Western&Graduate&PostdoctoralStudies

10-30-2020 10:00 AM

Mid-Infrared Studies of Galactic sources: Probing the Relationship Between Polycyclic Aromatic Hydrocarbons and their Physical Environment

Collin Matthew Knight, *The University of Western Ontario*

Supervisor: Peeters, Els, *The University of Western Ontario*
A thesis submitted in partial fulfillment of the requirements for the Doctor of Philosophy degree in Astronomy
© Collin Matthew Knight 2020

Follow this and additional works at: https://ir.lib.uwo.ca/etd

Part of the Stars, Interstellar Medium and the Galaxy Commons

Abstract

Over the past 50 years, prominent mid-infrared (MIR) emission features from 3–20 μm have been observed ubiquitously in the interstellar medium (ISM) of Galactic and extragalactic sources. These emission features arise from the vibrational relaxation of polycyclic aromatic hydrocarbons (PAHs) after the absorption of a far-ultraviolet (FUV) photon. PAHs are astronomically significant in that they contain up to 15% of the cosmic carbon inventory and play an important role in the physical and chemical processes of the ISM such as, for example, the gas heating and the ionization balance. Variations in the relative strengths of the major PAH bands can be used to understand their underlying molecular properties and their interaction with the surrounding photodissociation region (PDR) environment.

We employ these variations to characterize the PAH populations in terms of properties such as degree of ionization and sizes and investigate their dependence on the physical conditions such as the FUV radiation field strength, the gas density and the gas temperature for nearby spatially resolved Galactic PDRs. We find both size and charge tend to rise with increasing radiation field strength or proximity to the illuminating source. Correlations between PAH emission features in spatially resolved sources are found to be highly dependent on the PDR morphology (i.e. edge-on versus face-on) and environmental conditions. These results are indicative of significant UV processing driving the photochemical evolution of astronomical PAH populations.

We utilize observations of far-infrared (FIR) cooling lines of atoms and the FIR dust continuum emission of a nearby reflection nebula in combination with PDR models to derive maps of the physical conditions. Comparing these derived physical conditions with PAH emission characteristics at a matching spatial resolution and apertures allows us to critically test previous established relationships between PAH emission and these physical conditions. From these results, we show that these relationships also hold at a higher spatial resolution than previously obtained.

Summary for Lay Audience

Peppered throughout the interstellar medium of our Galaxy and other galaxies, young, massive stars are born from the depths of gigantic molecular clouds. These stars give off a large amount of UV light, which carves out ionized cavities around them through the irradiation of the surrounding cloud. The interface between the ionized cavity (or HII region) and the molecular cloud is referred to as a photo-dissociation region (PDR).

Within these irradiated PDRs, the physics and chemistry of its gas and dust constituents are driven by the high quantity of incident UV radiation, hence the name. The chemical species native to PDRs range from simple atomic gases to large dust grains of sub-millimeter size. Somewhere in between, we find large quantities of a peculiar group of molecules referred to as polycyclic aromatic hydrocarbons (PAHs). These PAHs are akin to such earthbound species found in soot, auto exhaust, tobacco smoke, charcoal, etc. All of which are notably highly carcinogenic.

We are able to detect emission from different gas and dust species within PDRs using astronomical observations that cover a large range in the electromagnetic spectrum. In particular, at mid-Infrared wavelengths of light, there is a prominent group of broad emission bands that are now widely accepted to result from the vibrational relaxation of PAH species that have previously absorbed a UV photon.

In this thesis, we investigate the dominant PAH emission features within four relatively nearby PDRs including: three reflection nebulae and the famous Orion Nebula. Questions we try to answer include: i) What is the effect of the UV radiation field on PAH molecular properties such as size and ionization state? ii) How do the PAH emission features vary within different types of interstellar environments? iii) Can we use these PAH emission features to quantitatively measure the physical conditions within PDRs?

Authorship statement

The following authors contributed to Chapter 2: C. Knight, E. Peeters, D. J. Stock, W. D. Vacca, A. G. G. M. Tielens

AGGMT, EP, and Olivier Berné wrote the observing proposal to obtain FLITECAM observations to trace the 3.3 μm PAH emission for the purpose of investigating the PAH size distribution in multiple sources. DJS provided useful suggestions and guidance on the data reduction process. WDV provided feedback and guidance on the calibration of the photometric data, as did EP. EP reduced the IRS spectral cubes used in our analysis. CK analyzed the photometric and spectroscopic data and identified trends in PAH size and ionization. CK prepared the figures and manuscript text. EP contributed to the interpretation of the data and provided regular discussions and feedback on the manuscript. AGGMT, DJS, and WDV provided additional comments and suggestions regarding the submission of this manuscript. All authors contributed to formulate the response to the referee's concerns.

The following authors contributed to Chapter 3: C. Knight, E. Peeters, W. D. Vacca.

EP and CK reduced the IRS spectral cubes used in our analysis. WDV provided feedback and guidance on the calibration of the photometric data, as did EP. CK analyzed the spectroscopic and photometric data and identified trends in the data. CK prepared the figures and manuscript text. EP contributed to the interpretation of these trends and provided regular discussions and feedback on the manuscript.

The following authors contributed to Chapter 4: C. Knight, E. Peeters, M. G. Wolfire, D. J. Stock.

CK, EP, DJS, and MGW wrote the proposal to obtain FIFI-LS of the FIR cooling lines for the purpose of a large-scale survey of PDR conditions and PAH emission. EP and CK reduced the spectral cubes used in our analysis. CK measured the PAH emission with the IRS spectral cube, measured the FIR cooling lines, performed the SED fitting to obtain the FIR dust continuum and input these data into the PDR models of MGW. MGW provided feedback and guidance regarding the use and interpretation of the PDR models. CK prepared the figures and manuscript text and identified trends in spectral data. EP provided useful manuscript comments and regular discussion towards the interpretation.

For my family and closest friends.

Without your love and support over the years, I would have been lost long ago.

Acknowledgements

First, words alone cannot express how grateful I am for my family. My parents, Valerie and Carl, who have taught me how to be a better person and have given me so much. My sisters, Cheryl and Sarah, have been immensely supportive and were always willing to make time for me when times were difficult. To the newest member of my family, Tara, thank you for making my life more meaningful and I look forward to the future. To the rest of my family and my close friends from home, I love you all and I appreciate your words of encouragement more than you know.

Second, a huge thank you to my advisor, Els Peeters. Completing this long and difficult journey would not have possible without your positive outlook and wisdom. Despite my many flaws and derailments, you stuck by my side and have given me hope for the future.

Finally, to everyone I met at Western during my stay, I truly appreciate your insight and kindness. I wish you all great success on the rest of your journeys.

Contents

List of Figures

List of Tables

List of Frequently Used Acronyms

2MASS	The Two Micron All-Sky Survey
AGB	Asymptotic Giant Branch
AKARI	The AKARI Space Telescope
BSS	Blind signal separation
FIR	Far-Infrared
FLITECAM	The First Light Infrared TEst CAMera
FORCAST	The Faint Object infraRed CAmera for the SOFIA Telescope
FOV	Field of View
FWHM	Full Width at Half Maximum
FUV	Far-Ultraviolet
H I	neutral H
H II	H^+
IR	Infrared
IRAC	The Infrared Array Camera
IRS	The Infrared Spectrograph
ISM	Interstellar Medium
ISO	The Infrared Space Observatory
JWST	The James Webb Space Telescope
LS	Local Spine Continuum
G_0	The FUV Radiation Field Strength
GS	Global Spine Continuum
HD	The Henry Draper Catalogue
MIR	Mid-Infrared
NGC	New General Catalogue
NIR	Near-Infrared

OBC	Orion Bar Combined Aperture
OBI	Orion Bar Ionized Aperture
PAH	Polycyclic Aromatic Hydrocarbons
PAHdb	The NASA Ames PAH Spectroscopic Database
PAHTAT	PAH Toulouse Astronomical Templates
PANH	Polycyclic Aromatic Nitrogen Heterocycle
PN(e)	Planetary Nebula(e)
PDR	Photodissociation Regions
PDRT	The Photo Dissociation Region Toolbox
PL	Dust Continuum
PSF	Point Spread Function
RN(e)	Reflection Nebula(e)
SOFIA	The Stratospheric Observatory for Infrared Astronomy
SED	Spectral Energy Distribution
SNR	Signal–to–Noise Ratio
SWS	The Short Wavelength Spectrometer
UIR	Unidentified Infrared
UV	Ultraviolet
VSG	Very Small Grain
YSO	Young Stellar Object

Chapter 1

Introduction

1.1 The Life of Stars

When we think of space, we think of just that, empty space with a few stars far in between. However the definition of this word betrays the true nature of the Cosmos beyond our little planet. Despite the perception of space as empty, there is an enormous quantity of gas and dust located between the stars, referred to as the interstellar medium (ISM). In other words, the stars and their planetary systems within our Milky Way only take up 3×10^{-10} of the available space, with the rest corresponding to the ISM (Tielens, 2005). The ISM is composed primarily of hydrogen and helium gases while all of the heavier elements only account for a small fraction. The ISM has multiple distinct phases including cold dense molecular gas, cold and warm neutral H clouds, warm ionized gas, hot H II regions (nebulae of ionized gas when recent star formation has taken place), and the highly diffuse, hot intercloud medium. The gas densities of these phases range from $\sim 10^{-3}$ cm^{-3} in the hot intercloud medium to $>10^5$ cm^{-3} in some H II regions and molecular clouds and temperatures range from ~ 10 K in molecular clouds up to $\sim 10^6$ K in the hot intercloud medium (Tielens, 2005). It is from the material in the ISM that all stars and subsequently all organic life is born.

All stars begin their life in a giant molecular cloud, with temperature on the order of T $\sim$ 10-15 K and densities of n $\sim 10^3$ cm^{-3}. The structure of the molecular cloud is not homogeneous, instead it may contain clumpy regions that tend to exceed the typical average densities in molecular clouds, up to 10^6 cm^{-3} (e.g. Shu et al., 1987) . Under the influence of gravity, these clumps contract inwards to eventually form hot dense cores, with T $\sim$ 100 - 300 K and n $\sim 10^7$ - 10^9 cm^{-3}. Gravitational contraction continues until these conditions become hot and dense enough within these cores to allow hydrogen fusion to occur, a process that usually occurs on the order of a million to a hundred million years. The immense amount of radiation pressure produced from this ignition pushes back against the cloud's gravitational collapse until the two forces eventually balance out into a stable configuration. It is in this way that a star begins its life cycle (see Figure 1.1 for a schematic outlining the typical life cycle of stellar objects with respect to the ISM).

The advent of hydrogen fusion for all stars is referred to as the zero age main sequence. Stars spend a large portion of their life cycle on the main sequence (MS), where hydrogen fusion in their core is the main source of energy to combat the ever present gravitational pull.
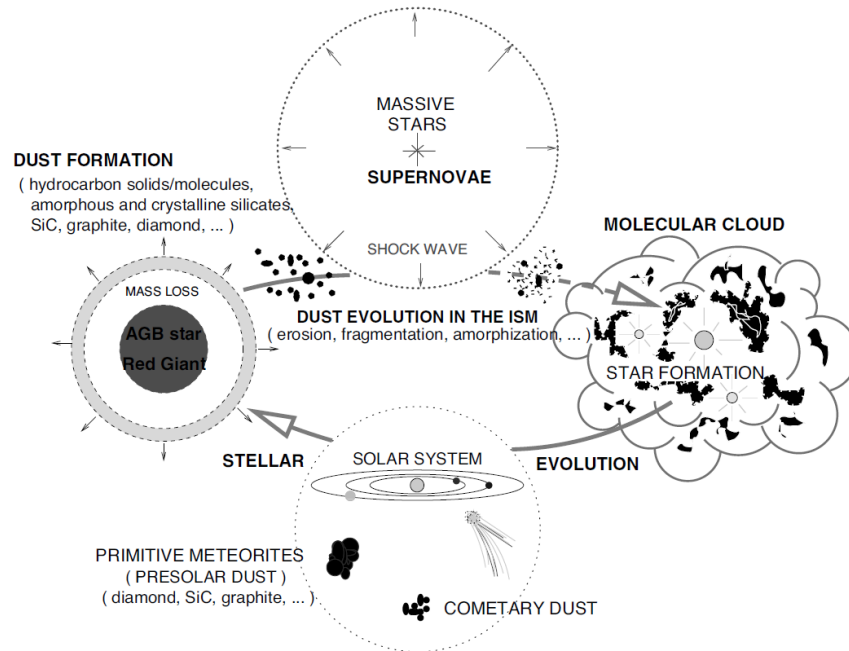
Figure 1.1: The life cycle of stars along with the associated gas and dust in the ISM. Within this cycle, interstellar gas and dust becomes more enriched with heavier elements moving in a clockwise direction. Figure from Jones (2004), reproduced by permission of the Astronomical Society of the Pacific Conference Series.

The main sequence lifetime of a star is determined by a multitude of factors, in particular its mass and core temperature. Early–type main sequence stars typically are much more massive (> 10 $M_\odot$) compared to their late–type counterparts, implying they are subject to a stronger gravitational field. This yields a higher core temperature, drastically increasing the rate of core hydrogen fusion as fusion is highly sensitive to temperature. These high–mass stars can exhaust their core hydrogen supply in tens to hundreds of millions of years. In contrast, intermediate–mass stars ($1.4 < M_\odot < 10$) take about a billion years to exhaust their core hydrogen supply, while in lower mass stars ($M_\odot < 1.4$), this same process is predicted take tens of billions up to even trillions of years.

After a star depletes its core hydrogen supply, gravitational contraction once again becomes the dominant force. The star continues to contract until it becomes hot enough for helium core fusion to begin. For intermediate to massive stars, the large gravitational force causes the temperature to become high enough to allow a smooth transition into helium fusion. In lower mass stars, degeneracy pressure (i.e. electrons are packed in so densely that they cannot be compressed by gravity any further due to all of the lowest energy states being occupied) and temperatures continue to rise until an abrupt chain reaction of helium fusion occurs throughout the core causing a rapid outburst of energy referred to as a helium flash. This marks the beginning of the horizontal branch where helium fusion persists in stellar cores.

For low–mass stars, helium core fusion tends to last about a tenth of the time of hydrogen core fusion (e.g. Carroll & Ostlie, 2007). The exhaustion of the helium core supply leads into

the asymptotic giant branch (AGB) phase. In AGB–type stars, the outer envelope becomes so tenuous that it cools enough to allow dust and gas molecules to form without being immediately destroyed. In the gas outflows of the star, chemical reactions involving dust grains and simple molecular gas can occur. Once the helium core is depleted, envelope contraction occurs until the hydrogen shell becomes hot enough to ignite. This hydrogen shell fusion in turn causes the outer envelope to expand until the temperature decrease stops further fusion. However, during hydrogen shell fusion, helium ash is deposited onto an inert helium shell layer surrounding the core, leading to the contraction of this helium shell until it becomes hot enough to begin helium fusion. This helium fusion is accompanied by a burst of energy expelling some of the outer envelope, referred to as a thermal pulse. The helium shell fusion will continue for a time until the expansion of the above hydrogen layers decreases the temperature within the helium shell, below the helium fusion threshold. This cycle of dual shell fusion accompanied by thermal pulses will continue around 10 times until all of the remaining envelope is blown off into a planetary nebula and only the inert carbon-oxygen core remains as a white dwarf remnant.

Similarly, intermediate–mass stars are also left with an inert carbon core after the helium fusion phase ends (e.g. Carroll & Ostlie, 2007). Helium shell fusion will continue to deposit ash onto the degenerate carbon core causing a continuous rise in temperature and pressure. This leads to a similar process as the helium flash found in low–mass stars as the conditions become hot enough to allow for a chain reaction of carbon fusion. However, this carbon flash produces much more energy in comparison and the entire envelope is rapidly expelled leaving only a dense, inert core. Further gravitational contraction compresses the electron and protons making up this core into neutrons, which are then able to repel further contraction via neutron degeneracy pressure (analogous to the aforementioned electron degeneracy pressure) to form a relatively stable neutron star remnant.

In the most massive stars once helium fusion ends, a cycle of gravitational contraction followed by core fusion of heavier elements will occur (e.g. Carroll & Ostlie, 2007). Above the core, hydrogen and helium fusion shells will form as the core contracts until the temperature becomes hot enough to begin carbon fusion. This leads to an onion-like structure with layers of more massive elements forming above the core as it continues to contract and fuse heavier elements all the way up to iron. As iron fusion is an endothermic reaction, it will not support the star against its massive weight. This results in a rapid contraction throughout the star onto the now rigid degenerate core. The degeneracy pressure within the core increases until it overcomes its gravity and the accumulated matter is rebounded sending a shock wave outwards with energies on the order of 10^{51} ergs. This results in a catastrophic event known as a Type II supernova where a massive star blows itself apart. It is prior to this event that elements heavier than iron are formed and distributed amongst the ISM.

In summary, all stars are essentially giant nuclear reactors that produce the elemental constituents of our Universe except for hydrogen and helium. When they have finally run out of nuclear energy to stop the timeless persistence of gravity, they release their material back into the ISM. Over time, the enriched gas will become part of the molecular clouds where the next generation of stars are born, thus beginning the stellar life cycle anew.

The gas and dust of the ISM also have a life cycle of their own as briefly discussed above. From the initial formation within the outflows of carbon–rich stars or from energetic processes with the ISM, incident UV radiation absorbed by this material promotes a rich gas-phase chemistry, yielding a wide variety of different molecular species. This material is further processed

and expelled throughout the local galaxy by means of stellar winds or supernovae shocks. Gravitational forces and local stellar environments cause the gas and dust to conglomerate into the different phases of the ISM. Some of this matter is contained in the dense cores of molecular clouds and becomes part of the star formation process. In the more diffuse ISM phases, this material can exist for up to hundreds of millions of years where photochemical processes from nearby stars continually change its molecular structure. We now turn our focus to a very conspicuous type of ISM material that illustrates the interplay between stars and their surrounding environment.

1.2   PAH Characteristics

Polycyclic aromatic hydrocarbon (PAH) molecules are found throughout the ISM in abundance in a wide variety of astronomical environments. These species are thought to be formed in the outflows of carbon-rich stars or from energetic processes such as interstellar shocks within the diffuse ISM (e.g. Tielens, 2008, and references therein). PAHs are organic molecules characterized by multiple planar benzene (or hexagonal) rings linked together in a planar honeycomb structure with peripheral hydrogen atoms inhabiting the edge of the molecule. Figure 1.2 shows a single benzene ring along with some simple PAH species. Each carbon atom in a ring forms three covalent σ-bonds with adjacent carbon or hydrogen atoms. The fourth valence electron from each carbon atom forms a delocalized π-bond that is shared throughout the ring, hence we refer to these bonds as having an aromatic nature. Aromatic bonds are significantly more stable than non-aromatic bonds, making PAHs more resilient to interstellar conditions compared to linear (aliphatic) hydrocarbons.

On Earth, PAHs are a component of incomplete combustion products that we encounter on a daily basis. Some terrestrial examples of PAHs are auto exhaust, soot, tobacco smoke, and coal. All of these chemical species are carcinogenic and prolonged exposure should be avoided. Despite these health concerns, there is immense scientific value in studying the PAH species that can be found here as a prototype of those that exist throughout the Universe.

It should be noted that various carbonaceous molecules are present in space. In particular, fullerenes are spherical or ellipsoidal cage structured molecules made of both 5-membered and 6-membered aromatic carbon rings (Figure 1.2). These molecules were hypothesized to form around stars with carbon-rich, hydrogen poor atmospheres (e.g. Kroto & Jura, 1992) or within the ejecta of Type II supernovae (Clayton et al., 2001). Recent observational evidence has shown the presence of multiple fullerene species: C_{60}, C_{60}^+, and C_{70} in numerous environments including a planetary nebula (PNe, Cami et al., 2010), in reflection nebulae (RNe, Sellgren et al., 2010), and the diffuse ISM (Berné et al., 2017; Cordiner et al., 2019).

1.2.1   Mid–Infrared Astronomical Spectra

Mid-infrared (MIR) spectroscopic observations for a large range of astronomical sources show prominent emission features at 3.3, 6.2, 7.7, 8.6, 11.2, and 12.7 μm, attributed to the IR fluorescence of PAHs (Allamandola et al., 1985). These bands were originally observed by Gillett et al. (1973) and were first referred to as the unidentified infrared bands (UIR). This was due to the nature of their carriers being unknown for a decade after their discovery.

Benzene (C_6H_6)   Naphthalene ($C_{10}H_8$)   Pyrene ($C_{16}H_{10}$)

Coronene ($C_{24}H_{12}$)   Ovalene ($C_{32}H_{14}$)   Fullerene (C_{60})
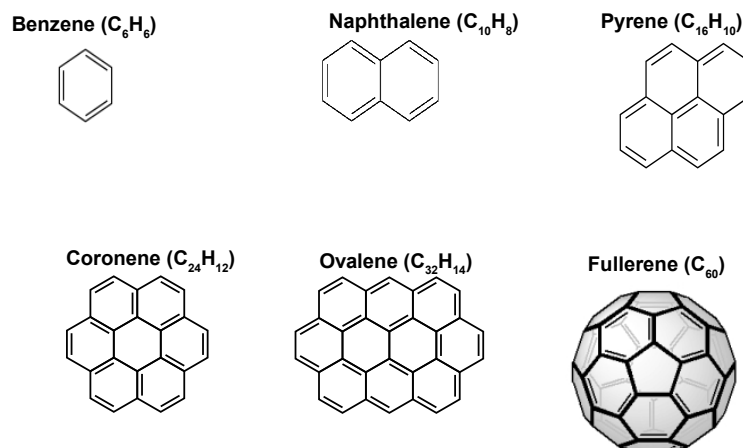
Figure 1.2: Chemical structure of benzene and a few small PAH species made up of multiple benzene rings fused together: napthalene, pyrene, coronene, and ovalene. Peripheral hydrogen atoms are not shown here. PAHs in the ISM typically are significantly larger with ∼ 50–100 carbon atoms and sizes of ∼ 6–9 Å (e.g. Tielens, 2005). Also shown is C_{60}, a fullerene cage made up of aromatic carbon rings.[2]

Since their discovery, these PAH emission features have been observed using ground-based, airborne, and space-based observatories. They are ubiquitous and dominate the MIR spectra of virtually all objects that have gas and dust illuminated by stellar ultraviolet (UV) radiation. This includes Galactic and extragalactic sources such as H II regions, post-AGB stars, young stellar objects (YSOs), PNe, RNe, the (diffuse) ISM, galactic nuclei, and galaxies as a whole (e.g. Hony et al., 2001; Verstraete et al., 2001; Peeters et al., 2002; Smith et al., 2007b; Galliano et al., 2008, 2018).

A typical MIR spectrum is shown in Figure 1.3 of the Orion Bar. Strong PAH emission at 3.3, 6.2, 7.7, 8.6, 11.2, and 12.7 μm can be seen, along with additional weaker features of the same nature at 3.4, 5.25, 5.7, 6.0, 11.0, 12.0, 13.5, 14.2, 15.8, 16.4, 17.4, and 17.8 μm. All of these features are on top of broad emission plateaus at 3.2-3.6, 6-9, 11-14, and 15-19 μm which are perched on top of a rising dust continuum.

---

[2]"Structure of benzene" and "Structure of naphthalene" by NEUROtiker; "Structure of pyrene." by Emeldir; "The structure of Coronene" and "The structure of Ovalene, a polycyclic aromatic hydrocarbon, or PAH" by Inductiveload; "Image of [60]Fullerene or C-60" by Torsten Brandmueller released into the public domain (https://commons.wikimedia.org/wiki/File:Benzol.svg, https://commons.wikimedia.org/wiki/File:Naphthalin.svg, https://commons.wikimedia.org/wiki/File:Pyrene_200.svg, https://en.wikipedia.org/wiki/File:Coronene.svg, https://commons.wikimedia.org/wiki/File:Ovalene.svg, https://commons.wikimedia.org/wiki/File:C60-1.jpg).
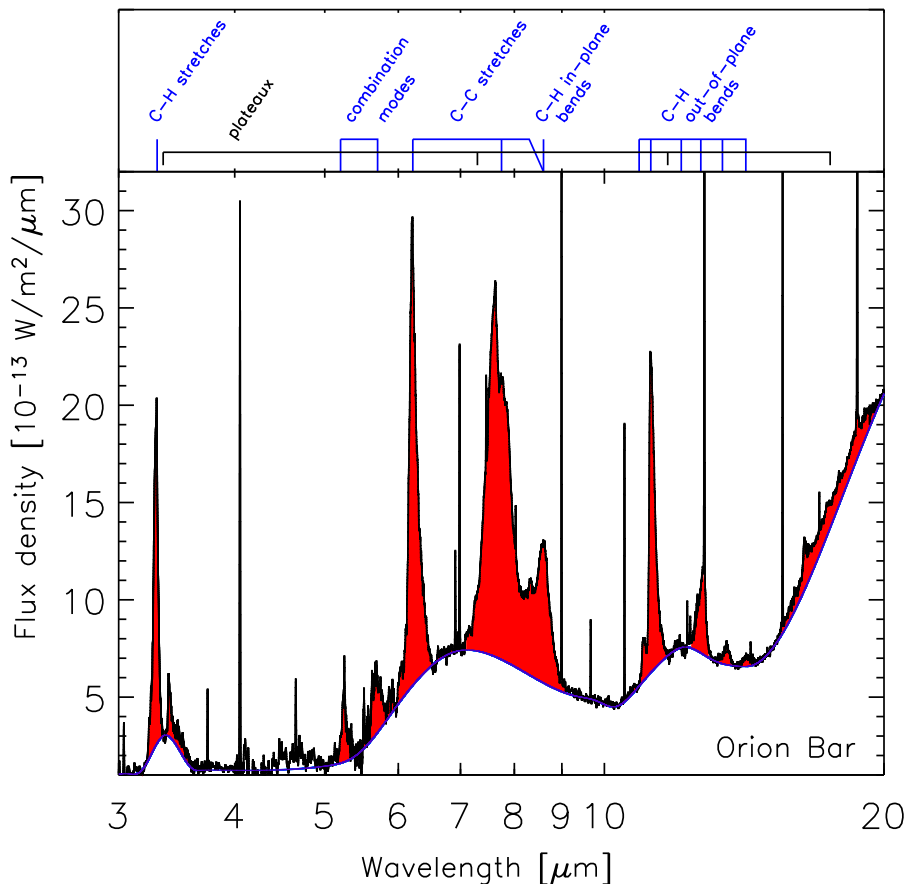
Figure 1.3: The MIR spectra of the Orion Bar (shown in black). The emission features attributed to PAHs are shown in red with the associated vibrational modes labelled in the top panel. The purple line separates the PAH emission from the emission plateaus due to larger carbonaceous grains and the rising dust continuum. Figure from Peeters et al. (2004a), reproduced by permission of the Astronomical Society of the Pacific Conference Series.

1.2.2   PAHs as Carriers of UIR Emission Bands

The first glimpse into the identification of the carriers of the UIR bands was the attribution of the 3.3 μm band to the vibrational excitation of aromatic C-H groups by Duley & Williams (1981). In the following years, various carbonaceous species were considered as potential carriers including hydrogenated amorphous carbon (Duley & Williams, 1988), quenched carbon composite (Sakata et al., 1984), coal (Papoular et al., 1989), and PAHs (e.g. Allamandola et al., 1989; Puget & Léger, 1989). The vibrational spectra of all of these species have emission bands which peak at the same wavelengths as the UIR bands. Hence, any of these spectra can provide a reasonable fit to the observed astronomical spectra. These similarities largely stem from all of these species consisting of primarily aromatic material on the smallest scales. For example, a comparison of the 6.2 and 7.7 μm emission bands in the MIR spectrum of the Orion Bar with the MIR Raman spectra of auto exhaust shows remarkable similarities (see Figure 1.4). The

agreement between these two spectra gives strong evidence for the carriers of the UIR bands being comprised of aromatic material.
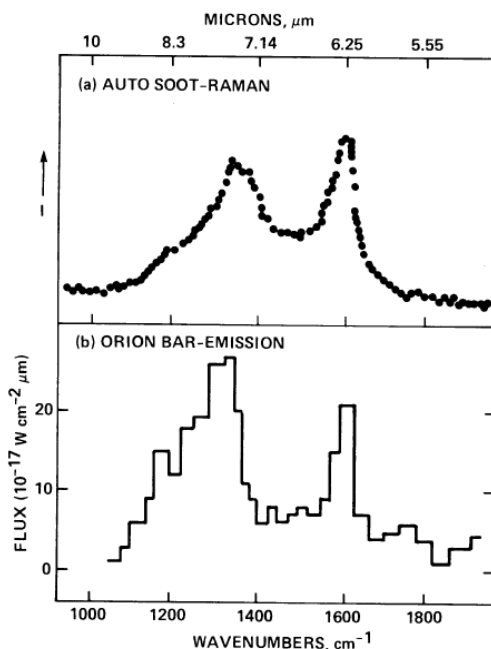
Figure 1.4: (a) Raman spectra from 5 to 10 μm of auto exhaust. (b) Orion Bar spectrum from 5 to 10 μm. Figure from Allamandola et al. (1985), reproduced by permission of the AAS.

The distinction between the carriers of the UIR bands existing as aromatic molecules in the gas phase as opposed to larger dust grains was first made by Sellgren (1984). She observed near-infrared emission in three RNe, which all showed strong 3.3 μm emission with a smooth continuum from 1.25 to 4.8 μm, characterized by a colour temperature of $\sim$ 1000 K. This emission was found to be independent of the distance from the illuminating source. Large classical carbonaceous dust grains containing $\sim$ 1000 carbon atoms are in thermal equilibrium with their environment. In the diffuse ISM with temperatures on the order of 10 K, these dust grains do not become hot enough to account for the observed emission. Sellgren (1984) explained these observations in terms of an emission model where very small grains with a typical size of 10 Å are rapidly heated to 1000 K through the absorption of a single UV photon, referred to as stochastic heating. Further studies confirm that the carriers of the UIR bands must be small aromatic molecules (PAHs) containing $\sim$ 50 carbon atoms (e.g. Léger & Puget, 1984; Allamandola et al., 1989; Tielens et al., 1999).

1.2.3   PAH Emission Mechanism

The emission process responsible for the PAH emission features is detailed as follows (e.g. Allamandola et al., 1989; Puget & Léger, 1989; Tielens, 2005): a PAH molecule absorbs a far-ultraviolet (FUV) photon causing it to transition into a higher electronic energy level with

internal temperatures greater than 1000 K. This energy is rapidly ($\sim 10^{-9}$ s) internally redistributed into high vibrational excitation in a lower electronic state. The vibrationally excited PAH molecule will then cool down predominantly through IR fluorescence relatively slowly (~ 1 s) which is observed as MIR emission. An excited PAH molecule cools back down to the equilibrium temperature of its environment (~ 10 K) after a few seconds and will remain cold until it absorbs another FUV photon. Characteristic time scales between FUV absorption events range from ~ 10 minutes in photo-dissociation regions (PDRs) such as the Orion Bar to once a year in the diffuse ISM (Tielens, 2005).

The relaxation of vibrationally excited PAH species occurs most prominently through C-C and C-H vibrational modes. Each of the major PAH bands are attributed to aromatic bending and stretching modes between the atomic constituents within PAH molecules (Allamandola et al., 1989). The 3.3 μm band is attributed to aromatic C-H stretching, the 6.2 μm and 7.7 μm bands are both attributed to C-C stretching, while the 8.6 μm band is attributed to C-H in-plane bending. Emission in the 10-15 μm range is attributed to C-H out-of-plane bending modes, including bands at 11.0, 11.2, 12.7, 13.5, and 14.2 μm (Allamandola et al., 1989; Hony et al., 2001). The frequency of each of these emission bands depends on the number of adjacent peripheral C-H bonds; which may be solo, duo, trio, or quartet C-H groups. Weaker PAH bands in the 15-20 μm range are attributed to C-C-C bending modes (Allamandola et al., 1989).

1.2.4   Astronomical Importance

There are numerous reasons why PAH species are significant within an astronomical context aside from their ubiquity. PAHs contain up to 15% of the cosmic carbon inventory (Allamandola et al., 1989), a non negligible fraction of the key element in organic chemistry and biological life as we know it. The MIR emission attributable to PAHs accounts for up to 20% of the total IR emission in galaxies (Smith et al., 2007b). In other words, PAHs absorb a significant amount of UV energy from young, high–mass stars. Consequentially, PAH emission serves as a tracer of star formation rates (e.g. Peeters et al., 2004a).

PAHs play an important role in several significant astrophysical and astrochemical processes. The heating of neutral gas in the ISM is driven in large part through the photoelectric ejection of electrons from PAHs and PAH clusters (Bakes & Tielens, 1994). The ionization balance in the neutral ISM is dominated by the photoionization and recombination of PAHs (Lepp & Dalgarno, 1988). Their large surface area also makes them ideal sites for surface chemistry, providing an environment to facilitate the formation of smaller molecules such as H_2 (e.g. Habart et al., 2004; Wolfire et al., 2008; Verstraete, 2011). Additionally, the chemical structure of PAHs may be modified through photo-processing. In this way other carbon–based species may be formed, such as smaller hydrocarbon radicals and carbon chains (Tielens, 2008) or even fullerenes (e.g. Berné & Tielens, 2012; Zhen et al., 2014). Finally, PAH species in water ice may be relevant in the formation of prebiotic molecules, such as amino acids (Allamandola, 2011). Hence, MIR observations of PAH-rich environments are a way to reveal the molecular nature of the Universe.

1.3 Variability in PAH Emission

To first order, the MIR spectra of many astronomical sources show the same PAH emission features. Upon closer inspection, there are subtle differences as these PAH emission features tend to show variability in intensities, peak positions, and profiles between sources and spatially within extended sources (e.g. Bregman et al., 1989; Hony et al., 2001; Peeters et al., 2002; Galliano et al., 2008; Stock et al., 2016; Peeters et al., 2017). In this section, we address the variations found in these spectra and relate them to the underlying physical principles at work.

1.3.1 Intensity Variations

Variations in the strength of the major PAH emission bands (e.g. 3.3, 6.2, 7.7, 8.6, 11.2, and 12.7 μm) can be seen between and within astronomical sources (e.g. Joblin et al., 1996a; Hony et al., 2001; Vermeij et al., 2002; Smith et al., 2007b; Galliano et al., 2008). To a lesser extent, the weaker bands also demonstrate variation in emission strength (e.g. Peeters et al., 2012; Shannon et al., 2015). These variations are found not only in absolute PAH emission strength but also in their relative emission strength (emission ratios, e.g. 8.6/11.2 μm). Relative intensities are advantageous in that they normalize differences between objects of study including abundances and distances to the observer (e.g. Chan et al., 2000).

PAH bands are typically characterised observationally by how well they correlate with each other. For instance, the 6.2, 7.7, and 8.6 μm emission ratios are highly correlated over a wide range of environmental conditions (e.g. Joblin et al., 1996a; Vermeij et al., 2002; Smith et al., 2007b; Galliano et al., 2008) indicating these features originate from the same PAH subpopulation (Figure 1.5). The 6.2 μm band has also been found to correlate with the 12.7 μm band (e.g. Hony et al., 2001). Likewise, the 3.3 and 11.2 μm emission bands are well correlated with each other but not with the 6-9 μm emission bands, suggesting that these bands become more prominent in different subpopulations of PAHs (Figure 1.5, Russell et al., 1977; Hony et al., 2001). It is also worthwhile to note that the weaker 11.0 μm band has been shown to be strongly correlated with the 8.6 μm band and, to a slightly lesser extent with the 6.2 and 7.7 μm bands (e.g. Peeters et al., 2017).

Correlations between the weaker PAH emission bands in the 15-20 μm range and the major PAH bands are also present in wide range of astronomical environments (e.g. Boersma et al., 2010; Peeters et al., 2012; Shannon et al., 2015). The 15.8 μm band shows correlations with the 11.2 μm band. In contrast, the 16.4 μm band shows correlations with the 6.2 and 12.7 μm bands. The 17.4 μm band shows weak correlation with the 16.4 μm band, but is more prominent in higher radiation fields towards the illuminating sources observed. The 17.8 μm band is found to have two components that are similar to the 11.2 and the 12.7 μm bands respectively.

1.3.2 Profile Variations

The profile and peak position of the PAH emission features in the 6-9 μm range show significant variations (Figure 1.6, Peeters et al., 2002). Peeters et al. (2002) classified the profile variations based on the peak positions of the PAH emission features and their overall shape into three spectral classes: A, B, and C. Profile variations are most apparent in the 7.7 μm complex in terms of its two main components at 7.6 and 7.8 μm with varying relative emission strength
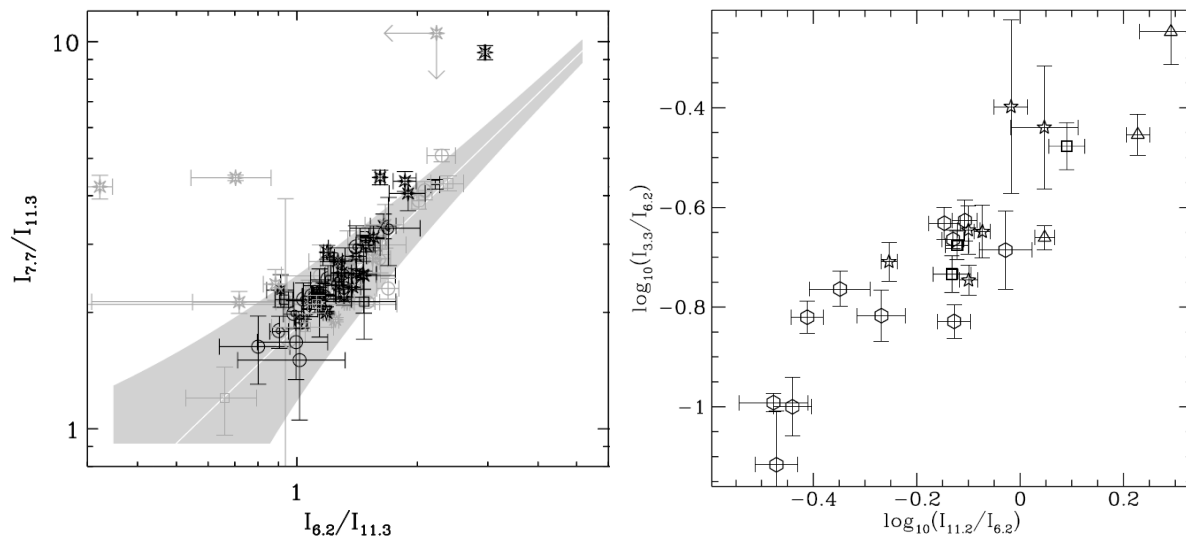
Figure 1.5: *left* The relative integrated strength of the 6.2 μm vs. the 7.7 μm PAH emission bands, both normalized to the 11.2 μm band, over a large sample of Galactic and extragalactic sources. The black points and associated error bars correspond to measurements that are considered to be reliable, whereas the gray points have a higher uncertainty. Figure from Galliano et al. (2008), reproduced by permission of the AAS. *right* The relative integrated strength of the 3.3 μm vs. the 11.2 μm PAH emission bands, both normalized to the 6.2 μm band, from a survey of Galactic sources. Hexagons are H $\textsc{ii}$ regions and intermediate–mass star–forming regions, squares are RNe, and triangles are PNe. Figure from Hony et al. (2001), reproduced with permission © ESO.

(Bregman, 1989; Cohen et al., 1989). Class A spectra have emission features that peak at shorter wavelengths relative to the other classes: the 7.7 μm emission band peaks at $\sim$ 7.6 μm. Class B peaks redward of class A: the 7.7 μm band peaks between 7.8 and 8.0 μm. Class C has a broad emission feature that peaks at 8.22 μm instead of the typical profile shape seen for the 7.7 μm complex as shown in Figure 1.3. More recently, a fourth spectral class, D, has been discovered that has broad emission from 7 - 9 μm (Matsuura et al., 2014). The shift in peak position is also apparent in the 6.2 and 8.6 μm to a lesser degree: the difference between class A to C peak positions range from 6.2 to 6.3 μm in the 6.2 μm band, whereas the difference between the class A and B peak positions range from $\sim$ 8.6 to 8.7 μm in the 8.6 μm band. Note that in class C profiles, the 8.6 μm band is very weak or absent.

The 3.3 and 11.2 μm emission features are also distinguished in terms of class A and B spectra (Figure 1.6, van Diedenhoven et al., 2004). Observations of the 3.3 μm band show two distinct profile types: a symmetric feature peaking at $\sim$ 3.290 μm and an asymmetric feature peaking at $\sim$ 3.3 μm. The 11.2 μm profile is generally asymmetrical with peak position ranging from 11.20 - 11.24 μm.

Each of these spectral classes are dependent on the type of object, while the reverse is not true. That is to say, there is not a one-to-one correlation between some sources, such as post-AGB stars and PNe, and their associated spectral class. Generally, Class A profiles are found
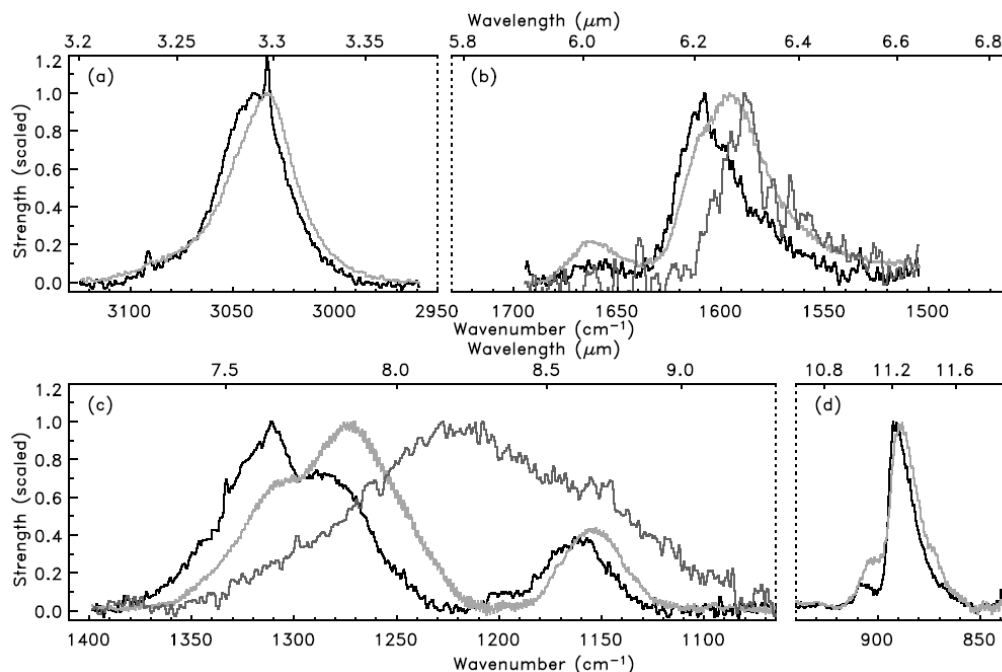
Figure 1.6: Profile variations of the major PAH emission features. In each case, class A peaks at the shortest wavelength (shown as a black line) and class B peaks at a longer wavelength (shown as a light grey line). For the 6–9 μm features, there is a third class C (shown as grey line), peaking at even longer wavelengths than the class B profiles. Note that the spectra shown in each panel are normalized to the peak intensity of the emission features within the wavelength range given. Figure from van Diedenhoven et al. (2004), reproduced by permission of the AAS.

in interstellar sources including H II regions, RNe, and non–isolated Herbig Be stars but also include some PNe and post-AGB stars. Class B profiles are found in circumstellar sources including planetary nebula, isolated Herbig Be stars and some post-AGB stars. Class C and D profiles have only been found in a couple post-AGB and Herbig Ae/Be stars. This classification suggests that the emission properties of PAHs and their composition are determined by the local environment.

Finally, from a study on the profile variations of a sample of post-AGB stars and isolated HAeBe stars of class B or C, Sloan et al. (2007) found an anti-correlation between the peak position of the 7.7 μm band with the effective temperature of the exciting star. This correlation does not extend to class A objects. Despite this, they attributed this trend to an increase in UV processing as the driving factor for profile variations. Hotter stars will produce a stronger UV radiation field, thus increasing the degree of photo-processing in a nearby PAH population.

1.3.3   Emission Variations as Tracers of Physical Properties

The variations found between the 6–9 μm bands and the 3.3, 11.2 μm bands can be explained through consideration of the underlying physical properties. Comparison of astronomical spec-

tra with experimental and theoretical PAH spectra suggest the most significant driver of intensity variations is PAH charge (e.g. Joblin et al., 1996a; Hony et al., 2001; Hudgins & Allamandola, 2004; Galliano et al., 2008; Bauschlicher et al., 2008). The emission strength of the 6.2, 7.7, and 8.6 μm emission feature are found to increase with ionization, whereas the emission strength of the 3.3 and 11.2 μm emission features are prominent in neutral PAHs (Allamandola et al., 1989; Bauschlicher et al., 2008). The 12.7 μm emission feature has been found to have spectral components corresponding to both cationic and neutral PAHs (Boersma et al., 2013; Shannon et al., 2016). The 11.0 μm band, is attributed to solo C-H out-of-plane bending modes in PAH cations, acting as an ionized analog to the neutral 11.2 μm band (e.g. Hudgins & Allamandola, 1999). Additionally, based on the observed correlations, the PAH emission features in the 15–20 μm range have also been linked to both cationic PAHs (16.4, 17.4 μm and a component of the 17.8 μm band) and neutral PAHs (15.8 μm and a component of the 17.8 μm band, e.g. Boersma et al., 2010; Peeters et al., 2012; Shannon et al., 2015).

The intensity ratio of ionized to neutral PAHs as traced by, e.g. the 6.2/11.2 emission ratio, can be used to trace the ionization balance of the emitting PAH population (e.g. Galliano et al., 2008; Stock et al., 2016). The charge state of the PAH population is determined by the ratio of the ionization and recombination rates which sets the PAH ionization parameter, $\gamma = G_0 T^{0.5}/n_e$, where G_0 is the intensity of the ambient FUV radiation field, T is the gas temperature, and n_e is the electron density (Bakes & Tielens, 1994). Hence, the ionized to neutral PAH emission ratio can be used to probe environmental conditions.

PAH emission ratios can provide more insight on the properties of a PAH population than just the relative charge state. The 11.2/3.3 emission ratio can be used as a tracer of the average size of the emitting population (Schutte et al., 1993; Ricca et al., 2012; Maragkoudakis et al., 2020). Both of these emission bands correspond to primarily neutral species and cover the largest wavelength range between the major PAH bands. These traits avoid any dependency on ionization and maximize the spectral sensitivity to temperature respectively. As previously discussed, the absorption of a FUV photon by a PAH molecule results in stochastic heating with a rapid rise in internal energy that is redistributed to vibrational energy (Allamandola et al., 1989). Smaller PAHs have fewer vibrational modes, and so become hotter than larger PAHs when a photon with the same amount of energy is absorbed and will emit more radiation at a shorter wavelength. Through probing variations in relative PAH size through the 11.2/3.3 emission ratio within an extended region, we can find evidence of the photochemical evolution of these species promoted by UV processing (e.g Croiset et al., 2016, Knight et al. submitted (Chapter 2)).

Another useful way to probe a PAH population is through the 11.2/12.7 emission ratio as it can be used to determine the prevalent molecular edge structure of these species (Hony et al., 2001; Bauschlicher et al., 2009). Recall that both emission features are attributed to C-H out-of-plane bending modes: the 11.2 μm band is due to solo C-H adjacency and the 12.7 μm band is ascribed to a combination of duo and trio C-H groups. If the intrinsic strength of each band is known, observations reveal the relative abundance of solos and duo C-H groups. In regions where the 11.2 μm band dominates, there is an abundance of large, compact, symmetrical PAHs. In contrast, a stronger 12.7 μm band implies the presence of more irregularly shaped PAHs. However, as the 11.2 μm is largely dominated by neutral PAHs and the 12.7 μm by both ions and neutrals, correction for the influence of PAH charge must be made (e.g. Boersma et al., 2013; Shannon et al., 2015).

1.4   Life Cycle of PAHs

1.4.1   Formation

The formation of PAHs is still a topic of debate despite their ubiquitous nature in the ISM. There are currently two proposed formation routes: bottom-up processing, where PAHs are formed from smaller hydrocarbon molecules in the outflows of carbon-rich AGB stars and top-down processing, where PAHs are formed through the fragmentation of larger carbonaceous grains.

Bottom-up Processing

PAHs are a natural product in the outflows of carbon-rich AGB stars, as they provide a high temperature soot-producing environment (Latter, 1991). Due to the absence of UV photons in these stars, there is a lack of observational evidence for PAH formation in these outflows in most cases. However, in the later evolutionary stages of these stars with higher effective temperatures, including carbon-rich post-AGB objects and PNe, the PAH emission features can be seen. Additionally, PAH emission has been detected in carbon-rich AGB stars where a blue binary companion provides UV–pumping photons (Boersma et al., 2006).

PAH formation in the carbon-rich AGB outflows is thought to begin with the smaller carbonaceous species present. Most of the carbon in AGB outflows is in the form of CO and C_2H_2 (acetylene). CO is a highly stable species and is relatively impervious to the high temperature environment. C_2H_2 is significantly more reactive than CO with atomic hydrogen promoting the formation of larger hydrocarbon species. This is similar to the combustion processes found on Earth, where PAHs are a significant intermediate species in soot formation (Frenklach et al., 1985).

Theoretical studies of PAH formation in AGB outflows have been done by Frenklach & Feigelson (1989) and Cherchneff et al. (1992). The formation of a single benzene ring from C_2H_2 or C_3H_3 is the rate–limiting step to PAH formation (Miller & Melius, 1992). There are multiple proposed mechanisms for the growth of additional aromatic rings, one of note is the hydrogen abstraction-acetylene addition (HACA) mechanism as described by Frenklach et al. (1985). In this case, radical sites on the benzene ring allow additional C_2H_2 species to bond, which can lead to the formation of another ring and so on. However, a recent computational study has suggested that this mechanism fails for PAH species with more than three benzene rings and thus alternative formation pathways are required (Kaiser et al., 2015).

Top-down Processing

Larger carbonaceous dust grains composed of aromatic and aliphatic material are present throughout the ISM. One of the natural products of the fragmentation of these species are freely-floating PAH molecules. PAHs can be extracted from carbonaceous dust through interstellar shocks and UV radiation.

Shock waves produced by supernovae or the stellar outflows of young stars ripple throughout the ISM, causing high velocity grain-grain collisions (Tielens, 2008). Collisions between large and small grains can cause fragmentation or complete destruction of entire grains. Jones

et al. (1996) have calculated the lifetime of large grains (of size ~ 1000 Å) against shattering from collisions to be ~ 10^8 years. A typical interstellar shock can free 10% of the carbonaceous material in grains to produce smaller carbon species of size < 15 Å, characteristic of PAHs and very small grains (Jones et al., 1996). Unfortunately, there is currently minimal evidence for PAH formation in regions affected by interstellar shocks due to the difficulty of separating the emission of supernova remnants from the Galactic background (Tielens, 2008). With regards to shocks produced by young stars, PAH emission has been observed in the shocked gas of the superwind produced by the nuclear starburst in M82 (Engelbracht et al., 2006).

Another hypothesis is the fragmentation by UV radiation of very small dust grains (VSG) into PAHs. Cesarsky et al. (2000) attribute continuum and broadband emission in the RN Ced 201 found far from the illuminating star to VSG of size ~ 1 nm. VSG are thought to be present throughout the ISM, but only show MIR emission in specific environments where they are sufficiently heated such as RNe. Within these extended environments, continuum emission far from the illuminating source comes from the same chemical family as the PAH emission features closer to the source, but these two types of emission are not directly correlated (e.g. Cohen et al., 1985; Roche et al., 1989; Bregman et al., 1989). The stratification with respect to distance from the illuminating source in the observed MIR emission due to VSG and PAHs with increasing UV flux is indirect evidence of VSG fragmentation producing PAHs (e.g. Rapacioli et al., 2005). Additionally, Goto et al. (2003) found that the relative intensity of the 3.4 μm band (aliphatic C-H stretching) to the 3.3 μm band (aromatic C-H stretching) decreased with increasing distance from a carbon-rich post-AGB star, indicative of the UV processing of dust grains into material with a higher degree of aromaticity.

1.4.2   PAH Evolution

The chemical evolution of PAHs – i.e. their transformation into other carbonaceous species as well as other PAH species – is determined by the environmental conditions. We consider some of the principal drivers of PAH evolution such as grain-grain collisions, freezing onto grain surfaces, and photo-processing which modifies the PAHs in the following ways. First, in low energy grain-grain collisions, PAHs grow through the coagulation or accretion of other species and can become a part of larger dust grains. In contrast, in high energy collisions, PAHs are fragmented or completely destroyed. Second, in the low temperature environments of dense molecular clouds, PAHs will freeze out onto grain surfaces. Incident UV radiation or cosmic rays on these ice mantles induce chemical reactions involving PAHs that lead to a multitude of complex molecules, including some prebiotic materials, such as amino acids and amphiphilic organic compounds similar to cell membranes (Allamandola, 2011). Finally, the photo-processing of PAHs further changes the PAH structure. Significant progress has recently been made on understanding the effects of photo-processing, and we will expand on this in the following section.

The Effects of UV Processing on PAH Evolution

With the advent of the current generation of high spatial resolution observatories, in particular the Spitzer Space Telescope, we can investigate variations in MIR emission on a much finer spatial scale. This allows the properties of PAHs and their relationship to the UV radiation

field from the illuminating stellar source to be investigated on much smaller scales in sources with strong MIR emission (e.g. Peeters et al., 2012; Boersma et al., 2013; Shannon et al., 2015; Stock et al., 2016; Peeters et al., 2017; Stock & Peeters, 2017; Andrews et al., 2018).

PAHs and Other Carbonaceous Species

PAHs and C_{60}   The fraction of elemental carbon locked–up in PAH species can be measured using IR observations with the following equation (Tielens 2005):

$$f_c = 0.23 \, \frac{(7 \times 10^{-18} cm^2)}{\sigma_{uv}^{PAH}} \, \frac{R}{(1 - R)}, \tag{1.1}$$

where σ_{uv}^{PAH} is the UV absorption cross-section of PAHs, with a typical value of 7 x 10^{-18} cm^2 per carbon atom and R is defined as the ratio of PAH flux to the total IR flux, which is represented by the sum of the total MIR PAH flux and the far-infrared (FIR) flux. Using the typical values of the elemental carbon abundance (3.9×10^{-4}) and the average number of carbon atoms in an interstellar PAH molecule (50 carbon atoms, Tielens et al., 1999), the PAH abundance can be determined. A variation in the PAH abundance reflects the formation and/or destruction of PAHs, exemplified by Berné & Tielens (2012) in their analysis of the RN NGC 7023. These authors reported a decrease in PAH abundance from the PDR front towards the central star. This suggests that the higher UV radiation field near the star increases the rate of photo-destruction of PAHs.

In addition, this decrease in PAH abundance towards the central star coincides with an increase in the C_{60} abundance (see Figure 1.7). This anti-correlation indicates that the formation of fullerenes may be related to the fragmentation of large PAH species (> 60 carbon atoms). Based on this observation, Berné & Tielens (2012) hypothesized a top-down model in which the UV processing of large PAHs can lead to the formation of C_{60}. The strong UV radiation field near the star first dehydrogenates the PAHs leaving large graphene sheets. Upon further photo-processing, the graphene species will isomerize into C_{60} as it is significantly more stable. Theoretical models have shown C_{60} can survive for a long period of time in the harsh radiation near a star whereas similar sized PAHs are quickly destroyed (Berné et al., 2015).

In order to test the hypothesis of C_{60} formation from PAHs in a laboratory environment, Zhen et al. (2014) irradiated large PAHs with UV lasers. These authors found that upon the irradiation of large PAHs, sequential H losses occurred until these PAHs were fully dehydrogenated into graphene. Further irradiation lead to the removal of C_2 molecules in the graphene sheet which induced curling into the cage structures of fullerenes. Thus, fullerenes can be formed through the photo-processing of PAHs.

PAHs and VSG   Blind signal separation (BSS) is a mathematical technique that restores a set of unknown spectral source signals due to their different morphology from an observed mixture of spectra that is a linear combination of the source spectra without any information on the mixing parameters (Aapo Hyvärinen, 2001). BSS analysis has been used to explain spatial variations in MIR spectral maps of RNe in terms of three different spectral components, layered with distance to the star (see Figure 1.8, e.g. Boissel et al., 2001; Rapacioli et al., 2005; Berné et al., 2007). The component closest to the illuminating star is attributed to PAH ions of
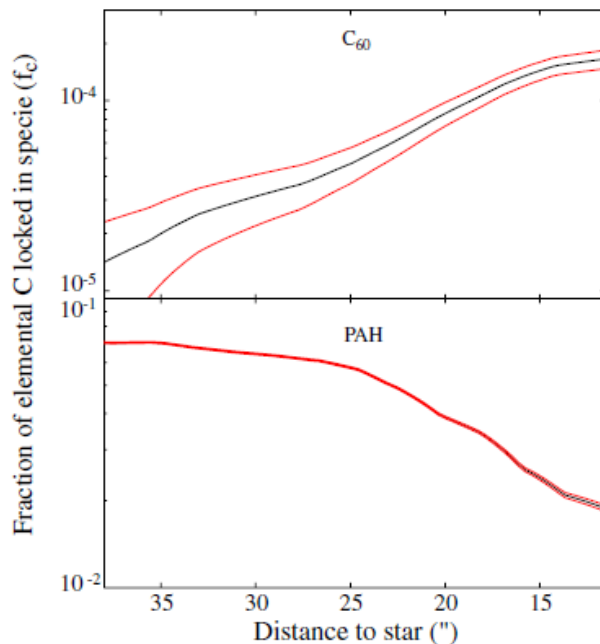
Figure 1.7: Abundances of PAHs and C_{60} as a function of distance from the central star in NGC 7023. The red curves give the 1-sigma uncertainty. Figure from Berné & Tielens (2012), reproduced by permission of the PNAS.

typical size of 50–150 carbon atoms. Moving further away, the next component is attributed to neutral PAHs of similar size as the aforementioned PAH ions. The spectral component deepest into the cold molecular clouds is hypothesized to be due to VSG or very large PAH species of size > 300 carbon atoms. The change in dominant species is ascribed to an increase in the level of UV processing with decreasing distance from the illuminating source. At the edge of the molecular cloud, VSGs are photo-evaporated prompting the release of smaller neutral PAH species. These molecules are subsequently ionized as they drift closer to the star and are eventually destroyed or transformed into other, more stable carbonaceous species upon sufficient photo-processing.

Spatial Variations of PAH Populations

Charge   PAH charge is an important factor in determining the relative intensities of the PAH emission bands (Section 1.3.3). Conversely, we can use the observed relative PAH intensities to infer the charge state of a PAH population. Following this logic, two of the three spectral templates found with the BSS method were assigned to neutral and ionic PAH species with the ionic species peaking closer to the star. This assignment was confirmed by Rosenberg et al. (2011) by fitting each spectral template using the NASA Ames PAH IR Spectroscopic Database (PAHdb, Bauschlicher et al., 2010; Boersma et al., 2014b; Bauschlicher et al., 2018). In addition, the spatial distribution of individual PAH features show that the emission bands associated with PAH cations (i.e. 6.2, 7.7, and 8.6 μm) peak closer to the star, whereas the
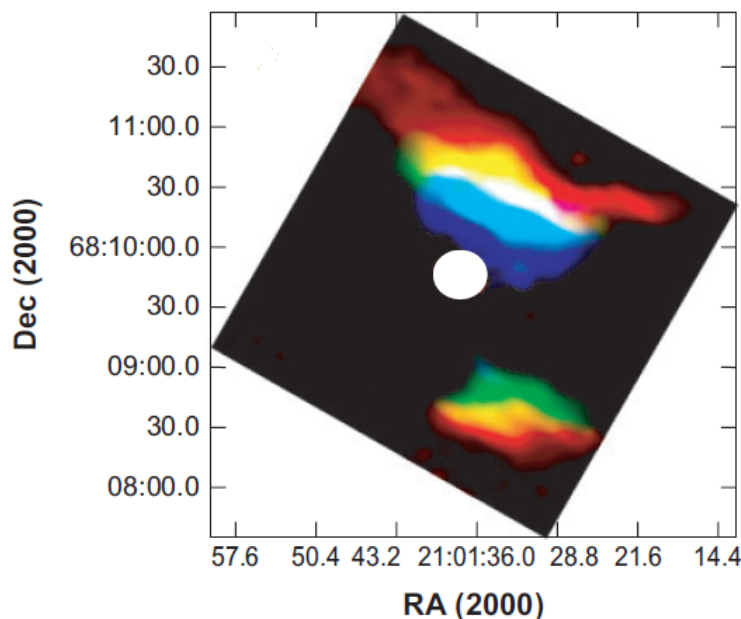
Figure 1.8: Distribution of three MIR emission components derived from BSS in NGC 7023: PAH ions (blue), PAH neutrals (green), and VSG (red). Figure from Berné et al. (2008), reproduced with permission © ESO.

bands indicative of neutral PAHs (i.e. 3.3 and 11.2 μm) peak further away from the star. This distribution further supports the picture of the photochemical evolution of astronomical PAHs as they become more ionized with increasing exposure to the UV radiation of the central star.

Size   PAH size is traced using the observed ratio of the 11.2/3.3 (Section 1.3.3). Indeed, a PAH size distribution can be constructed by comparing the observed ratio with the intrinsic 11.2/3.3 ratio from theoretical spectra of PAHs over a range of sizes expected to be found in the region (e.g. Bauschlicher et al., 2008, 2009; Ricca et al., 2012; Boersma et al., 2013; Croiset et al., 2016; Maragkoudakis et al., 2020), typically around 50 carbon atoms (Allain et al., 1996; Tielens et al., 1999). This PAH size distribution probes the photochemical evolution of PAHs by mapping how the average PAH size varies with distance to an illuminating source. Since smaller PAHs are less stable (e.g. Schutte et al., 1993), they are dissociated with less radiative energy and are expected to be found further from the illuminating star compared to their larger counterparts. Moving closer to the star, the average PAH size will increase as only the largest, most stable species can survive the increase in UV radiation (e.g. Andrews et al., 2015; Peeters et al., 2017). Thus, it follows that an observed change in PAH size is evidence of UV processing and is a suitable probe for the photochemical evolution of these species.

PAH Structure   Similar to the PAH charge and size, the edge structure of PAHs can be examined in finer detail through the spatial mapping of the relevant PAH emission features (Hony et al., 2001; Fleming et al., 2010; Boersma et al., 2013; Shannon et al., 2016). The

12.7/11.2 emission ratio is one such tracer of the edge structure (section 1.3.3). Changes in the edge structure of a PAH population can be analysed through measuring the spatial variations in each emission band upon correcting for charge state differences.

In addition, the 7–9 μm PAH emission features can be decomposed into four Gaussian components (G7.6, G7.8, G8.2, G8.6, Peeters et al., 2017; Stock & Peeters, 2017). The G7.6 and G8.6 components show the same spatial distribution, are well correlated and are both attributed to compact, symmetrical PAHs based on the PAHdb emission models. Similarly, the G7.8 and G8.2 are correlated, have a similar spatial distribution as the dust continuum emission and are attributed to irregularly edged PAHs with bay regions from the PAHdb models. Thus, these four spectral components of the 7–9 μm PAH emission provides another way to probe PAH structure.

Spatial Sequence of PAH Emission Features   In the reflection nebula NGC 2023, spatial variations of the PAH emission components were probed in finer detail by Peeters et al. (2017). Similar studies were done on the reflection nebula NGC 7023 by Boersma et al. (2013) and Shannon et al. (2015). The authors found that the peak emission of individual PAH bands as well as continuum emission showed a spatial sequence from the illuminating star. Each of these emission features were grouped based on location and assigned to different carriers based on the PAHdb.

The spatial sequence of the emission features and their assignments reveals the photochemical evolution of the PAH population driven by increased exposure to the UV radiation field from the central source within the evaporate flows of NGC 2023 (see Figure 1.9). Beginning from the edge of the molecular cloud, MIR emission is dominated by VSG and neutral PAH clusters with large irregular edges. Moving inwards towards the central star, these species are photoprocessed into very large PAHs with irregular edges with sizes between 100–150 carbon atoms, which are subsequently broken into neutral and cationic highly symmetrical compact PAHs at the PDR front (Andrews et al., 2015). Further inwards, more smaller irregular edged PAHs are found. In the cavity region closest to the star, only large, compact PAH cations (> 70 carbon atoms) and C_{60} can exist without being rapidly fragmented.

1.5   Photo-Dissociation Regions

PAHs reside in PDRs. The existence of PDRs, regions where far-ultraviolet (FUV) photons with energies > 6 eV and < 13.6 eV (the ionization energy of hydrogen) control the physics and chemistry of the gas, was initially prompted by observations of the fine structure lines [C II] 158 μm and [O I] 63 μm in massive star forming regions (Melnick et al., 1979; Storey et al., 1979; Russell et al., 1980, 1981). From these studies, the conclusion was drawn that primarily neutral, IR-luminous regions exist around H II regions surrounding young stars. Within these regions, molecules are photodissociated and elements with ionization potentials below 13.6 eV are photoionized by the FUV photons from nearby stars. However, the study of PDRs extends to the warm neutral medium, giant molecular clouds, RNe, the neutral gas enveloping PNe, the photodissociated winds of red giants and AGB stars, and the ISM within the nuclei of starburst galaxies and galaxies containing active galactic nuclei (Hollenbach & Tielens, 1999). Thus, all atomic and at minimum 90% of the molecular gas in the Galaxy is contained in
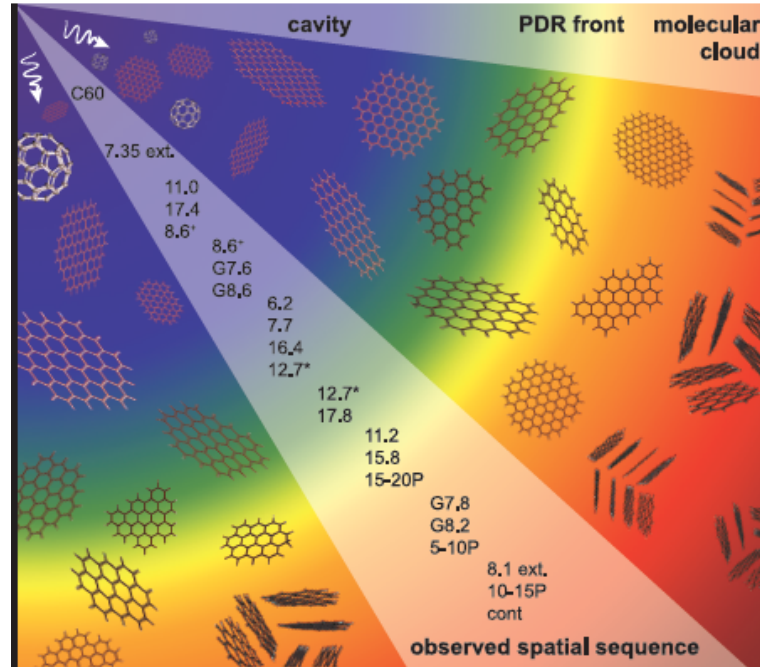
Figure 1.9: Diagram of the photochemical evolution of PAH population in NGC 2023. The changes in PAH structure with increasing exposure to the UV radiation field from the central star on the right upon transitioning from the PDR into the cavity are shown along with the prominent emission features associated with each class of PAH species. Figure from Peeters et al. (2017), reproduced by permission of the AAS.

PDRs (Hollenbach & Tielens, 1999). Observed emission from PDRs consist of the FIR dust continuum, PAH emission, H_2 emission, the atomic fine structure lines of [O I] and [C II], and CO rotational lines.

The morphology of a PDR can be understood in terms of a simple one dimensional schematic (see Figure 1.10). Consider a source of FUV flux, such as the interstellar radiation field (ISRF) or a nearby hot star, incident on a neutral gas cloud. A PDR is defined to begin at the H I/H II boundary, the ionization front (IF), where Lyman continuum photons dominate, and to end deeper into the cloud at the O/O_2 boundary. Moving inwards from the outer boundary, the gas is predominantly in the form of atomic hydrogen extending to depth of $A_V \sim 1$–2 from the ionization front. Eventually, there is a transition from H I to molecular hydrogen, with FUV-pumped H_2 emission peaking at the H I/H_2 interface. Other prominent atomic species found in PDRs are C and O, with C^+/C emission extending to a depth of $A_V \sim 2$–4 and atomic O emission extending to a depth of $A_V \sim 5$–10. In the case of diffuse clouds, PDRs only reach $A_V < 2$, thus contain primarily atomic gas. Within cooler, denser clouds, PDRs extend into regions where H becomes molecular and most of the C is in the form of CO. Significant FUV photochemistry involving free C and O atoms can persist up to $A_V \sim 10$. Typical values for G_0[3] range from the local average ISRF (~ 1.7, Draine, 1978) up to $> 10^6$ ergs/cm²/s in proximity to an O type star. The gas density, n, ranges from ~ 0.25 cm^{-3} in warm neutral gas up to

---

[3]integrated radiation flux from 6 to 13.6 eV in units of the Habing field = 1.6 x 10^{-3} ergs/cm²/s

$\sim 10^3$–10^7 cm^{-3} for regions including molecular gas.
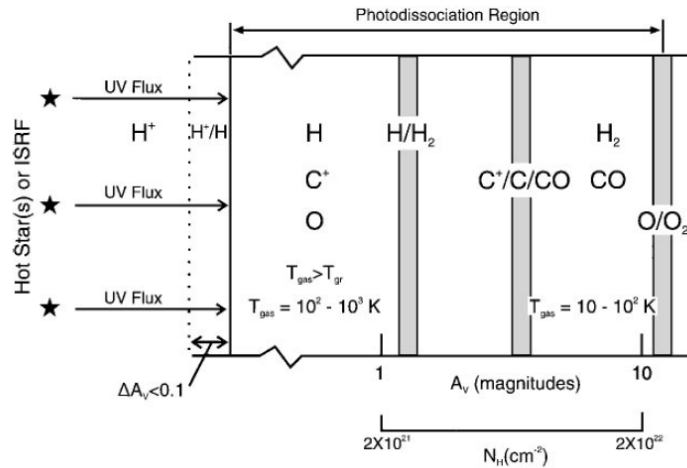
Figure 1.10: A schematic diagram of a photo-dissociation region. A strong UV flux from the left illuminates the PDR beginning at the H I/H II transition boundary up to a depth of $A_V \sim 10$ visual magnitudes, the transition boundary from primarily atomic O to O_2. A PDR will typically include a neutral atomic surface layer as well as a large molecular layer. Re-published with permission of G. Burbidge, from Hollenbach & Tielens (1997); permission conveyed through Copyright Clearance Center.

There are two principal heating mechanisms that couple the gas in the PDR to stellar FUV photon emission (Hollenbach & Tielens, 1997): (1) The absorption of a FUV photon of sufficient energy by a PAH species will cause an electron to be ejected. This free electron contributes to the gas heating through the transfer of kinetic energy upon colliding with other species present. The photoelectric heating will be significant when the PAH population is primarily neutral as a higher charge state translates into a higher ionization potential, decreasing the efficiency of this process. In other words, the photoelectric heating efficiency depends on γ, the PAH ionization parameter. (2) The FUV fluorescence of a H_2 molecule causes it to become vibrationally excited. This is followed by the IR fluorescence of H_2 or the collisional de-excitation of H_2 with another species in the gas depending on the gas density, thus contributing to the heating of the gas. The fraction of the FUV photon flux that excites H_2 depends on the H I/H_2 boundary, which depends on the physical conditions, G_0 and n.

Gas cooling in PDRs is mainly through the FIR fine structure lines, which include [C II] 158 μm, [O I] 63, 146 μm, [Si II] 35 μm, [C I] 609, 370 μm (Hollenbach & Tielens, 1997). The intensity of the FIR fine structure lines depends on the density of the gas layer from which the emission arises. If the gas density is above the critical density of the emitting species, collisional de-excitation becomes dominant returning the energy to the gas. Thus each fine structure line will only be present in the gas layers that are below the critical density of the emitter. In this way, different lines are used to probe different depths of a PDR. Consider Figure 1.11, in which the ratio of [C II] 158 μm/ [O I] 63 μm is plotted as a function of density for different temperatures. In the low density layers (n < n_{cr}([C II]) = 3×10^3 cm^{-3}), [C II] emission dominates cooling and the gas temperature is the only variable (Tielens, 2005). In high density layers

(n >> n$_{cr}$([O I]) = 5x10^5 cm^{-3}), [O I] cooling is dominant at each temperature regime. For intermediate densities (3x10^3 cm^{-3} < n < 5x10^5 cm^{-3}), the largest dependence on gas density is found.
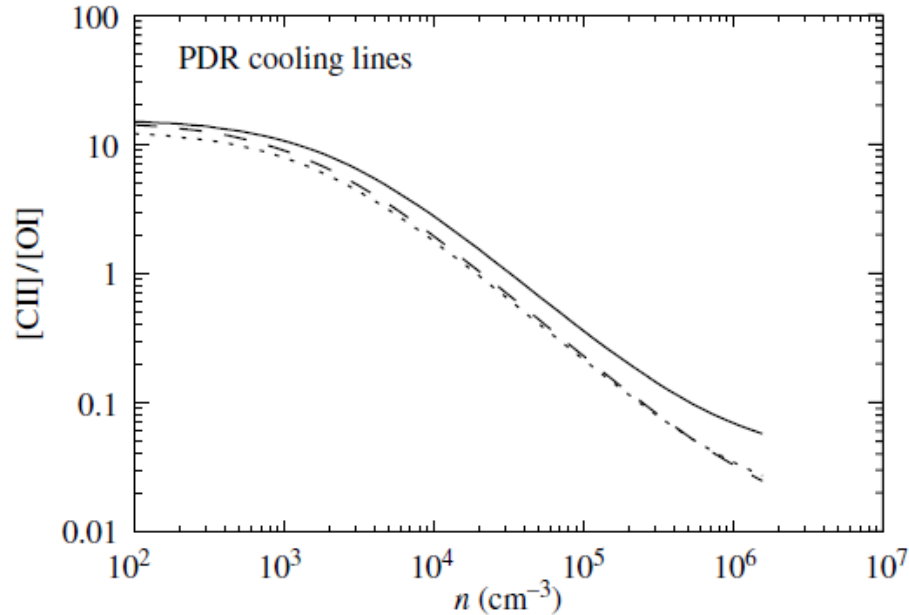
Figure 1.11: The ratio of the cooling from the [C II] 158 μm to the cooling from the [O I] 63 μm line as a function of the gas density at different temperatures: solid line, T = 100 K; dotted line, T = 250 K; dashed line, T = 1000 K. Figure from Tielens (2005), reproduced with the permission of Cambridge University Press through PLSclear.

1.5.1 PDR models

Theoretical models serve as a bridge to compare observations with calculations of physical parameters. Tielens & Hollenbach (1985b) developed a novel PDR model to describe the gas heating and cooling based on assumptions of the gas chemistry and the thermal balance of dense neutral gas illuminated by FUV photons. This model was then applied to a prototypical PDR, the Orion Bar (Tielens & Hollenbach, 1985a; Tielens et al., 1993). These authors assumed a one dimensional plane-parallel semi-infinite slab illuminated on one side by FUV radiation. Their model for the Orion Bar region is quantitatively shown in Figure 1.12, where the abundance of significant species, the temperatures of gas and dust, and the FIR cooling lines are calculated as a function of visual magnitude. There have since been more sophisticated PDRs model that have iterated upon this original model (e.g. Kaufman et al., 1999, 2006; Hollenbach et al., 2012; Wolfire et al., 1990, 2010).
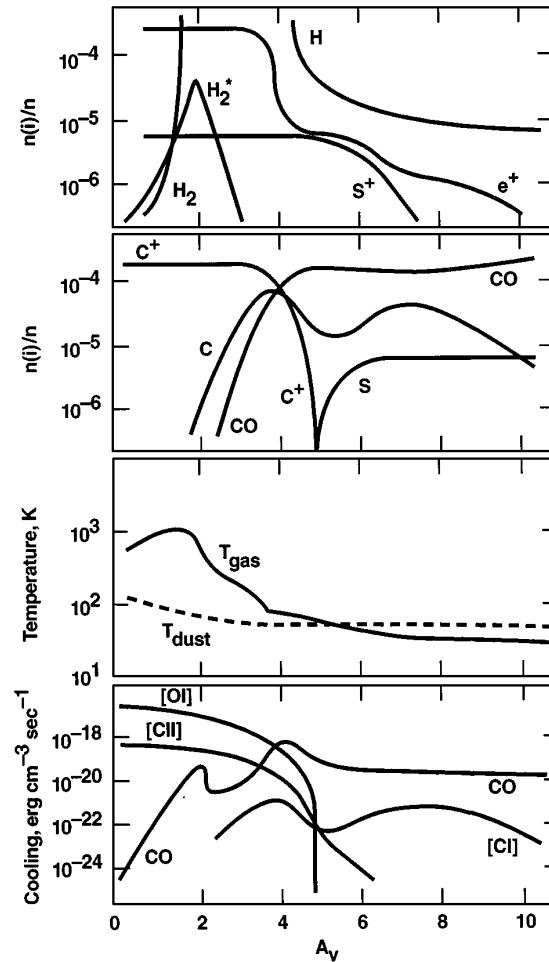
Figure 1.12: Calculated structure of the Orion PDR as a function of visual extinction, A_V, with the illuminating source on the left. The top two panels show the abundances of relevant species to H abundance. The third panel shows the gas and dust temperatures. The bottom panel gives cooling rates from prominent gas lines. Republished with permission of G. Burbidge, from Hollenbach & Tielens (1997); permission conveyed through Copyright Clearance Center.

1.5.2   FIR PDR Diagnostics

The FIR fine structure lines can be used to derive the physical conditions within a PDR. As a result, diagnostic diagrams using the line ratios of the bright PDR cooling lines such as [O I] and [C II] are able to probe the density and temperatures within a PDR. This is due to the critical densities and excitation energies of these species spanning the range of conditions found in PDRs.

One example of a diagnostic diagram illustrates how the ratio [O I] 63/[C II] 158 depends on the physical parameters G_0 and n (see Figure 1.13). The [O I] 63 μm/[C II] 158 μm ratio is approximately constant for a fixed value n for $G_0 > 10^4$. At low G_0, the decrease in the intensity of the 63 μm line is much greater than in the 158 μm line, causing a decrease in the ratio at densities $< 10^4$ cm^{-3}. As the critical density of the [O I] 63 μm line, $\sim 5 \times 10^5$ cm^{-3}, is

much higher than the [C II] 158 μm line, n > 3x10^3 cm^{-3}, [O I] 63 μm intensity continues to increase with density whereas the [C II] 158 μm intensity remains constant for G_0 < 10^2 and n > 3x10^3 cm^{-3}. It is clear that there is no simple dependence between the line emission and the physical parameters. To obtain singular values for these parameters, multiple diagnostics must be used to find where these values intersect (e.g. Wolfire et al., 1990; Kaufman et al., 1999).
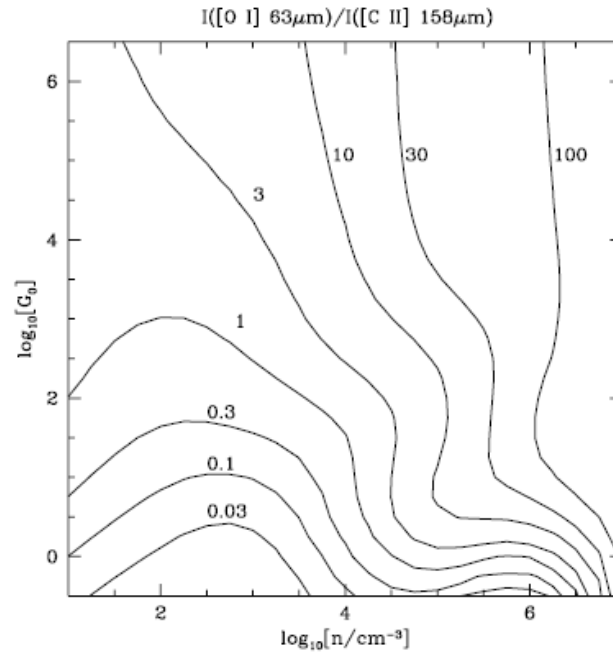
Figure 1.13: Ratio of the [O I] 63 μm line intensity to the [C II] 158 μm line intensity emitted from a PDR surface as a function of gas density and incident FUV flux. Figure from Kaufman et al. (1999), reproduced by permission of the AAS.

1.5.3 PAHs as PDR Diagnostics

Recently, PAH emission has been explored as a quantitative probe of the environmental conditions within a PDR. Galliano et al. (2008) have derived an empirical relationship between the 6.2/11.2 intensity ratio and the PAH ionization parameter, γ, based on the observations of three well studied PDRs where the physical conditions had already been constrained (see Figure 1.14). Boersma et al. (2015) also found a correlation between the 6.2/11.2 intensity ratio and γ by fitting spectral data of NGC 7023 with a selection of PAHs from the PAHdb. However, these relationships disagree with each other by about an order of magnitude. The Boersma et al. (2015) method may be influenced by the bias towards the PAH species found in the PAHdb and the applied conversion of the ionization fraction to γ, whereas the Galliano et al. (2008) method suffers from uncertainties in deriving the physical conditions and a mismatch in apertures (or FOV) of the MIR and FIR observations. Additionally, they are both unable to distinguish between individual physical parameters within γ. Thus, by deriving the ionization

parameter using the Boersma et al. (2015) method and comparing it with the observed ionization parameter derived from PDR cooling line and FIR dust emission measurements observed in the same aperture and spatial resolution as the MIR PAH emission, we can fine-tune and/or validate this method and investigate the discrepancy between both methods.
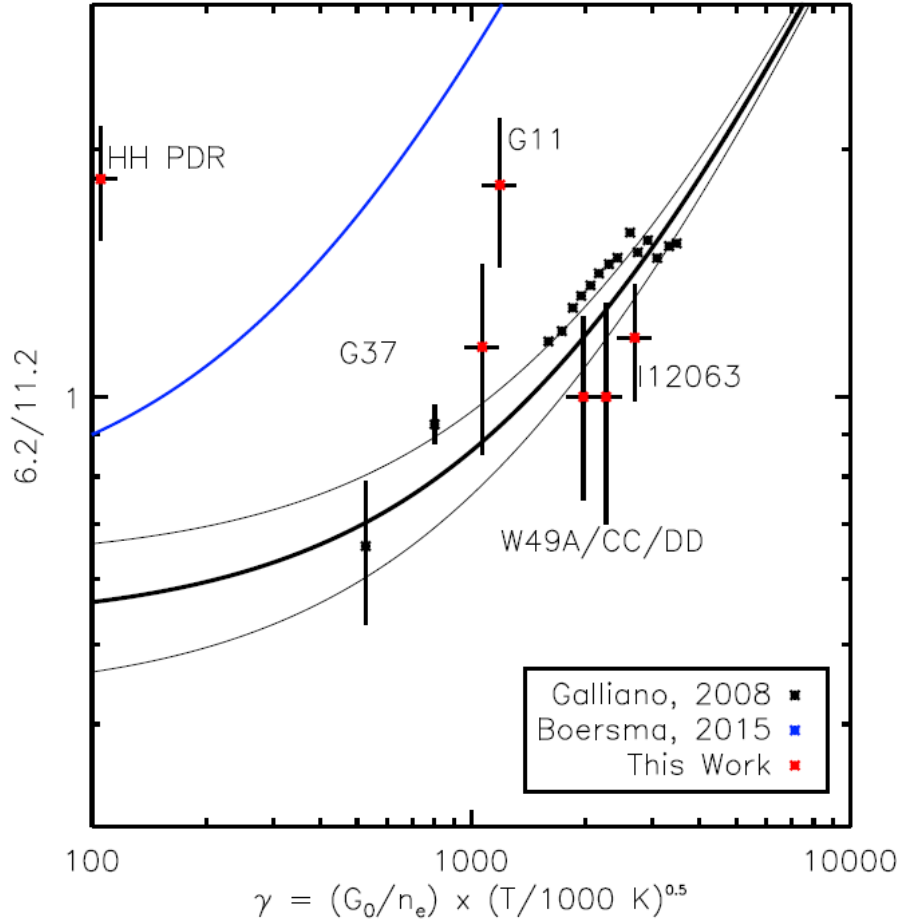
Figure 1.14: Empirical relationship between the 6.2/11.2 emission ratio and γ, the ionization parameter. The black thick line is the linear relationship found by Galliano et al. (2008), with the thinner lines being the 1 σ deviations. The blue line is the relationship derived from PAHdb fitting of NGC 7023 by Boersma et al. (2015). Figure from Stock et al. (2016), reproduced by permission of the AAS.

Ratios of the sub-components of the 7.7 μm complex are also found to be closely related to the environmental conditions (see Figure 1.15, Stock & Peeters, 2017). It was found that the 7.8/7.6 intensity ratio was linearly related to G_0. The red solid line is a fit to data points which have a literature prediction for G_0, whereas the blue dashed line includes two ISO diffuse ISM spectra. Note that there are much fewer sources for low G_0 values leading to more uncertainty in what the nature of a typical PAH spectrum looks like for low G_0. Stock et al. (2014) have argued that the diffuse emission surrounding the H II region, W49A is a good representative for the PAH spectrum in a diffuse ISM as the majority of the emission is emitted along the

line of sight instead of near the H II region. This relationship can be further investigated using spatially resolved observations of PDRs cooling lines for a wide range of sources with matching positions and apertures as the current PAH emission observations, with an emphasis on increasing the sample size of PDRs with low G_0.
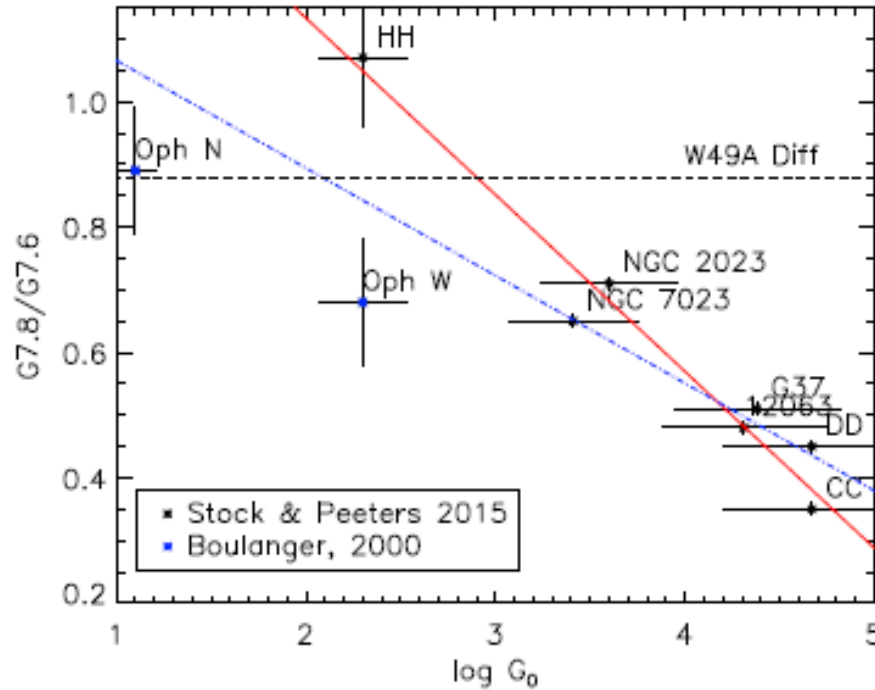
Figure 1.15: Correlation between the 7.8/7.6 emission ratio and the UV field intensity, G_0. The red solid and blue dashed line are fits to the black points and the black and blue points respectively. The dashed line is the maximum 7.8/7.6 emission ratio found in the outskirts of the H II region, W49A. Figure from Stock & Peeters (2017), reproduced by permission of the AAS.

BSS analysis has the ability to decompose a spectral map of PAH emission into three distinct components (Section 1.4.2). Based on this analysis, the fitting tool PAHTAT has been developed (Pilleri et al., 2012). PAHTAT enables these spectral components to be extracted in the absence of a spectral map. Using this tool, an empirical relation between the fraction of carbon atoms locked within VSG and G_0 was derived providing another way to probe PDR conditions based on VSG emission (Pilleri et al., 2012). This relationship shows a decrease in the fraction of carbon atoms locked in VSG with increasing G_0, implying an increase in UV processing will cause the fragmentation or destruction of these species. It should be noted that this method does not work for H II regions because it is unable to correctly measure the rise in dust continuum emission.

1.6   The Interplay of PAHs and their Environment: Thesis Outline

1.6.1   Investigating PAH properties in Nearby Prominent Mid–Infrared Environments

The photochemical evolution of astronomical PAHs is evident throughout the ISM (section 1.4). Within nearby MIR bright regions, observed spatial variations in the PAH emission and PAH abundance are attributed to changing physical conditions. For example, an in-depth study of the RN NGC 7023 has shown evidence for the importance of the photo–destruction of PAHs and the subsequent formation of C_{60} (section 1.4.2). Nearby PDRs, such as the RNe NGC 1333, NGC 2023, NGC 7023 and the Orion Bar, provide an ideal location to investigate this photo-chemical evolution. The study of the PAH population in these regions allow us to critically test the interpretation of UV processing driving variations in the spatial and spectral characteristics of the PAH emission as well as the underlying properties of the emitting species.

This photochemical evolution of PAHs is investigated by quantitatively measuring the PAH size distribution, the degree of ionization of these species and by characterizing the spatial behaviour of the various components of the PAH emission. The PAH size distribution is mea-sured through spatially mapping the observed 3.3/11.2 emission ratio and comparing with the intrinsic 3.3/11.2 emission ratio based on theoretically or experimentally calculated emission spectra of PAHs available in PAHdb (section 1.3.3). We can then use this size distribution to indicate the presence of significant UV processing within these regions (Chapter 2). Similarly, spatial variations in the relative ionization state of PAHs can be mapped using ratios of emis-sion features related to ionized and neutral PAH species respectively (e.g. 7.7/11.2, section 1.3.3, Chapter 2). Additionally, we use spectral maps to determine how spatial variations of the relative intensities of the PAH emission features are related to their environment (Chap-ter 4). We compare the relative behaviour of these PAH bands in a highly irradiated nebula with the surrounding diffuse ISM to demonstrate how some of these bands can be attributed to multiple PAH subpopulations (Chapter 4).

In nearby spatially–resolved sources, we can also consider the effect that the relative ori-entation (such as edge–on or face–on) of the PDR structure to the source of UV photons has on the observed PAH emission as well as on other atomic and molecular species found within PDR environments (Chapter 3). In short, for a purely edge–on PDR, we can clearly differen-tiate between the the level of UV processing of different gas layers (i.e. material closer to the illuminating source will be increasingly processed as it has been exposed to a higher intensity of UV photons). Hence, for edge–on PDRs such as the Orion Bar, we can test how previously established correlations between the PAH emission features hold up with respect to exposure to the FUV radiation field. In contrast, within a face–on PDR, we observe multiple gas layers with varying degrees of UV processing within a given beam, making it much more difficult to gauge the photochemical evolution of a PAH population in these regions.

1.6.2 PAHs as Environmental Tracers

The PAH emission features clearly depend on environmental conditions as seen in a wide range of sources (see section 1.5.3). Previously established empirical relationships between PAH emission and PDR physical conditions show promise in the use of the PAH emission features as diagnostic tools for both Galactic and extragalatic PDR studies. In the case of extragalactic PDRs, such a PAH diagnostic tool would be invaluable due to the primary PDR cooling lines being difficult to observe in these sources. However, there are some discrepancies in the established empirical relationships that require further investigation.

We compare the PAH emission features and the physical conditions in two nearby PDR environments, the Orion Bar and the RN NGC 1333. In Chapter 3, we use the same assumptions about the physical conditions for the Orion Bar as was done in by Galliano et al. (2008) to derive line profiles for G_0 and the ionization parameter, γ. In Chapter 4, we use spatially resolved measurements of the FIR cooling lines and FIR dust continuum emission to compute the physical conditions (G_0, T, and n_e) for NGC 1333. Maps of the physical conditions in NGC 1333 are derived by calibrating the FIR cooling lines and FIR dust continuum emission with theoretical PDR models. We compare the PAH emission features with the physical conditions at matching spatial resolution and aperture size in both the Orion Bar and NGC 1333. This enables us to test the previously established empirical relationships and potentially derive new relationships between PAHs and their environment.

Chapter 2

Tracing PAH Size in Prominent Nearby Mid-Infrared Environments

C. Knight[1], E. Peeters[1,2,3], D. J. Stock[1], W. D. Vacca[4], A. G. G. M. Tielens[5]
Submitted to MNRAS.

[1]*Department of Physics and Astronomy, University of Western Ontario, London, ON N6A 3K7, Canada; cknigh24@uwo.ca*

[2] *Institute for Earth and Space Exploration, University of Western Ontario, London, ON, N6A 3K7, Canada*

[3]*Carl Sagan Center, SETI Institute, 189 N. Bernardo Avenue, Suite 100, Mountain View, CA 94043, USA*

[4]*SOFIA-USRA, NASA Ames Research Center, MS N232-12, Moffett Field, CA 94035-1000, USA*

[5]*Leiden Observatory, PO Box 9513, 2300 RA Leiden, The Netherlands*

2.1 Introduction

The mid-infrared (MIR) spectra of many astronomical sources are dominated by emission features at 3.3, 6.2, 7.7, 8.6, 11.2, and 12.7 μm, attributed to the infrared (IR) fluorescence of Polycyclic Aromatic Hydrocarbon molecules (PAHs, e.g. Allamandola et al., 1985; Léger & Puget, 1984). It has been well established that PAH molecules with sizes from $50 - 100$ carbon atoms are the carriers of these bands (e.g. Allamandola et al., 1989; Puget & Léger, 1989). In recent works, different authors have adopted various monikers to refer to these features such as the aromatic emission features (AEFs, e.g. Werner et al., 2004a), the aromatic infrared bands (AIB, e.g. Croiset et al., 2016) or simply referred to them as the PAH emission features (e.g. Boersma et al., 2012; Peeters et al., 2012, 2017). Other related species are also considered to be carriers such as polycyclic aromatic nitrogen heterocycles (PANHs, Hudgins et al., 2005; Bauschlicher et al., 2008) or PAHs with functional groups attached (e.g. Joblin et al., 1996a; Sloan et al., 1997; Pilleri et al., 2015; Maltseva et al., 2016; Shannon & Boersma, 2019). These PAH emission features have been found in wide variety of Galactic and extragalactic sources such as H II regions, reflection nebulae (RNe), post-AGB stars, planetary nebulae (PNe), the diffuse interstellar medium, and galaxies (e.g. Sellgren et al., 1996; Hony et al., 2001; Peeters et al., 2002; Verstraete et al., 2001).

The PAH emission features show variations in intensities, peak positions, and band profiles (e.g. Bregman et al., 1989; Hony et al., 2001; Peeters et al., 2002; Galliano et al., 2008).

Relative intensity variations reveal how these bands relate to each other and to the intrinsic properties of these species. The 6.2, 7.7, 8.6 μm bands are well correlated over a wide range of environments (Joblin et al., 1996a; Galliano et al., 2008). Likewise, the 3.3 and 11.2 μm bands are well correlated (Russell et al., 1977; Hony et al., 2001) but do not strongly correlate with the 6–9 μm PAH bands. Laboratory and quantum chemical studies show that the most significant driver of these intensity variations is the PAH charge state: 6.2, 7.7, 8.6 μm bands are prominent in ionized PAHs, whereas the 3.3 and 11.2 μm bands are strongest in neutral PAHs (e.g. Allamandola et al., 1989; Bauschlicher et al., 2008). This in turn is strongly dependent upon the UV radiation field of nearby stellar sources incident upon the environment in which these PAHs reside (as well as local gas density and temperature, e.g. Tielens, 2005; Galliano et al., 2008; Boersma et al., 2013; Stock et al., 2016; Stock & Peeters, 2017; Peeters et al., 2017).

The MIR spectra can be strongly influenced not only by ionization, but also by changes in the chemical structure of these species. In particular, changes in PAH size can be traced by relative intensity variations within an extended region (e.g. Mori et al., 2012; Croiset et al., 2016). We investigate the PAH size distribution through the measurement of the 11.2/3.3 PAH intensity ratio in the photodissociation regions (PDRs) adjacent to three astronomical sources: two reflection nebulae (RNe): NGC 2023 and NGC 7023; and the region southeast from the Orion Bar. RNe are ideal test beds for the study of the PAH emission bands as they have strong MIR emission and have a well defined structure without contamination from atomic lines (i.e. Sellgren, 1983; Rapacioli et al., 2005; Berné et al., 2007; Boersma et al., 2013, 2016), whereas the Orion Bar has long been considered the prototypical photodissociation region (PDR Tielens & Hollenbach, 1985a), i.e. regions where far-ultraviolet (FUV) photons with energies between 6 eV and 13.6 eV control the physics and chemistry of the gas.

In this paper, we relate the PAH sizes in each source considered (NGC 2023, NGC 7023, and the region southeast of the Orion Bar) to other properties of these species as well as the physical characteristics of their PDRs. Section 2.2 details the properties of each of the sources studied here. In Section 2.3, the observations used in this study are detailed while in Section 2.4, the data reduction performed is discussed. Section 4.5 presents the results of our analysis in the form of spatial maps of emission feature ratios and line projections of these ratios extending from the illuminating sources. These results are discussed in Section 2.6 and conclusions are given in Section 2.7.

2.2 Astronomical Sources

For our analysis, we selected three well known sources that show prominent PAH emission features. We briefly summarize the general morphology and properties of these sources relevant to this study below.

NGC 2023   NGC 2023 is a well-known RN illuminated by the B1.5V type star, HD 37903, and located at a distance of 403 ± 4 pc (Kounkel et al., 2018). Its MIR emission has been the focus of many studies over the past 40 years (e.g. Sellgren, 1984; Gatley et al., 1987; Abergel et al., 2002; Peeters et al., 2012, 2017). It shows the same morphology at a wide range of wavelengths: a limb-darkened shell or a 'bowl' shaped PDR surrounding the interior cavity

(Figure 2.1). We can see into the various layers of the PDR along with some diffuse filamentary structure throughout the RN. PDR models of the cavity have shown a FUV radiation field strength of ∼ 4000 times that of the average interstellar field (position H5, Steiman-Cameron et al., 1997) as well as gas densities ranging from 10^4 to 10^5 cm^{-3} (e.g. Burton et al., 1998; Wyrowski et al., 2000; Sandell et al., 2015). We focus our study of this RN to the south of HD 37903, where the presence of multiple MIR emission peaks are suggestive of significant PAH emission along the PDR boundaries and are associated with the densest gas structures in the region. These peaks are labelled as in Peeters et al. (2017) as the S ridge, the SSE ridge, the SE ridge and the S' ridge.

NGC 7023   NGC 7023 is another RN that is well-known for its strong MIR emission (e.g. Cesarsky et al., 1996; Boissel et al., 2001; An & Sellgren, 2003; Werner et al., 2004a; Rapacioli et al., 2005; Berné & Tielens, 2012; Boersma et al., 2013, 2014a). It is illuminated by the Herbig Be star, HD 200775, and is located at a distance of 361 ± 6 pc (Gaia Collaboration et al., 2016, 2018). There are three main regions of study located around this star: 40″ northwest, 70″ south, and 170″ east (Berné et al., 2007). Each of these regions coincides with a PDR front. In Figure 2.2, only the NW and S PDR are visible. The NW PDR is the most prominent of the three with an edge-on structure in which clear stratification of emission is visible (e.g. Pilleri et al., 2012). Estimates for the UV radiation field strength at the NW PDR front are 2600 times that of the average interstellar value with gas densities on the order of 4×10^3 cm^{-3} (Chokshi et al., 1988). Due to its prominence, the NW PDR of NGC 7023 is the focus of our study of this RN.

Orion Bar   The Orion Bar or Bright Bar refers to the ionization ridge in the Orion Nebula or the interface between the H II region and PDR located at a distance of 414 ± 7 pc (Menten et al., 2007). The MIR emission within the Orion Bar has been well studied showing a stratified plane-parallel structure in which different species peak at a range of distances from the source of UV radiation, θ^1 Ori C (e.g. Aitken et al., 1979; Sellgren, 1981; Bregman et al., 1989; Geballe et al., 1989; Sellgren et al., 1990; Tielens et al., 1993; Giard et al., 1994; Cesarsky et al., 2000; Rubin et al., 2011; Boersma et al., 2012; Haraguchi et al., 2012). In Figure 2.3, the Bar structure is quite prominent as it separates the extremely bright Trapezium Cluster responsible for the production of the strong UV radiation field in the northwest from the relatively colder, lower density region extending southeast from the Bright Bar. The faint foreground Veil region along the outer edges of the Orion Nebula can also be seen, extending from the northeast to southeast of Figure 2.3. PDR models of the Orion Bar suggest a gas density of 5×10^4 cm^{-3} and FUV radiation field strength of 4×10^4 times that of the average interstellar value (e.g. Tauber et al., 1994). The UV field of the H II region surrounding θ^1 Ori is expected to be too harsh to allow a significant PAH population to prosper. Indeed, most of the MIR emission to the north of the Orion Bar is associated with warm dust within the ionized gas (Salgado et al., 2016). Thus our study of the Orion Nebula extends beyond the PDR front within the Bright Bar southwards towards the outer Veil.
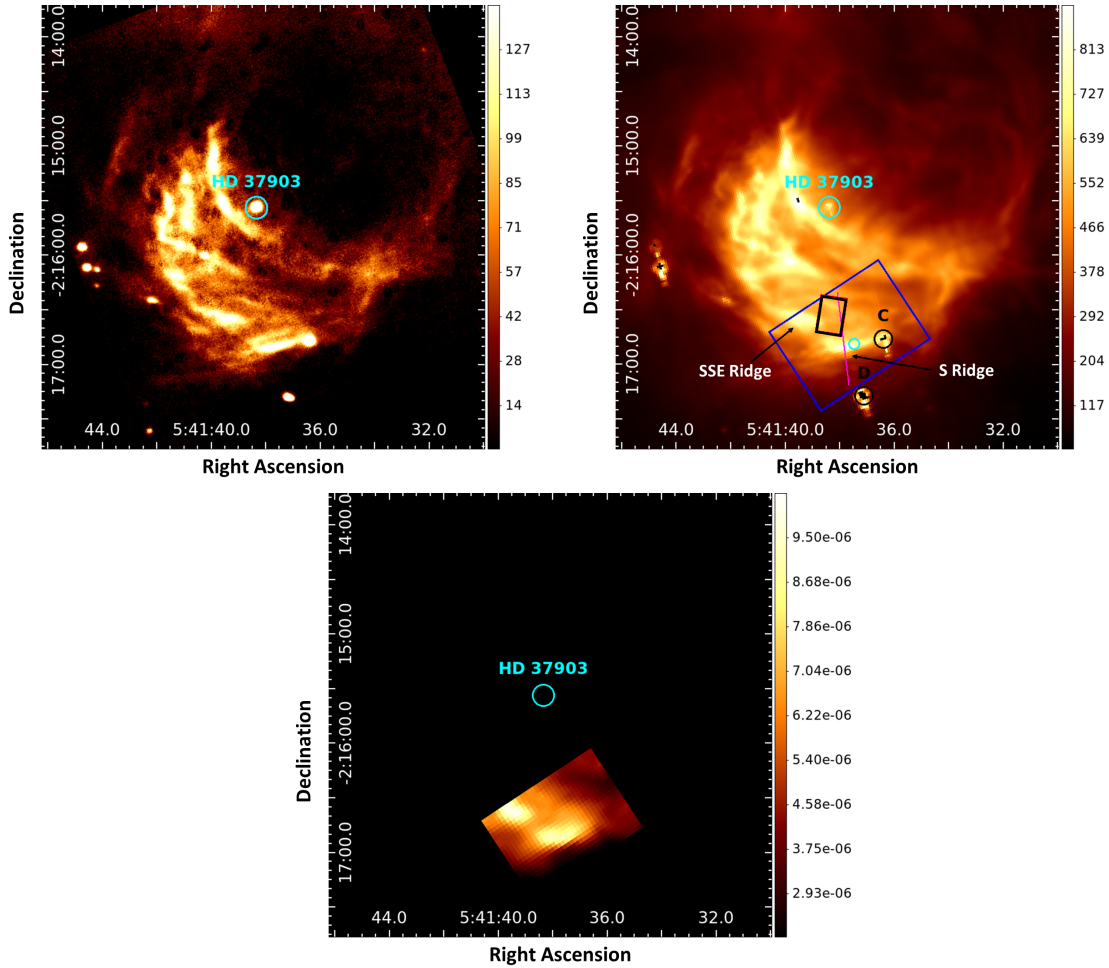
Figure 2.1: FLITECAM 3.3 μm (top left), IRAC 8.0 μm (top right),a nd the 11.2 μm band extracted from IRS SH (bottom center) observations of NGC 2023. The illuminating star, HD 37903 is indicated by a cyan circle, the young stellar objects, C and D, are indicated by black circles, the south IRS SH FOV by a blue rectangle, the ISO-SWS FOV by a black rectangle and the crosscut used for the line profile by a magenta line. The south ridge and south-southeast ridge as referred to by Peeters et al. (2017) are labelled by S Ridge and SSE Ridge respectively. A 2MASS point source embedded within the S Ridge is indicated by a small cyan circle (see Section 2.6). The units are surface brightness (MJy sr^{-1}) for FLITECAM 3.3 μm and IRAC 8.0 μm images and integrated fluxes (W m^{-2} sr^{-1}) for the 11.2 μm image.
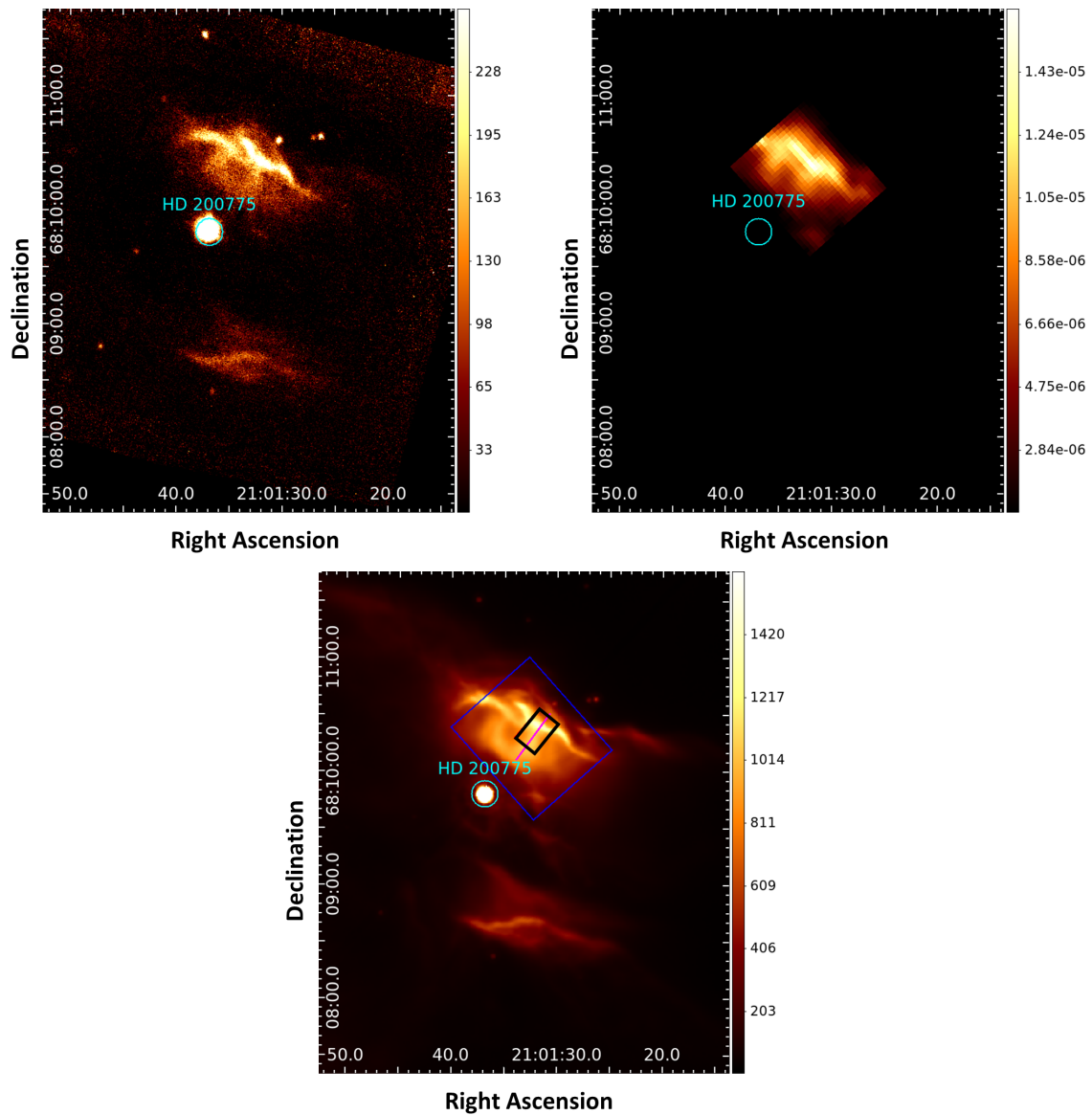
Figure 2.2: FLITECAM 3.3 μm (top left), IRAC 8.0 μm (top right), and the 11.2 μm band extracted from IRS SH (bottom center) observations of NGC 7023. The illuminating star, HD 200775, is indicated by a cyan circle, the northwest IRS SH FOV by a blue rectangle, the ISO-SWS FOV by a black rectangle and the crosscut used for the line profile by a magenta line. We use the same units as given in Figure 2.1.
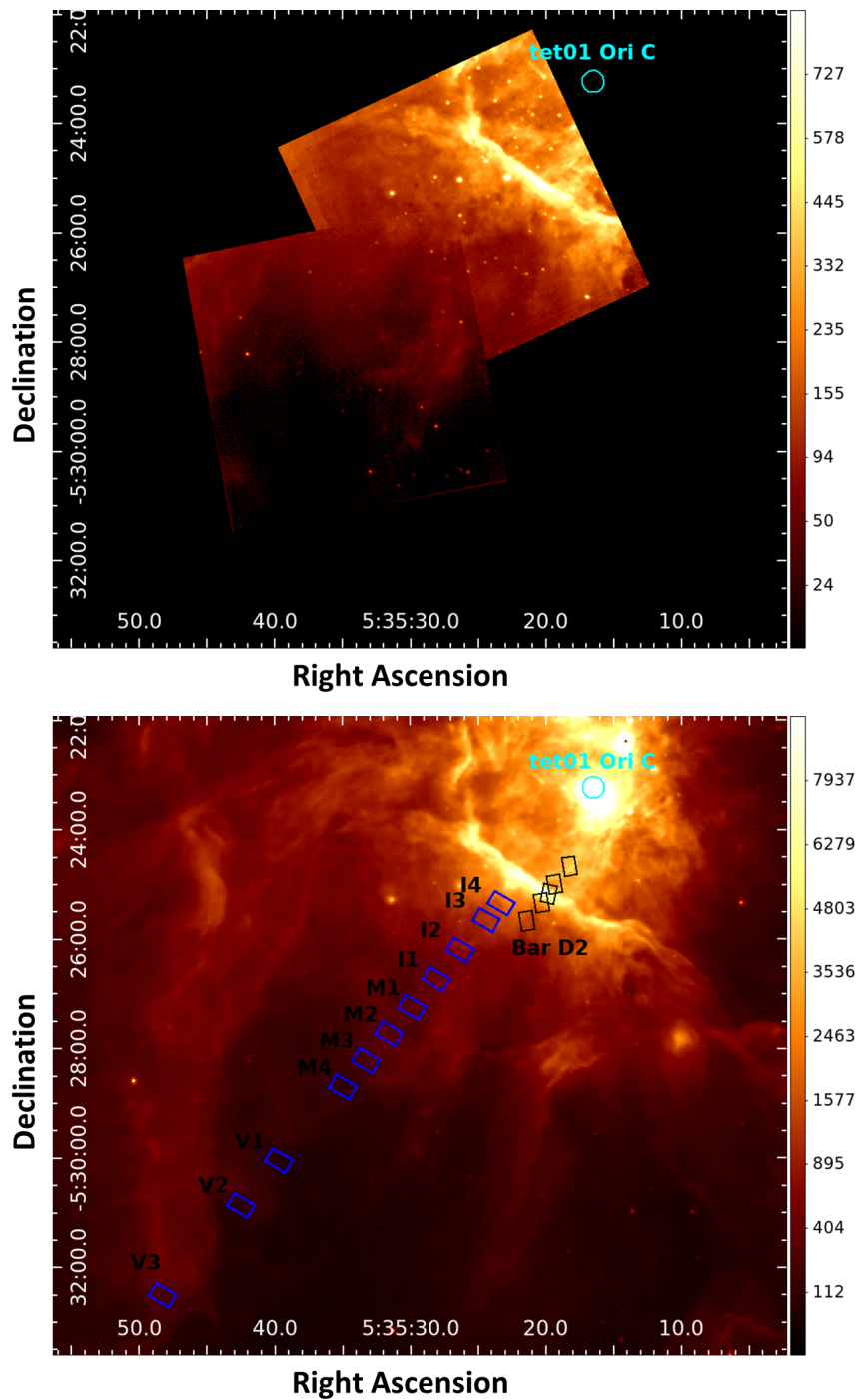
Figure 2.3: FLITECAM 3.3 μm (top) and IRAC 8.0 μm (bottom) observations of the Orion Nebula. The position of the illuminating source, θ^1 Ori C, is indicated by a cyan circle, the IRS SH maps for each position specified in Rubin et al. (2011) by blue rectangles, and the ISO-SWS FOVs by black rectangles. We note that the FLITECAM 3.3 μm and IRAC 8.0 μm images use a square root scale to show the entire range in emission structure. We use the same units as given in Figure 2.1.

2.3   Observations

We used multiple MIR observations to measure the dominant PAH emission bands. First, we obtained photometric observations from the First Light Infrared TEst CAMera (FLITECAM, Temi et al., 2012) on–board the Stratospheric Observatory for Infrared Astronomy (SOFIA, Young et al., 2012) to probe the 3.3 μm PAH emission. Second, PAH emission in the 7–9 μm range was investigated using observations from the Infrared Array Camera (IRAC, Fazio et al., 2004) on–board the Spitzer Space Telescope (Werner et al., 2004b). Finally, the 11.2 μm PAH emission was extracted from observations in the short-high mode (SH) of the Infrared Spectrograph (IRS, Houck et al., 2004) on–board the Spitzer Space Telescope. These observations are detailed below and are summarized in Table 2.1.

2.3.1   SOFIA observations

We obtained SOFIA-FLITECAM observations in the 4th to 6th cycles for both NGC 2023 (Figure 2.1) and two pointings towards the southeast of the Orion Bar (Figure 2.3) in the 'PAH' filter, which has an effective wavelength of 3.302 μm and a bandwidth of 0.115 μm (PID: 04_0058, PI: A. Tielens). The FLITECAM instrument has a 1024 pixel $\times$ 1024 pixel InSb detector that covers a 8 arcmin $\times$ 8 arcmin area on the sky with 0.475 arcsec $\times$ 0.475 arcsec pixels.

The NGC 2023 field of view (FOV) is centered on the central star, HD 37903, while the Orion FOVs were chosen such that they are centered on the Spitzer-IRS SH pointings I2 and M2 as defined in Rubin et al. (2011), which probe the region southeast of the Orion Bar, in order to cover all the Spitzer-IRS SH pointings closest to the Trapezium cluster observed by Rubin et al. (2011). To account for background emission, the instrument was used in nod mode, where the nod parameters were set so that the telescope was moved sufficiently off source between each observation. In the case of NGC 7023 (Figure 2.2), we have used SOFIA-FLITECAM archival data previously published by Croiset et al. (2016). The FLITECAM 3.3 μm images were found to have a point source FWHM of $\sim$ 2.1 arcseconds.

2.3.2   Spitzer observations

We obtained Spitzer-IRAC 8.0 μm observations (channel 4) of each source (see Figures. 2.1, 2.2, and 2.3). The IRAC 8.0 μm band is a broadband filter with a bandwidth of 2.9 μm and a nominal wavelength of 7.87 μm, and is found to be an excellent tracer for the Σ7–9 μm PAH emission (e.g. Smith et al., 2007a; Stock et al., 2014, see Appendix A.1). The IRAC 8.0 μm observations were found to have a point source FWHM of 2 arcseconds.

For each source, we measured the 11.2 μm PAH emission using IRS SH data, which covers the wavelength range of 10–20 μm at a spectral resolution of 600. IRS SH spectral maps were obtained over a portion of the nebula for both NGC 2023 and NGC 7023 (see Figures. 2.1 and 2.2 respectively). The spectral map of NGC 2023 covers the S and SSE emission ridges (following the nomenclature of Peeters et al. 2017) as well as YSO C defined by Sellgren (1983). The spectral map of NGC 7023 is comprised of the region surrounding the NW PDR. For Orion, we use IRS SH pointings taken along a line from 2.1 to 12.1 arcminutes extending

radially away from the illuminating source θ^1 Ori C near the Bright Bar (Rubin et al., 2011; Boersma et al., 2012). The spectra obtained for each pointing correspond to a 2×10 aperture grid pattern or 'chex' of SH spectra (for details, see Rubin et al., 2011). The resulting FOV of each of these pointings ($25.4'' \times 16.3''$) and the position of each pointing are shown in Figure 2.3. These pointings are given the following designations by Rubin et al. (2011) with increasing distance from the Bar: 'inner' (I4, I3, I2, I1), 'middle' (M1, M2, M3, M4), and 'veil' (V1, V2, V3).

2.4 Data Processing

The same general reduction procedure was used for all sources to generate emission ratio maps.

2.4.1 FLITECAM

To extract the 3.3 μm emission feature, the raw FLITECAM frames were co-added using a noise weighted mean into a single image and flux calibrated using standard stars observed during the same night as the observations. These images were slightly misaligned with respect to the IRAC 8.0 μm images. We correct for this misalignment by shifting our FLITECAM images to align with the IRAC 8.0 μm images. The FLITECAM images are converted from units of surface brightness (Jy pixel^{-1}) to flux (W m^{-2} sr^{-1}) by multiplying by the bandwidth of the FLITECAM filter, assuming a nominal flat spectrum. This is done in order to have comparable units with the 11.2 μm emission extracted from the IRS SH spectra.

Reflection Nebulae

In the case of NGC 7023, we obtained a single set of observations for which it was necessary to rotate the FLITECAM image to get the NW and S PDRs to overlap with respect to the IRAC 8.0 μm image (Croiset et al., 2016). In the case of NGC 2023, we obtained three sets of observations. Each of these three FLITECAM frames had a significantly high median on-frame background level that is subtracted from each frame (755, 357, and 224 MJy sr^{-1}) after which they are combined in a single image. We checked the absolute calibration for both sources in two ways. First, by comparison with ISO-SWS observations[1]. In particular, we checked the absolute flux calibration of the ISO-SWS spectra with IRAC 3.6 μm observations by comparing the observed IRAC 3.6 μm emission with the expected value in the IRAC 3.6 μm bandpass based on the ISO-SWS spectrum. We found a consistency of 90% and 98% for NGC 7023 and NGC 2023 respectively, indicating that the ISO-SWS spectra are well calibrated in an absolute sense. Subsequently, we compare the FLITECAM emission observed in the ISO-SWS aperture with the expected FLITECAM emission based on the ISO-SWS spectrum. We found an agreement of 100% and 104% for NGC 7023 and NGC 2023 respectively, indicating that the FLITECAM images are well calibrated. Second, by comparison with photometry of

---

[1]Based on observations with ISO, an ESA project with instruments funded by ESA Member States (especially the PI countries: France, Germany, the Netherlands and the United Kingdom) and with the participation of ISAS and NASA. The TDT (Target Dedicated Time) number is 20700801 and 65602309 for respectively NGC 7023 and NGC 2023.

Table 2.1: Log of observations.

Data	SNR[1]	RA[2]	DEC[2]	Nod ($''$, $°$)[3]	Exp.[12] (s)
NGC 2023					
FC[4]	12	5 41 37.89	-2 15 52.2	1000, 245	460
IRS SH[5]		5 41 37.63	-2 16 42.5		
IRAC 8.0[6,7]	46	5 41 37.89	-2 15 52.2		
NGC 7023					
FC[4,8]	76	21 01 36.92	68 09 47.7	600, 0	50
IRS SH[9]		21 01 32.89	68 09 52.5		
IRAC 8.0[6,8]	80	21 01 36.92	68 09 47.7		
Orion					
FC I2[4]	40	5 35 26.00	-5 26 12.0	1500, 50	360
FC M2[4]	9	5 35 37.00	-5 29 21.0	1400, 45[13]	792
IRS SH[10]					
I4		5 35 23.3	-5 25 20.7		
I3		5 35 24.4	-5 26 39.1		
I2		5 35 26.3	-5 26 12.1		
I1		5 35 28.1	-5 27 43.8		
M1		5 35 29.9	-5 27 14.4		
M2		5 35 31.6	-5.27 43.6		
M3		5 35 33.3	-5 28 12.9		
M4		5 35 35.0	-5 28 42.1		
V1		5 35 39.7	-5 30 2.7		
V2		5 35 42.5	-5 30 51.9		
V3		5 35 48.3	-5 32 30.3		
IRAC 8.0[11]	39	5 35 22.33	-5 24 36.0		

[1] This value corresponds to the peak SNR in each frame.; [2] α, δ (J2000) refer to the center of the map; α has units of hours, minutes, and seconds, and δ has units of degrees, arc minutes, and arc seconds; [3] Nod parameters (throw, angle); [4] FLITECAM; [5] e.g. Peeters et al. (2012, 2017); Shannon et al. (2016); [6] Spitzer Heritage Archive; [7] Fleming et al. (2010); [8] Croiset et al. (2016); [9] e.g. Berné et al. (2007); Boersma et al. (2013); Stock et al. (2016); [10] Rubin et al. (2011); Boersma et al. (2012); [11] Megeath et al. (2012); α, δ in this case reference the center of a sub image extracted from the original mosaic. [12] Exposure Time. [13] We use the nod position of FLITECAM I2

their central star. Specifically, for NGC 2023, we performed photometry on the central star, HD 37903, in each frame after background subtraction which resulted in a flux density of 0.38 ± 0.02 Jy on average. Similarly for NGC 7023, we performed photometry on the central star, HD 200775, in the FC frame and found a flux density of 11.56 ± 0.03 Jy. This is consistent with the spectra of HD 37903 and HD 200775 given in Sellgren (1984), again demonstrating that our FLITECAM data is properly calibrated.

We estimate the PAH contribution to the total flux observed in this filter from AKARI spectral observations of NGC 7023 coinciding with the NW PDR (Pilleri et al., 2015). We do this by multiplying both the continuum–subtracted 3.3 μm band and the total spectrum with the FLITECAM 3.3 μm filter response curve and subsequently integrate over the filter range for each AKARI pointing. Dividing these quantities, we found that the PAH contribution in the 3.3 μm filter ranges from 59–74% of the total emission (which comprises both PAH and dust continuum emission). As both continuum and PAH features are due to UV pumped fluorescence from large molecules (Allamandola et al., 1989) and both species require similar sizes to be excited, it is reasonable to assume that the feature to continuum ratio will remain constant within a given source. Moreover, ISO-SWS observations of NGC 2023 and NGC 7023 show that both sources have very similar feature to continuum emission ratios for the 3.3 μm band (e.g. Moutou et al., 1999, their figure 3), thus the total PAH contribution in the FLITECAM filter will be approximately the same.

Orion

The Orion FLITECAM observations (I2 and M2, Figure 2.3) were taken on separate dates and were thus calibrated independently. The chosen nod off source position for the FLITECAM M2 observation in Orion has the same level of flux in the IRAC 3.6 μm image as the faintest portion in the FLITECAM FOV. Therefore, we used the sky background of the FLITECAM I2 observation. Comparing the I2 and M2 observations in the entire overlap region, we find the data do not agree with each other: the I2 observation exhibits higher surface brightness for the diffuse emission. We therefore match the background level of the I2 to the M2 frame by subtracting the difference in the average surface brightness of both frames within the overlap region (293 ± 3 MJy sr^{-1})) from the I2 data. We compare the I2 observation to the M2 observation (after this offset correction) by performing a linear fit with a fixed y-intercept of 0 on all pixels in the overlap region (Figure 2.4). The resulting slope fit between both images shows a slope of 1 implying they agree well with each other. Both FLITECAM FOVs were regridded onto a larger area that encompassed both frames and subsequently combined into one image (shown in Figure 2.3). We note that when combining these images, flux density values from the M2 observation were taken for the overlapping pixels to avoid adding more uncertainty and minimize any discontinuities between the borders of these two FOVs.

Due to these calibration difficulties with the FLITECAM data, we further investigate the absolute calibration by comparing it with IRAC 3.6 μm data. First, we estimate the expected ratio of the FLITECAM to IRAC observations for the Orion Bar. To this end, we use the ISO-SWS
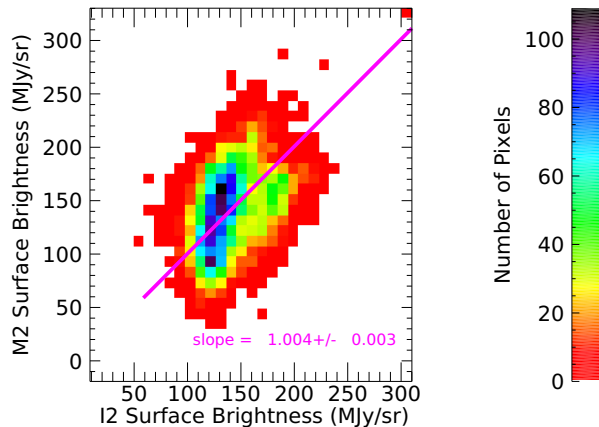
Figure 2.4: The observed surface brightness in the M2 and I2 FLITECAM observations (after offset correction) for all pixels in the overlap region (see text for details). The magenta line represents a slope fit to the data of which the fit parameters are given at the bottom of the figure. All stellar sources present have been masked.

spectra across the Orion Bar [2]. We multiply these ISO-SWS spectra with both filter response curves and find that the average FLITECAM-to-IRAC ratio equals 2.7 ± 0.2. Next, we compare the observed flux densities of the FLITECAM I2 $3.3\,\mu$m and the IRAC $3.6\,\mu$m images (after applying the IRAC $3.6\,\mu$m extended source correction) within the ISO-SWS pointings [3]. We find the average observed FLITECAM I2/IRAC $3.6\,\mu$m ratio is 4.4 ± 0.2. A FLITECAM-to-IRAC ratio of 4.4 is 1.6 times higher than our predicted ratio of 2.7 and indicates that the absolute flux calibration of the FLITECAM $3.3\,\mu$m emission is overestimated by a factor of 1.6 ± 0.1. To further validate this approach, we also apply it to the RNe. The predicted FLITECAM to IRAC ratio is determined by multiplying the AKARI spectra of NGC 7023 (Pilleri et al., 2015) with the respective filters. We find that the mean flux density of the spectrum multiplied with the $3.3\,\mu$m filter is about 2 times greater than multiplying with the IRAC $3.6\,\mu$m. A similar ratio is expected for NGC 2023 based on the similarity of the IR spectra of these sources (e.g. Moutou et al., 1999; Verstraete et al., 2001). Using the same sized apertures as the Orion pointings in both RNe, we are able to reproduce the predicted FLITECAM-to-IRAC flux ratios of 2. This shows that the FLITECAM observations of the RNe are in agreement with predicted values whereas those of Orion are not. We thus apply a scaling factor of 1/1.6, as determined above, to the FLITECAM Orion data. We find that the M2 observations is in better agreement with IRAC $3.6\,\mu$m than the I2 observations as the latter requires an additional negative offset. Hence, we will use the M2 observation as a reference and we only consider the I2 observation where the M2 observation is unavailable, i.e. for the IRS SH positions I4 and I3. The IRS SH I2 position lies on the edge of the FLITECAM M2 frame, thus we use a combination of both the FLITECAM I2 and M2 data for this position. All other IRS SH position that overlap

---

[2]There are five ISO-SWS spectra available across the Orion Bar at distances of $2.597'$, $2.175'$, $1.971'$, $1.766'$, and $1.356'$ from θ^1 Ori C referred to as positions D2, H2S1, D5, Brγ, and D8 respectively (Fig 2.3, e.g. Peeters et al., 2002; van Diedenhoven et al., 2004). Their TDT numbers are 69502005, 69501806, 83101507, 69502108, and 69501409 respectively.

[3]See Appendix A.2 for a comparison between FLITECAM and IRAC $3.6\,\mu$m for all pixels.

with our FLITECAM frames (I1, M1, M2, M3, M4, V1, and V2) are covered solely by the FLITECAM M2 data. We note that the relative intensity variations are not influenced by the large factor applied to match the FLITECAM data with the IRAC 3.6 μm data, hence relative intensities and derived relative ratios will not be affected.

We estimate the PAH contribution to the total flux observed in the FLITECAM filter from the ISO-SWS Orion Bar D2 position by multiplying the filter response curve with the Bar D2 spectrum (e.g. Peeters et al., 2002; van Diedenhoven et al., 2004). We find that the total PAH contribution to the 3.3 μm filter is about 71% of the total emission (which comprises both PAH and dust continuum emission).

2.4.2 Spitzer

We obtained the Spitzer-IRS data in reduced form (for details on the reduction process, see Peeters et al. (2012) and Shannon et al. (2015) for the RNe and Boersma et al. (2012) for the Orion data). To measure the 11.2 μm PAH emission, we defined and subtracted a local spline continuum with anchor points at 10.85 and 11.65 μm (as in Peeters et al., 2017) from the spectrum at each pixel in our spectral maps or in the case of the Orion IRS SH data, from the spectrum at each pointing. We performed a simultaneous Gaussian fitting procedure to the 11.0 and 11.2 μm emission features in each continuum–subtracted spectra in order to separate these features (e.g. Stock et al., 2014, 2016; Peeters et al., 2017). The flux of the 11.2 μm emission band is then determined by integrating these continuum–subtracted spectra over the wavelength range given above and subtracting the 11.0 μm band flux.

We obtained the Spitzer-IRAC data in reduced form for NGC 2023 and the Orion Nebula (Fleming et al., 2010; Megeath et al., 2012) and retrieved them from the Spitzer Heritage Archive in the case of NGC 7023. To approximate the 7.7 μm PAH emission, we convert the IRAC 8.0 μm images (MJy sr^{-1}) to flux densities (W m^{-2} sr^{-1}) by multiplying by the wavelength range covered by the 7.7 μm emission band of $\sim$ 1.0 μm (e.g. Peeters et al., 2002), again assuming a nominal flat spectrum. The relative PAH contribution in this filter is expected to be up to about 89% of the total emission in the diffuse ISM (Stock et al., 2014) [4]. This approximation remains valid across the FOV except near the illuminating source where the radiation field strength will be significantly stronger and the relative PAH contribution will drop. For example, Stock et al. (2014) found that in the center of an ultra-compact H ii region, the PAH contribution drops to about 55% of the emission. As these correspond to the most extreme variations that may be expected and are likely much larger than for the PDRs considered here, we are confident in our procedure.

In order to compare the spatial distribution of the different PAH bands for the RNe, the FLITECAM and IRAC 8.0 μm images were regridded to the IRS SH pixel scale (2.3″ $\times$ 2.3″). Both images were additionally averaged over 2 x 2 pixels, set by the IRS spatial resolution. Bright stellar sources in the IRS FOVs and pixels for which there was no 3 σ detection of the 11.2/3.3 PAH ratio were masked out. In case of the Orion, we determined the median flux

---

[4] We find taking a radial cut of a Spitzer IRS SL spectral cube across the S ridge PDR front in NGC 2023 and find PAH emission accounts for between 72–80% across the cut (see Appendix A.1.)

density for both FLITECAM and IRAC 8.0 μm images within the IRS SH aperture at each pointing. In this way, the PAH emission at 3.3, 7.7, and 11.2 μm are compared at 10 different pointings within the Orion region (as the V3 IRS FOV was not covered by the FLITECAM observations).

2.5   Results

We determined the 11.2/3.3 and IRAC 8.0/11.2 (as probed by IRAC 8.0 μm/11.2 μm) PAH intensity ratios spatially where images of each band were present. For NGC 2023 and NGC 7023, these ratios were measured where each of our observations overlap, this resulted in a FOV of the same size as the IRS SL maps. For Orion, we determined these ratios in the IRS SH apertures in each of the different pointings. We consider the ratio maps and cuts obtained for each source individually.

NGC 2023

Figure 2.5 shows the 11.2/3.3 and IRAC 8.0/11.2 PAH intensity ratios in the southern PDR of NGC 2023. Contours of the 12.3 μm H_2 line are overplotted in white to emphasize the S and SSE emission ridges. These bright filaments are thought to be edge-on corrugations of the cloud material that surrounds the bowl-shaped cavity (Field et al., 1994). The central star is beyond the upper right edge of this map.

We find minima in the 11.2/3.3 PAH intensity ratios at the peak of the H_2 emission and the 3.3 μm emission near the S ridge. In the SSE ridge, the minimum is slightly displaced (in the direction towards the star) compared to the H_2 peak intensity, again coinciding with the nearby peak of the 3.3 μm emission. Another minimum in the 11.2/3.3 ratio behind the H_2 peak centered at pixel (5, 11) is also apparent. In general, we find an increase in this ratio as we move towards the star and further into the molecular cloud behind both ridges. Moving inwards towards the star from the S ridge H_2 peak, there is a local minimum shown in cyan surrounded by green which extends westward from the SSE ridge towards the far right of the image and which is centered at pixel coordinates (15, 18). This ratio then proceeds to rise moving further inwards towards the top right of the frame.

Overall, the IRAC 8.0/11.2 PAH intensity ratio exhibits a stratified morphology with its highest values closest to the central star. In addition, it exhibits a narrow local peak just above the H_2 peak within the S ridge as well as in the lower right portion of the S ridge. The SSE ridge, in contrast, has a minimum in this ratio. Below the S ridge into the molecular cloud, there is a rise in this ratio.

Figure 2.6 shows a crosscut taken across the S ridge emission peak (see Figure 2.1 for the orientation of the cut) of (a) the normalized flux densities of the 3.3, IRAC 8.0, and 11.2 μm emission as well as (b) the 11.2/3.3 and IRAC 8.0/11.2 ratios. Note that the 3.3 μm and the 11.2/3.3 profile have a shorter range beyond the PDR front, due to the lack of a 3 σ detection with FLITECAM. All three emission features peak at the PDR front (as traced by the peak intensity of the H_2 emission, at 78.6″ from the illuminating source). However, the 3.3 μm emission drops fastest in intensity away from this PDR front, followed by the 11.2 μm emission. Interestingly, the IRAC 8.0 μm emission shows a plateau from ~ 50–70″, before dropping
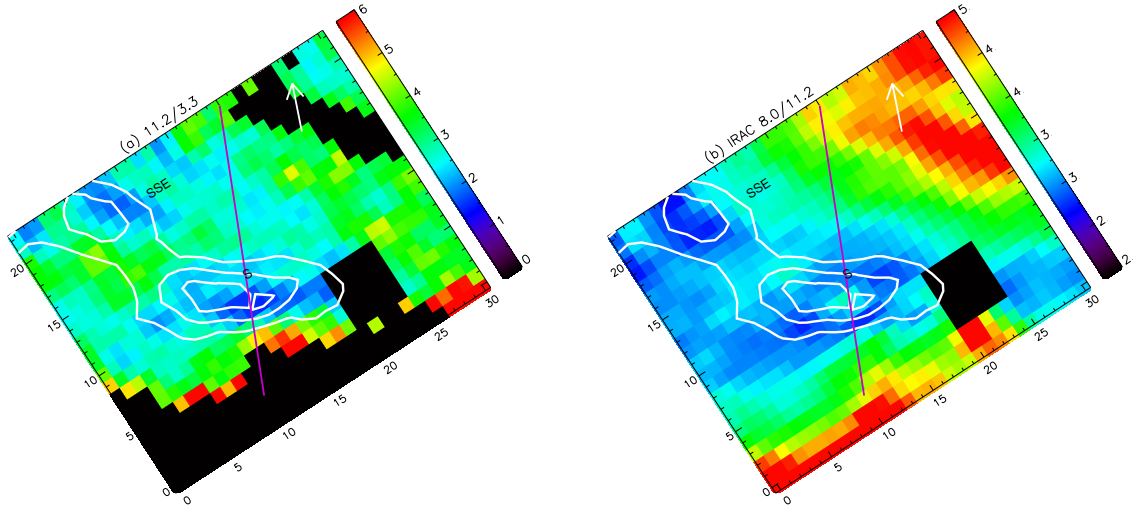
Figure 2.5: (a) The 11.2/3.3 and (b) the IRAC 8.0/11.2 PAH intensity ratios for the south FOV in NGC 2023. Contours of the 12.3 μm 0-0 S(2) H_2 line are overplotted in white ((2.5, 3.32, 4.14) $\times$ 10^{-7} W m^{-2} sr^{-1}). The direction to the illuminating source, HD 37903, is indicated by a white arrow. A magenta line is overplotted to indicate the position of the radial profile used for this source. The MIR emission peaks referred to as the the south ridge and south-southeast ridge as in Peeters et al. (2017) are given by S and SSE respectively. Pixels below a 3 σ detection or near the source YSO C are set to zero (shown here in black). North is up and east is to the left.

off as well closer to the central star. This overall radial profile is reflected in the 11.2/3.3 and IRAC 8.0/11.2 PAH intensity ratios which show, in general, a smooth decrease with increasing distance from the star until the PDR front, after which they start to increase again. We note that the 11.2/3.3 ratio decreases quickly from $\sim$ 4 $\pm$ 1 to $\sim$ 2.5 $\pm$ 0.5 going from 45 to 55″ away from the star. It then tends to be relatively constant between 55–70″ before dropping to a minimum of $\sim$ 1.8 $\pm$ 0.1 near the PDR front. In contrast, the IRAC 8.0/11.2 PAH intensity ratio displays a slower decrease moving away from the star, until it becomes relatively flat between 65–75″. At the PDR front, the IRAC 8.0/11.2 PAH ratio shows a very small peak which thus correspond to the local maximum at the PDR front as discussed above (see also Figure 2.5 (b)).

NGC 7023

Figure 2.7 shows 11.2/3.3 and IRAC 8.0/11.2 ratios in the NW PDR of NGC 7023. Note that these images have been rotated to align with the astrometry of NGC 7023 H_2 data from Lemaire et al. (1996). Contours of the 2.124 μm H_2 line are overplotted in white to probe the PDR front. The central star is positioned beyond the bottom left edge of this image. The 11.2/3.3 intensity ratio is at a minimum all along the PDR front. Moving towards the star, this ratio rises while also showing some smaller local fluctuations on top of the overall increase with respect to the PDR front. In addition, it does not trace very well the ring structure observed
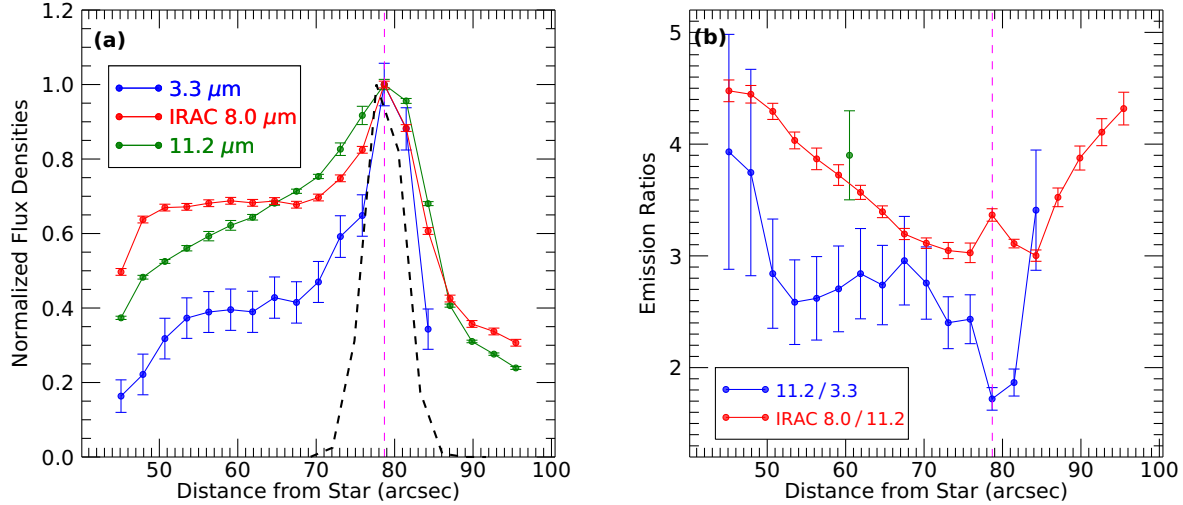
Figure 2.6: Shown are normalized radial profiles of 3.3, IRAC 8.0, and 11.2 μm intensities (a) radial profiles of the 11.2/3.3 and the IRAC 8.0/11.2 intensity ratios (b) as a function of distance to the central star in NGC 2023 (see Figure 2.1). In (a), we overplot as a black–dashed line a Gaussian fit to the PSF of YSO C within the SH cube shifted to peak at the PDR front in NGC 2023. The 11.2/3.3 intensity ratio determined from the ISO-SWS pointing is shown as a green circle in the respective ratio profiles (right panels, see text for details). The PDR front is traced by the 12.3 μm 0-0 S(2) H_2 emission line (shown in magenta). Note that increasing 11.2/3.3 corresponds to increasing PAH size and increasing IRAC 8.0/11.2 corresponds to increasing ionization. The associated uncertainties are indicated as error bars of the same color as the respective data.

in the IRAC 8.0 μm and FLITECAM 3.3 μm images. Behind the PDR front, the ratio rises although a SNR decrease limits the extent to which this can be traced reliably.

Overall, the IRAC 8.0/11.2 ratio decreases in an almost parallel layered structure with distance from the central star and does not show the ring structure as seen in the IRAC 8.0 emission. While the lowest values are found in regions sandwiching the PDR front, local maxima are apparent along the PDR front itself relative to its immediate surrounding area (around pixels (5, 20) and (13, 18)). Behind the PDR front, away from the central star, the ratio seems to rise again.

Figure 2.8 shows a crosscut across the NW PDR (see Figure 2.2 for the orientation of the cut) of (c) the normalized fluxes of the 3.3, IRAC 8.0, and 11.2 μm emission as well as (d) the 11.2/3.3 and IRAC 8.0/11.2 intensity ratios. Each of the emission features peak close to or at the PDR front (as traced by the peak intensity of the H_2 emission, at 46.3″ from the illuminating source). In NGC 7023, as was also found for NGC 2023, the 3.3 μm emission decreases more sharply away from the PDR front compared to the 8.0 and 11.2 μm emission. Moving towards the star, both the 3.3 and IRAC 8.0 μm intensities show an initial decrease followed by a plateau between ~ 30–40″ before decreasing again close to the star. This plateau in emission is likely due to the ring of emission seen south of the PDR front detected at both wavelengths (Figure 2.2). The 11.2 emission shows a linear decrease in intensity as the portion

Figure 2.7: (a) The 11.2/3.3 and the (b) IRAC 8.0/11.2 PAH intensity ratios for the northwest NGC 7023 FOV. Contours of the 2.124 μm 1-0 S(1) H$_2$ line are overplotted in white (80, 120, 175, 2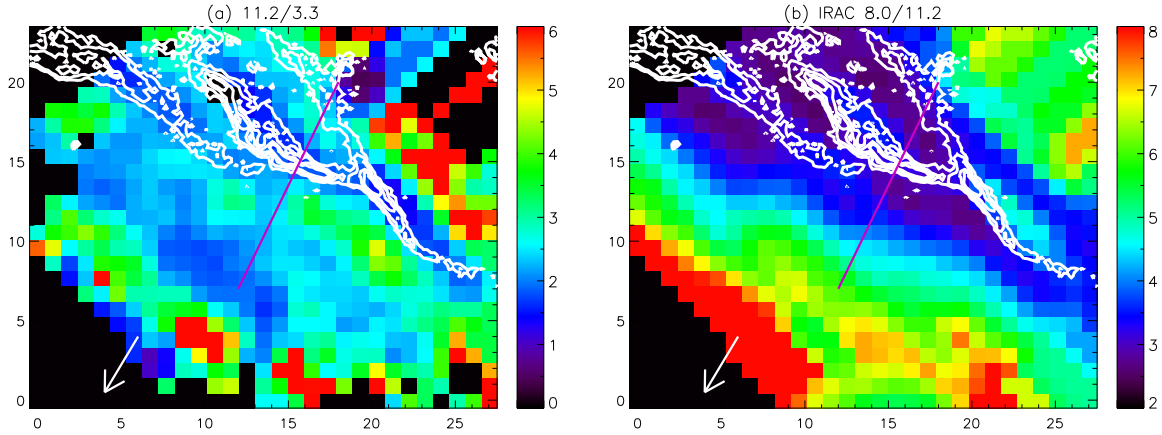20 arbitrary units, Lemaire et al., 1996). The direction to the illuminating source, HD 200775, is indicated by a white arrow. A magenta line is overplotted to indicate the position of the radial profile used for this source. Pixels below a 3 σ detection or outside of the IRS SH aperture are set to zero (shown here in black). North is up and east is to the left.

of the ring structure facing the illuminating star is much fainter in this band. The 11.2/3.3 radial profile shows a decrease away from the star up to a distance of 25″. The ratio then increases up to a maximum at ∼ 38″ due to the filaments comprising the ring structure perpendicular to the PDR front becoming increasingly luminous in the 11.2 μm. Beyond this peak, there is another decrease to a minimum located just beyond the PDR front at 50″, after which the ratio increases again. The IRAC 8.0/11.2 radial profile shows a different overall trend. It peaks closest to the illuminating star and shows a significant decrease away from the star down to a minimum that occurs at the same distance as the maximum in the 11.2/3.3 radial profile, corresponding to the emergence of the 11.2 μm emission within the ring structure. This again can be attributed to the steadily increasing prominence of the ring structure in the 11.2 μm emission relative to the other bands which show a more uniform emission distribution here. With continuing distance from the central star, the IRAC 8.0/11.2 ratio increases again until ∼ 50″ after which it drops.

We note that while the relative trends in 11.2/3.3 and IRAC 8.0/11.2 ratios are quite similar between this study and Croiset et al. (2016), the absolute values of the ratios are not in agreement. This arises due to the following differences. First, Croiset et al. (2016) used the FORCAST 11.1 μm broadband filter with a FWHM of 0.95 μm. These authors estimated that the continuum emission contributes 20% to the observed emission in the FORCAST filter and, as a consequence of this low contribution, represent the 11.2 μm PAH flux by the observed FORCAST 11.1 μm flux. In contrast, we measure the integrated 11.2 μm band strength from the IRS SH cube (Section 2.4.2). We find that this (integrated) flux accounts for 58% of the PDR front emission within the FORCAST bandwidth decreasing to 35% at 20″ from the illuminating star. At 11.2 μm, the peak position of the 11.2 PAH band, PAH emission contributes 80% of the observed emission at this wavelength at the PDR front. Due to the FORCAST filter width, this results in a lower (integrated) PAH contribution. In addition, we note that

the portion of the ring-like structure facing the illuminating source is not clearly visible in our 11.2 μm PAH map (extracted from IRS SH spectra) whereas it is clearly evident in the FOR-CAST 11.2 μm image presented in Figure 1 of Croiset et al. (2016). We attribute this to our subtraction of the dust continuum emission from the IRS SH spectra to isolate the 11.2 μm PAH emission. Summarizing, different methods of representing the 11.2 μm PAH emission strength and the subtraction (or not) of the underlying dust continuum give rise to differences in the 11.2 μm PAH strength between this work and Croiset et al. (2016). Second, the absolute surface brightness of the IRAC 8.0 μm observations used in each study differs. Specifically, the surface brightness at the NW PDR of the archival IRAC 8.0 μm observation used here is $\sim$ 3–4 times brighter than those of the IRAC 8.0 μm observations used in Croiset et al. (2016). The origin of this discrepancy is unknown and so we elected to use the archival IRAC 8.0 μm observations. As a consequence of these issues with the 11.2 and IRAC 8.0 μm measurements, our IRAC 8.0/11.2 ratios are a factor of 7 higher than those reported in Croiset et al. (2016). Despite these discrepancies, we emphasize that the relative trends found in both studies are consistent.
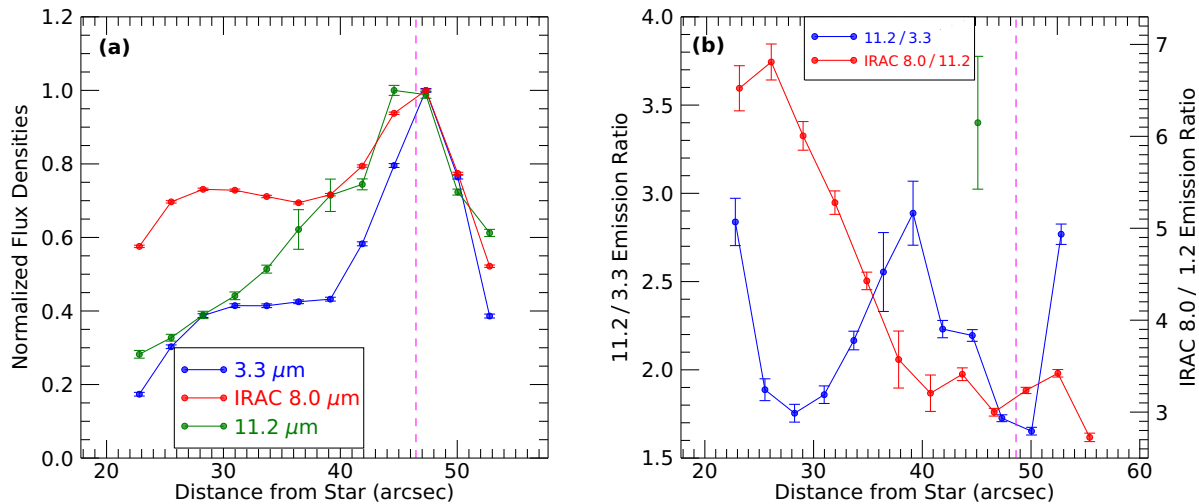
Figure 2.8: Shown are normalized radial profiles of 3.3, IRAC 8.0, and 11.2 μm intensities (a) radial profiles of the 11.2/3.3 and the IRAC 8.0/11.2 intensity ratios (b) as a function of distance to the central star in NGC 7023 (see Figure 2.2). The 11.2/3.3 intensity ratio determined from the ISO-SWS pointing is shown as a green circle in the respective ratio profiles (right panels, see text for details). The PDR front is traced by the 2.124 μm 1-0 S(1) H$_2$ emission line in NGC 7023 (shown in magenta). Note that increasing 11.2/3.3 corresponds to increasing PAH size and increasing IRAC 8.0/11.2 corresponds to increasing ionization. The associated uncertainties are indicated as error bars of the same color as the respective data.

Orion

Figure 2.9 shows (a) the normalized flux densities of the 3.3, IRAC 8.0, and 11.2 μm PAH emission as well as (b) the IRAC 8.0/11.2 and (c) the 11.2/3.3 ratios as a function of distance from the illuminating source for each IRS SH pointing. The V2 pointing is not included for the

3.3 μm profile and the 11.2/3.3 ratio due to the lack of a 3 σ detection with FLITECAM. Each of the three emission features are brightest near the Bar and decrease steeply out to the M1 pointing. Note that all three of these features vary in lockstep. Subsequently, moving outwards towards the Veil, the IRAC 8.0 and 11.2 μm exhibit a slower rate of decrease with distance reaching a minimum at the V1 pointing. Finally, both band intensities rise again at the V2 pointing. From measurements of the IRAC 8.0 and 11.2 μm emission in the V3 pointing (not shown in Figure 2.9), these flux densities continue to increase further into the Veil (see also Boersma et al., 2012). We note that the 11.2 μm band, as well the IRAC 8.0 μm band to a lesser extent, shows enhanced emission at the M2 and M3 pointings relative to the M1 and M4 pointings (or, alternatively, a relative steeper decline than expected at the M1 position) and a dip in its emission at the M1 position. Differences in the relative decline of the band intensity are better probed with their intensity ratios. At the I3 position, the 11.2/3.3 ratio reaches a maximum of 2.1 ± 0.1, which decreases out to the M1 position, where this ratio drops to a minimum of 1.0 ± 0.1 due to the larger relative decrease in the 11.2 μm band. Past this minimum, there is a slight rise in the 11.2/3.3 ratio at the M2 and M3 positions mimicking the bump found in the 11.2 μm profile. At the M4 position all the way out to the V1 position, the ratio remains constant within uncertainties at the same value as the M1 position.

In contrast, the IRAC 8.0/11.2 intensity is high at the I4 position and decreases down to a minimum at the I1 position. This is followed by an increase back to a maximum at the M1 position, again due to the 11.2 μm emission showing the sharpest relative decrease at this pointing. Beyond the M1 pointing, the ratio then decreases down to another minimum at the M3 pointing before rising again all the way out to the V2 pointing.

2.6   Discussion

Relative intensity variations of the 3.3 to 11.2 μm bands trace the average size of the observed PAH population (e.g. Schutte et al., 1993; Ricca et al., 2012). Indeed, upon absorption of a UV photon of a given energy, a smaller PAH molecule, with fewer vibrational modes in comparison to a larger molecule, will obtain a higher internal temperature as more energy is being distributed per mode. Smaller PAHs will thus emit preferentially in the 3.3 μm band compared to the 11.2 μm band. Both the 3.3 and 11.2 μm emission bands originate in neutral PAH species which eliminates any dependence on the PAH charge state. Both bands also originate in C–H modes and are therefore not sensitive to variations in the H/C ratio of the emitting species. In addition, these bands span the largest range in wavelength of the major PAH bands (excluding the 12.7 μm, which is of mixed charge state, i.e. Peeters et al., 2012, 2017; Shannon et al., 2015, 2016), maximizing the spectral sensitivity to internal temperature.

Ricca et al. (2012) employed the NASA Ames PAH IR spectroscopic database (PAHdb, Bauschlicher et al., 2010; Boersma et al., 2014b; Bauschlicher et al., 2018) to calculate the intrinsic emission spectrum of PAHs with different sizes for an average photon energy of 6 and 9 eV. These authors find i) a clear inverse-relationship between the 3.3/11.2 PAH band ratio and PAH size for PAHs of the coronene and ovalene family and ii) that a higher absorbed average photon energy will increase the 3.3/11.2 ratio for a given PAH species (their Figure 16). Hence,
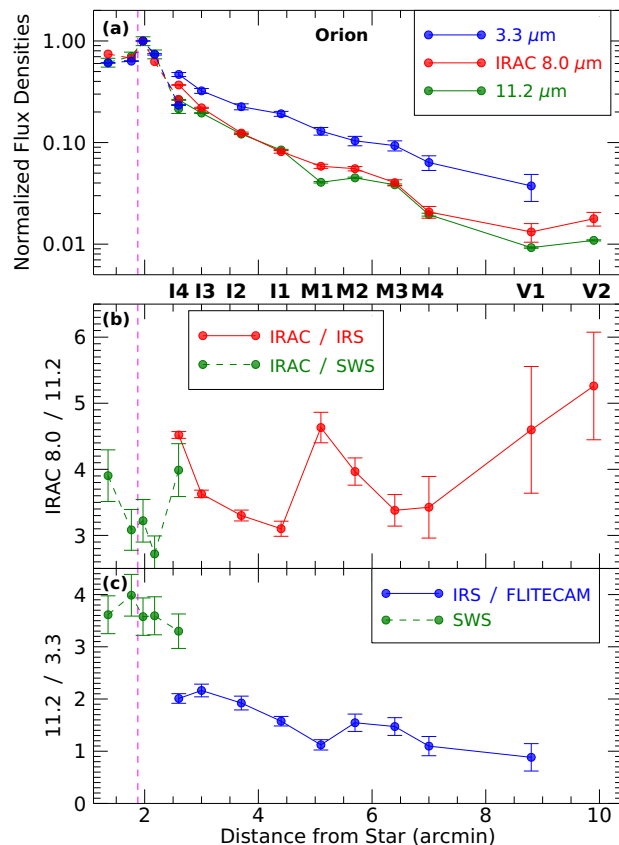
Figure 2.9: (a) Normalized radial profiles of the 3.3, IRAC 8.0, and 11.2 μm intensitiesand radial profiles of (b) the IRAC 8.0/11.2 ratio and (c) the 11.2/3.3 ratio as a function of distance to the illuminating source in the Orion Nebula (see Figure 2.3). Radial profiles including 3.3 and 11.2 μm intensities and the associated ratios derived in each of the five ISO SWS pointings across the Orion Bar are shown here using dashed lines. The projected distance from θ^1 Ori C to the ionization front of the Orion Bar (shown in magenta) is taken from [OI] 6300 Å measurements of Salgado et al. (2016). Note that increasing 11.2/3.3 corresponds to increasing PAH size and increasing IRAC 8.0/11.2 corresponds to increasing ionization. The associated uncertainties are indicated as error bars of the same color as the respective data.

comparing the observed 3.3/11.2 PAH intensity ratios with these calculations can then provide an estimate for the expected size distribution of the PAH population.

In contrast, the IRAC 8.0/11.2 ratio traces the ionization balance of the PAH population. Indeed, the IRAC 8.0 μm channel covers the 7.7 and 8.6 μm PAH emission bands which are due to ionized PAH molecules while the 11.2 μm emission band arises from neutral PAH species. Hence, this ratio yields another probe of the interaction between FUV radiation and the PAH population.

Croiset et al. (2016) investigated the size and charge distribution of the PAH population in NGC 7023. These authors followed the approach by Ricca et al. (2012) to determine the average size of the PAH population based on the 11.2/3.3 μm PAH intensity ratio using an

average absorbed photon energy of 6.5 eV (their Figure 5). They report that the average PAH size reaches a minimum of 50 carbon atoms at the PDR front and thus increases away from the PDR front towards both the molecular cloud and the illuminating star reaching sizes up to 70 carbon atoms. In addition, these authors report that the charge distribution becomes more dominated by ionized PAHs with decreasing distance from the central star, consistent with previous results (e.g. Joblin et al., 1996b; Verstraete et al., 1996; Berné et al., 2007).

Comparing the (relative) PAH intensity radial profiles for NGC 7023 and NGC 2023 (Figure 2.8 and (Figure 2.6), we report very similar trends in both RNe which are consistent with the results of Croiset et al. (2016): i) the intensity of each emission component increases with distance from the illuminating source and peaks at the PDR front before decreasing again into the molecular cloud, ii) the size of the PAH population reaches its minimum at the PDR front, and iii) the charge state of the PAH population decreases from the illuminating source towards the PDR front. As we probe a different configuration with our pointings towards the Orion Bar, its trends, as described in Section 2.5, are clearly distinct compared to those of the RNe. We now consider the specific properties of the size distribution and charge balance of the PAH population for each source individually.

2.6.1 Average PAH size distribution

We derive the average PAH sizes for our sample based on the 11.2/3.3 ratios as observed with FLITECAM and IRS. We remind the reader that some uncertainty exists related to their absolute values (cf. FLITECAM - SWS comparison, Section 2.5) and we did not apply a correction for the PAH contribution in the FLITECAM filter. Both will affect the derived average PAH sizes. Consequently, trends in the average PAH size are trustworthy while its absolute value is indicative.

NGC 7023   To determine the average PAH size in NGC 7023, we apply the emission model shown in Figure 5 of Croiset et al. (2016). The minimum in the 11.2/3.3 ratio of ∼ 1.7 ± 0.1 at the NW PDR front (Figure 2.7 (a) and Figure 2.8 (b)) corresponds to an average PAH size of ∼ 50 ± 2 carbon atoms. Closer to the illuminating star, the 11.2/3.3 ratio rises up to 2.9 ± 0.2, corresponding to PAHs with ∼ 65 ± 5 carbon atoms. This is followed by a decrease to a ratio of 1.8 ± 0.1 or PAHs with ∼ 50 ± 2 carbon atoms before rising again into the cavity surrounding the star. As detailed in Section 2.5, the trends found in the 11.2/3.3 and consequently the average PAH size for the NW region of NGC 7023 are overall similar to those reported by Croiset et al. (2016) while absolute values differ due to the different methods used to measure the 11.2 μm emission.

NGC 2023   We use the Kurucz stellar model used by Andrews et al. (2015) and the emission model of Croiset et al. (2016, which takes the absorption cross-section into account) to obtain an average photon energy of 7.3 eV. Using the dependence of the 11.2/3.3 PAH ratio on size as determined by Ricca et al. (2012, their Figure 16), we obtain an average PAH size of 75 ± 5 carbon atoms for a minimum value of the 11.2/3.3 ratio of ∼ 1.8 ± 0.1 at the S and SSE Ridges (Figures. 2.5 and 2.6 (b)). Moving towards the star, the 11.2/3.3 ratio rises up to ∼ 4 ± 1 corresponding to a size of ∼ 110 ± 20 carbon atoms.

Table 2.2: Physical conditions and average PAH size for our sample.

Source	coordinates[1] (J2000)	G_0 [2]	n_e [3] (cm^{-3})	T_{gas} (K)	γ [4] ($\times 10^2$)	Average PAH size minimum	Average PAH size maximum	Refs
NGC 7023	(21:01:33.3; +68:10:17.60)	2.6 (3)	0.64	250	20	50 ± 2	65 ± 5	1
NGC 2023	(05:41:40.39; -02:16:02.48) [5]	1.5 (4)	16	750	8			2
	(05:41:37.99; -02:16:35.26) [6]	4 (3)				75 ± 5	110 ± 20	2
Orion Bar	(05:35:19.9; -05:25:09.82) [7]	4 (4)	8	500	88	55 ± 5	80 ± 5	3, 4

[1] Position at which the physical conditions were derived; [2] G_0 is the integrated 6-13.6 eV radiation flux in units of the Habing field = 1.6×10^{-3} erg cm^{-2} s^{-1}. Order of magnitude is given in parenthesis ; [3] electron density in the PDR (cm^{-3}) estimated by $n_e \approx (C/H)n_H = 1.6 \times 10^{-4} n_H$ using the Carbon abundance of Sofia et al. (2004); [4] Ionization parameter $\gamma = (G_0/n_e)(T_{gas}/1000 \text{ K})^{0.5}$; [5] corresponds to the peak IR emission located outside our IRS FOV; [6] corresponds to the S ridge position; [7] Orion Bar position 4, which corresponds to the ISO-SWS D5 position.
References: 1. Chokshi et al. (1988); 2. Steiman-Cameron et al. (1997); 3. Tauber et al. (1994); 4. Galliano et al. (2008).

Orion   By using the emission model of Croiset et al. (2016) with a Kurucz stellar model of T_{eff} = 39000 K and log(g) = 4 for θ^1 Ori C (Kurucz, 1993), we obtain an average photon energy of 8.1 eV[5]. The 11.2/3.3 ratios in all regions probed SE of the Orion Bar vary between approximately 2.1 ± 0.1 to 1.0 ± 0.3[6]. This corresponds to an average PAH size range from 55 ± 5 to 80 ± 5 carbon atoms based on the 11.2/3.3 PAH ratio and size relationship as determined by Ricca et al. (2012).

Considering these three sources, we thus find that i) the average PAH sizes in NGC 7023 are the smallest, with its maximum average PAH size being similar to the minimum average PAH size in both NGC 2023 and SE of the Orion Bar, and ii) the range of average PAH size across the FOV is largest towards NGC 2023 (Table 2.2). Comparing these results with the physical conditions of the sources (Table 2.2), we note that for the RNe, the average PAH size increases when the intensity of the radiation field, as measured by G_0, increases.

2.6.2   PAH charge distribution

NGC 7023   As discussed in Section 2.5, the values of the IRAC 8.0/11.2 ratio are significantly higher than those derived by Croiset et al. (2016). Yet the relative ionization of the PAH population in NGC 7023 shows the same overall decreasing trend with distance from the illuminating star as well as a local peak along the PDR front as reported by Croiset et al. (2016).

Another tracer for the PAH ionization balance is the 11.0/11.2 PAH ratio (e.g. Hudgins & Allamandola, 1999; Rosenberg et al., 2011; Shannon et al., 2016; Peeters et al., 2017) as the 11.0 and 11.2 μm PAH emission is due to solo-C–H out-of-plane bending modes in respectively cationic and neutral PAHs (e.g. Hudgins & Allamandola, 1999; Hony et al., 2001; Bauschlicher et al., 2008). A crosscut of the 11.0/11.2 PAH ratio in NGC 7023 shows a clear decrease with

---

[5]We again note that O'Dell et al. (2017) have suggested that the primary ionization source beyond the Orion Bar is θ^2 Ori A, a O9.5V type star with T_{eff} = 34600 K. This corresponds to an average photon energy of 7.9 eV, which does not significantly change our size estimates.

[6]We note that these ratios and the subsequent PAH size derivations are highly influenced by the large multiplication factor used in Orion FLITECAM calibration. Hence, we emphasize the absolute values should be considered highly uncertain while the relative variations are trustworthy.

distance from the illuminating source (see Figure 2.10 (b) and (c)). This is fairly consistent with the crosscut of the IRAC 8.0/11.2 ratio in NGC 7023 shown in Figure 2.8 (b). We note however, that the rise in the IRAC 8.0/11.2 ratio seen moving into the molecular cloud (see Figure 2.8 (b)) is not evident in the 11.0/11.2 PAH ratio data. This suggest that the continuum contribution within the IRAC 8.0 μm filter increases behind the PDR and consequently the IRAC 8.0/11.2 ratio is not as strong of a tracer of relative PAH ionization in this region.

NGC 2023   Regarding the degree of ionization, we noticed the existence of a local maximum in the S ridge whereas no similar peak is seen at the SSE ridge (Figure 2.5 (b)). The Two Micron All Sky Survey (2MASS, Skrutskie et al., 2006) observations of NGC 2023 detect a stellar source embedded within the south ridge located $\sim 2.5''$ to the west of our line cut through this region (see Figure 2.1), which possibly gives rise to this increased PAH ionization balance.

There are clear difference between the IRAC 8.0/11.2 ratio and the 11.0/11.2 PAH ratio in NGC 2023 (see Figure 2.10 (a) and (c)). The 11.0/11.2 PAH ratio does not show the local maximum at the PDR front seen in the IRAC 8.0/11.2, but a local minimum just behind this point. Additionally, the 11.0/11.2 PAH ratio profile may reflect the bowl-shaped geometry of the cavity, where the relative ionization decrease is largest at the edge-on PDR front. Unlike the 11.0/11.2 ratio of NGC 7023, there is a slight rise in the 11.0/11.2 PAH ratio moving into the molecular cloud, but it is nowhere near as pronounced as the rise found in the IRAC 8.0/11.2 ratio of NGC 2023 (see Figure 2.6 (b)). The discrepancy between the IRAC 8.0/11.2 ratio and the 11.0/11.2 PAH ratio seen beyond the PDR front further reinforces the point that the increasing continuum contribution of the IRAC 8.0 μm makes the IRAC 8.0/11.2 ratio a relatively worse tracer of PAH ionization into the molecular cloud (e.g Appendix A.1).

Orion   The radial profile of the PAH ionization as traced by the IRAC 8.0/11.2 ratio does not resemble that of the 11.0/11.2 PAH ratio reported by Boersma et al. (2012, see Figure 2.11 (a)). This discrepancy may arise from, amongst others, a possible changing PAH contribution to the IRAC 8.0 μm band and/or from PAH dehydrogenation. As discussed in Section 2.3.2, the former cannot be the main driver of the observed variation in the IRAC 8.0/11.2 ratio. In contrast, PAH dehydrogenation will influence the 11.0, 11.2, and 8.6 μm band differently as the 11.0 and 11.2 μm bands are due to solo C–H groups while the 8.6 μm band probes all C–H groups in large compact PAHs. We note that the IRAC 8.0 μm band comprises both the 7.7 and 8.6 μm band with the 7.7 μm band dominating. Hence, PAH dehydrogenation may cause the IRAC 8.0/11.2 and 11.0/11.2 tracers for PAH ionization to diverge. Boersma et al. (2012) invoke PAH dehydrogenation for these observations to explain the discrepancy between the 11.0/11.2 PAH ratio and the observed change in the hardness of the radiation field as traced by the [S IV] 10.5/[S III] 18.7 line ratio reported by Rubin et al. (2011).

Additionally, Peeters et al. (2017) have shown that the 6.2 and 7.7 μm bands are spatially distinct from the 8.6 and 11.0 μm bands in NGC 2023. They found that the 11.0 and 8.6 μm bands peak much closer to the illuminating source in NGC 2023 than the 6.2 and 7.7 μm bands. Although all of these bands are attributed to ionic PAH species, the spatial diversity found suggests that the 6.2/7.7 and 8.6/11.0 bands correspond to distinct groups of PAH ions. Since the 7.7 μm band will have a significantly larger contribution within IRAC 8.0 μm than 8.6 μm, we conclude that IRAC 8.0/11.2 and 11.0/11.2 cannot both be used as identical tracers
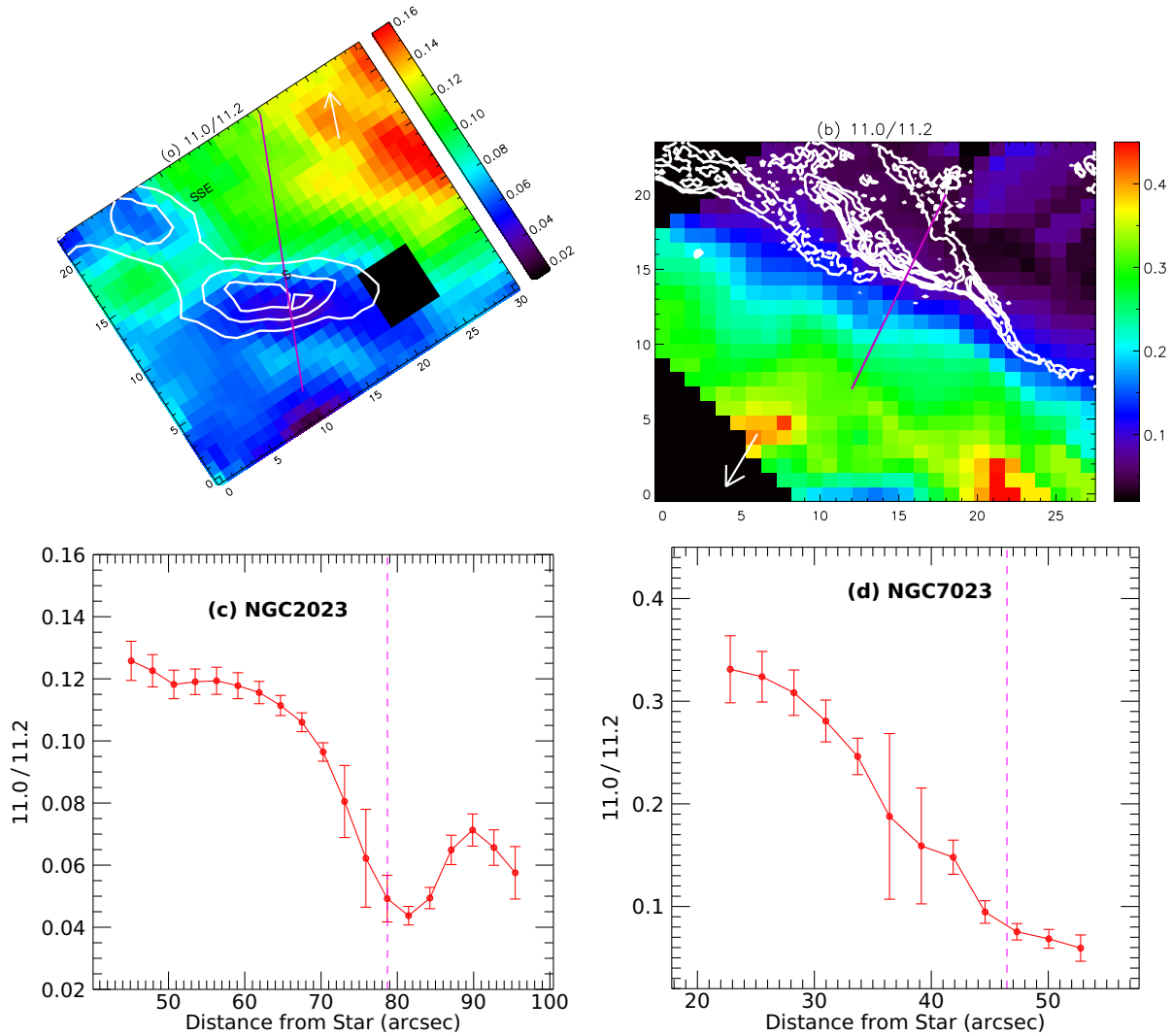
Figure 2.10: (a) The 11.0/11.2 PAH intensity ratios for the south FOV in NGC 2023 and (b) the 11.0/11.2 PAH intensity ratios for the northwest NGC 7023 FOV. See Figures. 2.5 and 2.7 for details on the contours and directions shown for NGC 2023 and NGC 7023 respectively. The direction to the illuminating source in both RNe is indicated by white arrows. A magenta line is overplotted to indicate the position of the radial profile used for these sources. Pixels below a 3 σ detection or outside of the IRS SH aperture are set to zero (shown here in black). North is up and east is to the left. Radial profiles of the PAH ionization balance as traced by the 11.0/11.2 PAH ratio (red) as a function of distance to the central star in NGC 2023 (c, see Figure 2.1) and NGC 7023 (d, see Figure 2.2). The PDR front is traced by the 12.3 μm 0–0 S(2) H_2 emission line in NGC 2023 and the 2.124 μm 1–0 S(1) H_2 emission line in NGC 7023 (shown in magenta). The associated uncertainties are indicated as error bars.
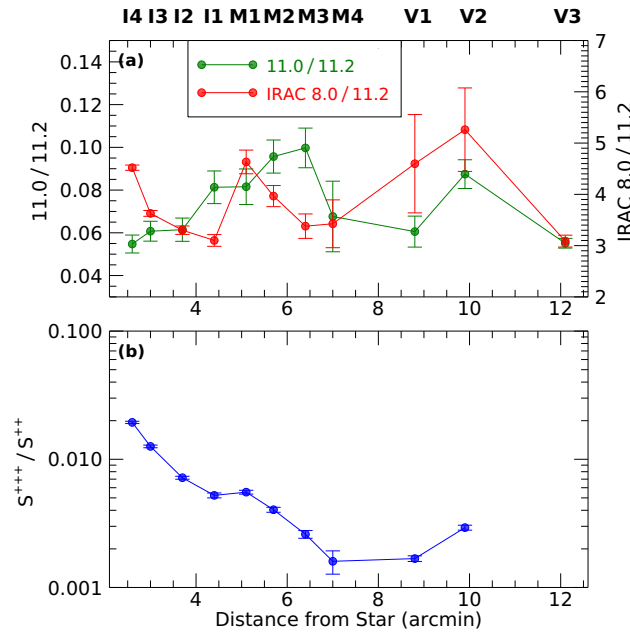
Figure 2.11: The Orion Nebula radial profiles of (a) the PAH ionization balance as traced by the IRAC 8.0/11.2 ratio (red, this work) and the 11.0/11.2 PAH ratio (green, Boersma et al., 2012), and of (b) the hardness of the radiation field as traced by the S^{+++}/S^{++} ratio (blue, Rubin et al., 2011) as a function of distance to the illuminating source. The associated uncertainties are indicated as error bars of the same color as the respective data.

of relative PAH ionization.

2.6.3   Photochemical evolution of PAHs

The observed variation of the average PAH size gives further evidence of significant ongoing photoprocessing of these molecules. Indeed, for both RNe, NGC 7023 and NGC 2023, we find that the average PAH size distribution in each source and variations in average size between the two RNe is strongly dependent on the radiation field strength, G_0. Specifically, we find that the minimum average PAH size is found at the PDR front and that the average PAH size increases upon closer approach to the illuminating stars as G_0 increases. Likewise, smaller average PAH sizes are found towards NGC 7023 (compared to NGC 2023) which has also the lowest radiation field intensity (Table 2.2). Enhanced intensity of the radiation field thus leads to increased PAH photo-processing resulting in the destruction of smaller PAH species as predicted by Allain et al. (1996). This, in turn, gives rise to a larger average PAH size. Together with the enhanced emission of fullerenes near the illuminating source (Sellgren et al., 2010; Peeters et al., 2012; Berné & Tielens, 2012), these results give support to the hypothesis of the formation of fullerenes from PAH molecules. Specifically, extreme levels of UV radiation promote the complete dehydrogenation of PAHs (> 60 carbon atoms) that subsequently fold into loose cage structures upon losing C_2 atoms until they reach stability as C_{60} molecules

(Berné & Tielens, 2012; Zhen et al., 2014; Berné et al., 2015). The interpretation of the average PAH size distribution southeast of the Orion Bar is more complicated than that of the RNe. We find an overall decreasing trend in the average PAH size (within the associated uncertainties) with distance from the illuminating source. While the G_0 value given in Table 2.2 is for the PDR front in the Bar, we expect G_0 to decrease with distance from the illuminating source (Pabst et al. 2021). Similar to the RNe, we thus find that the average PAH size decreases with G_0. However, due to lack of concrete G_0 values further into the Veil, we cannot make a direct comparison with the average PAH size in the two RNe. Boersma et al. (2012) report i) a notable decrease in the C_{60} emission from the Bar to the first Veil position at a distance of $9.90'$ (their Figure 6), and ii) fullerene-to-PAH ratio larger than 1 up to M1 and the V1-V2 positions and smaller than 1 from M1-M4 and at the V3 position. The latter has been interpreted as due to photo-processing of PAHs (Berné & Tielens, 2012; Boersma et al., 2012), this is reflected in the determined larger average PAH sizes closer to the Bar. The geometrical nature of the region delineated by the Orion Bar and the southeastern Veil is much more complex than the edge-on morphology of the PDRs found in the RNe. The Bar is an edge-on, compressed shell at the edge of a bowl created by the Trapezium cluster (Salgado et al., 2016). In our positions out to the Veil, we see a face-on PDR at the surface of the molecular cloud (Pabst et al., 2019). In the case of an edge-on PDR, the gas is transported into the cavity by the PDR evaporation flow and hence the material closer to the star is the "same" material as farther away except that it is more thoroughly processed by UV photons. In contrast, in the Veil, we are looking face-on and hence we are integrating over the history of this processing. Considering the complex morphology of this region along with the relative high uncertainties on the PAH size tracer (3.3/11.2), it is difficult to characterize the photochemical evolution of PAHs with the same level of confidence as in the simpler RNe geometries.

2.7   Conclusions

We present spatial maps of the 3.3 and 11.2 μm PAH intensities, the IRAC 8.0 μm emission, and the 11.2/3.3 and IRAC 8.0/11.2 emission ratios in three prominent MIR-bright sources – the reflection nebulae NGC 2023 and NGC 7023, and the region southeast of the Orion Bar – based upon observations from FLITECAM onboard SOFIA as well as archival Spitzer data. These emission ratio maps provide a measure of the average PAH size distribution and the relative PAH ionization respectively.

Both RNe exhibit similar trends in these intensity ratios: i) the average PAH size increases upon approaching the illuminating source while it is at a minimum along the PDR front and ii) the relative PAH ionization increases with proximity to the illuminating source. iii) In contrast to the 11.0/11.2 PAH ratio, the IRAC 8.0/11.2 ratio is not a suitable tracer of the relative PAH ionization into the molecular cloud region because of an increasing continuum contribution to the IRAC 8.0 μm band. The region southeast of the Orion Bar exhibits a decrease in the average PAH size from the Bar out to $\sim 5'$ from the illuminating source with a slight bump peaking at $\sim 6'$ before continuing to decrease in the Veil. Southeast of the Orion Bar, there is also a peculiar radial profile in the relative PAH ionization: a decrease away from the illuminating source up to $4.5'$, followed by a local maximum at $\sim 5'$ and a second maximum at $\sim 10'$. This radial profile does not resemble that of the 11.0/11.2 PAH ratio.

We derive an average PAH size of 75 carbon atoms at the PDR front up to 110 carbon atoms nearest to the illuminating source for NGC 2023; 50 carbon atoms at the PDR front, which increases up to 65 carbon atoms near the cavity region surrounding HD 200775 for NGC 7023; and a range of 55 to 80 carbon atoms for the southeast Orion region. For all sources, larger average PAH sizes correlate with an increase in G_0. In addition, the average PAH size in NGC 7023 is lower at all points in comparison to NGC 2023, whereas NGC 2023 has the widest range of average PAH sizes in the FOV considered. These results support the interpretation of the rise in the UV field intensity with proximity to the illuminating source driving the photochemical evolution of the PAH population that destroys all but the largest species and promote the formation of more stable fullerene molecules. Future studies of these astronomical sources using space-borne telescopes with higher spatial resolution instruments and lower uncertainties such as the James Webb Space Telescope will allow these trends of PAH size and relative ionization to be refined in much more detail.

Acknowledgements

Chapter 3

PAH Emission Across the Orion Bar

C. Knight[1], E. Peeters[1,2,3], W. D. Vacca[4]

[1]*Department of Physics and Astronomy, University of Western Ontario, London, ON N6A 3K7, Canada; cknigh24@uwo.ca*

[2] *Institute for Earth and Space Exploration, University of Western Ontario, London, ON, N6A 3K7, Canada*

[3]*Carl Sagan Center, SETI Institute, 189 N. Bernardo Avenue, Suite 100, Mountain View, CA 94043, USA*

[4] *SOFIA-USRA, NASA Ames Research Center, MS N232-12, Moffett Field, CA 94035-1000, USA*

3.1 Introduction

Mid-infrared (MIR) observations throughout the interstellar medium (ISM) of our Galaxy as well as external galaxies show strong emission features at 3.3, 6.2, 7.7, 8.6, 11.2, and 12.7 μm attributed to the infrared fluorescence of polycyclic aromatic hydrocarbons (PAHs). These molecules absorb far-ultraviolet (FUV) photons causing electronic excitation (i.e. Allamandola et al., 1989), which is rapidly converted into vibrational excitation that is radiated away as MIR emission as these PAH species cool. Since their discovery by Gillett et al. (1973), these bands have been observed in a wide variety of sources including H ɪɪ regions, young stellar objects, post-AGB stars, planetary nebulae, reflection nebulae, galaxies as well as the diffuse ISM (e.g. Hony et al., 2001; Verstraete et al., 2001; Peeters et al., 2002; Berné et al., 2007; Boersma et al., 2012; Shannon et al., 2016; Stock et al., 2016). PAHs and related species account for up to 15% of the cosmic carbon inventory (Allamandola et al., 1989) and play a key role in the physical and chemical processes in these environments. For instance, PAHs have been shown to be useful tracers of star formation rates (e.g. Peeters et al., 2004b; Calzetti et al., 2007; Maragkoudakis et al., 2018), they are the dominant heating source in the neutral ISM via photoelectric ejection (Bakes & Tielens, 1994), and are essential to the ionization balance through photoionization and recombination processes (Lepp & Dalgarno, 1988). Thus, studying these PAH emission features can yield a wealth of knowledge towards our understanding of the important role these molecules have in the physical and chemical processes that occur within the ISM.

The PAH emission features show variations in relative intensities, peak position, and band shape in different Galactic and extragalactic environments as well as within extended sources (e.g. Hony et al., 2001; Peeters et al., 2002; Galliano et al., 2008). The main driver for vari-

ations in PAH band intensities is the charge state of the underlying population. The 6.2, 7.7, and 8.6 μm bands are strong in ionic PAHs, whereas the 3.3 and 11.2 μm bands are more prevalent within neutral PAHs (e.g. Allamandola et al., 1989; Hudgins et al., 1994; Bakes & Tielens, 1994; Allamandola et al., 1999). Generally, PAH bands attributed to the same relative ionization state tend to be well correlated. For instance, there is a tight relationship between the 6.2 and 7.7 μm bands found in a wide variety of MIR bright sources (e.g Galliano et al., 2008; Boersma et al., 2014a; Stock & Peeters, 2017; Peeters et al., 2017; Maragkoudakis et al., 2018). However, the above relationship does not hold for all astronomical sources. Indeed, it has been found to break down on small spatial scales within the giant star-forming region N66 in the Large Magellanic Cloud (Whelan et al., 2013) and towards the center of ultra-compact H II regions within the Galactic massive star-forming region W49A (Stock et al., 2014). An investigation of PAH emission features in a much closer H II region with similar radiation field properties could provide an explanation for this anomaly by availing of the much higher spatial resolution as set by the observing instrument by virtue of proximity.

To this end, we consider the prototypical nearby star-forming region, the Orion Nebula (M42), located at a mere distance of 414 ± 7 pc (Menten et al., 2007). Within this nebula lies the Orion Bar, which has long been known to be a source of strong MIR emission (e.g. Aitken et al., 1979; Sellgren, 1981; Tielens & Hollenbach, 1985a; Bregman et al., 1989; Geballe et al., 1989; Sellgren et al., 1990; Tielens et al., 1993; Giard et al., 1994; Cesarsky et al., 2000; Rubin et al., 2011; Boersma et al., 2012; Haraguchi et al., 2012; Salgado et al., 2016; Pabst et al., 2019). Due to the edge-on, stratified nature of this photo-dissociation region (PDR), it is considered to be the benchmark for modelling these environments (e.g. Tielens & Hollenbach, 1985a; Tielens et al., 1993). Furthermore, the edge-on morphology is a key facilitator in our understanding of PDRs in that it allows us to clearly delineate the boundaries between the ionized cavity surrounding a stellar source of strong UV radiation, the neutral PDR where freely flying PAH species can prosper, and the cold molecular cloud that tends to encompass these PDRs (e.g. Tauber et al., 1994; Tielens et al., 1993; Walmsley et al., 2000; van der Werf et al., 2013; Cuadrado et al., 2015; Goicoechea et al., 2015).

In this study, we examine PAH emission features along with prominent MIR atomic and molecular emission lines towards the Orion Bar using spectroscopic observations from the Spitzer Space Telescope, along with supplementary data previously obtained from FLITE-CAM on–board the Stratospheric Observatory for Infrared Astronomy (SOFIA). In Section 3.2, we give an overview of the general morphology and physical properties of the Orion Bar. In Section 3.3, we present our spectroscopic observations as well as the data reduction methodology and we describe how the continuum and feature fluxes were measured in Section 3.4. In Section 3.5, we describe our primary results in the form of line projections of individual emission components and corresponding emission ratios with respect to distance from the primary illuminating source and correlations between these features. We discuss these results with respect to the environmental conditions and the properties of the PAH population in Section 3.6. Finally, a summary of this work is provided in Section 3.7.

3.2   Orion Bar

In the Orion Nebula, the primary illuminating source of the PDR is the brightest member of the Trapezium cluster, θ^1 Ori C, an O6V type star with T_{eff} = 38,950 K (e.g. O'Dell et al., 2017). In Figure 3.1, we show a zoomed-in mosaic of the Orion Nebula using MIR imaging. This image demonstrates that the MIR bright gas and dust forms the PDR boundary between the large ionized cavity centered on the Trapezium cluster and the surrounding molecular cloud. The Orion Bar is part of this PDR boundary and is an edge-on, compressed shell (Salgado et al., 2016). The outer boundary of the Orion Nebula is referred to as the Orion Veil, a large expanding shell of neutral gas driven by stellar winds expanding radially from the Trapezium Cluster (Pabst et al., 2019). The stratified edge-on morphology of the Orion Bar and its proximity makes it an ideal probe of a PDR environment as we can investigate the photo-processing of the gas and dust with distance to the illuminating source (e.g. Cesarsky et al., 2000; Goicoechea et al., 2015, Chapter 2). In contrast, in a face-on morphology, as found in the background PDR behind the ionized cavity surrounding the Trapezium cluster bounded by the Bar and behind the Bar out to the Veil, the entire processing history is mixed along the line of sight. Hence, this morphology makes it significantly more difficult to infer how the gas and dust chemistry is driven by the stellar radiation field. PDR models computed at the position of the Orion Bar have derived a gas density of 5×10^4 cm^{-3} and FUV radiation field strength, G_0[1], of 4×10^4 times that of the average interstellar value (e.g. Tauber et al., 1994). As we consider observations that are, in part, positioned behind the Bar, it is worth noting that it has been suggested that θ^2 Ori A, a O9.6V type star with an effective temperature of 34600 K, is the primary source of UV radiation on the far side of the Bar (O'Dell et al., 2017).

3.3   Observations and Data Reduction

3.3.1   Observations

Spitzer

Spectroscopic observations were obtained with the short-low (SL) staring mode of the Infrared Spectrograph (IRS, Houck et al., 2004) on–board the Spitzer Space Telescope (Werner et al., 2004b). This data set consists of three pointings with slits that transverse the Orion Bar at different locations (PID: 45, PI: Thomas Roellig, Figure 3.1). We assign the following nomenclature for these three pointings based on how much (part of) the aperture is in front of the Orion Bar towards the illuminating source, θ^1 Ori C. From closest to farthest from θ^1 Ori C, these pointings are referred to as: 'Orion Bar ionized' (OBI), 'Orion Bar' (OB), and 'Orion Bar neutral' (OBN). A summary of our observations is given in Table 3.1.

The SL mode has an effective wavelength range of 5.2 – 14.5 μm and a spectral resolution of 60 to 128 over three orders of diffraction: SL1, SL2, and SL3. The pixel size of the SL mode is 1.8″, with a slit width of 3.6″ and a slit length of 57″.

---

[1]in units of the Habing field (1.3×10^{-4} erg cm^{-2} s^{-1} sr^{-1}, Habing, 1968)

Table 3.1: Log of observations.

	Orion Bar	Orion Bar Neutral	Orion Bar Ionized
map α^1	5:35:27.5	5:35,27.7	5:35:25.7
map δ^1	-5:30:48	-5:31:14	-5:30:39
AORs[2]	4117760	4118016	4118272

[1] α, δ (J2000) are the central coordinates of each map. α has units of hours, minutes, and seconds and δ has units of degrees, arc minutes, and arc seconds; [2] AOR is Astronomical Observation Request Identifier.
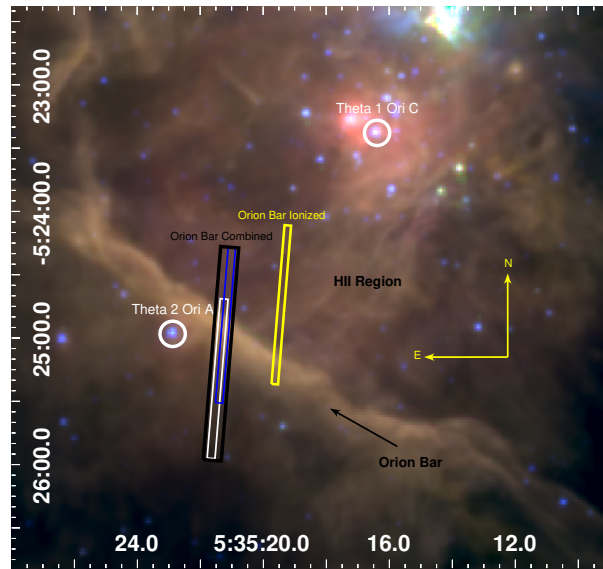
Figure 3.1: Mosaic of the Orion Nebula with IRAC 3.6 μm in blue, IRAC 5.8 μm in green, and IRAC 8.0 μm in red (Megeath et al., 2012). IRS SL apertures are referred to as 'Orion Bar' (OB), 'Orion Bar Neutral' (OBN), and 'Orion Bar ionized' (OBI) in blue, white and yellow respectively. We combine OB and OBN into a single aperture 'Orion Bar Combined' (OBC), shown in black, as detailed in section 3.3.2. The position of θ^1 Ori C and θ^2 Ori A are indicated by white circles. We note that the IRAC 3.6 μm, IRAC 5.8 μm, and IRAC 8.0 μm images use a square root scale.

SOFIA

We obtained SOFIA-FLITECAM observations in the 4th to 6th cycles towards the SE of the Orion Bar (Chapter 2). We regrid the FLITECAM 3.3 μm image to each of the three IRS SL apertures to compare these observations on an equivalent spatial resolution. Additionally, a 2×2 binning of the FLITECAM data is performed to be consistent with our analysis of the IRS SL data. While we acknowledge that the 3.3 μm emission feature accounts for $\sim 70\%$ of the flux in the FLITECAM 3.3 μm filter for ISO-SWS[2] observations near the Orion Bar as described in Chapter 2, no correction factor is applied to account for this. We convert the 3.3 μm observations from units of surface brightness (W m^{-2} μm^{-1} sr^{-1}) to flux density (W m^{-2} sr^{-1}) following the method employed in Chapter 2. Specifically, we multiply by the bandwidth of the 3.3 μm filter of ~ 0.1 μm, which assumes emission within the filter can be approximated by a nominal flat spectrum.

3.3.2 Data Reduction

The IRS SL raw data were processed by the *Spitzer* Science Center with the S18.18 pipeline version. The resulting bcd products are further processed with *cubism* (Smith et al., 2007a). Specifically, we set *cubism*'s *wavsamp* to $0.04 - 0.96$ and applied *cubism*'s automatic bad pixel generation with $\sigma_{TRIM} = 7$ and Minbad-fraction = 0.50 and 0.75 for global and record bad pixels respectively. Remaining bad pixels were subsequently removed manually.

Spectra are extracted in an aperture of 2×2 pixels moving along the slit in one-pixel steps. As a consequence, adjacent pixels are not independent. We found small mismatches in absolute flux levels between the SL1 and SL2 of 2–16% and <5% between SL1 and SL3. To remedy this, the SL3 data were scaled to the SL1 data followed by a scaling of the SL2 data to the combined SL1 and scaled SL3 data. Subsequently, the SL1 and SL2 orders were combined into a single spectral cube for each pointing.

Due to the considerable spatial overlap of the OB and OBN apertures (see Figure 3.1), we combine both slits into one extended aperture. We take pixels corresponding to the OB slit where the pointings overlap as it has a higher SNR in overlapping pixels. We refer to this combined aperture as 'Orion Bar Combined' (OBC) for the remainder of the text.

3.3.3 Spectra

Typical spectra observed towards the Orion Bar are displayed in Figure 3.2. Comparison of these spectra demonstrates how the slope of continuum rises with increasing proximity to the illuminating source. Emission features discernible above the dust continuum include the major PAH bands at 6.2, 7.7, 8.6, 11.2, and 12.7 μm as well as weaker PAH bands at 5.7, 6.0, 11.0, 12.0, and 13.5 μm. These PAH bands are usually on top of broad emission plateaus at 5–10 and 10–15 μm (separate from the dust continuum, detailed in Section 3.4.1). Additionally, other atomic and molecular lines were detected such as the 6.98 μm [Ar II] line, the 7.46 μm Pfund α line, the 8.99 μm [Ar III] line, the 9.7 μm S(3) H$_2$ line, the 10.5 μm [S IV] line, the 12.37 μm

Figure 3.2: Typical SL spectra from the PDR (left) and the H ɪɪ region (right) are shown. The orange line traces the local spline continuum (LS), the magenta line traces the global spline continuum (GS), and the green line traces the underlying dust continuum (PL).

H ɪ recombination line, and the 12.8 μm [Ne ɪɪ] line. In the ionized gas, the underlying dust continuum is much steeper and displays broad silicate emission at 10 μm (Cesarsky et al., 2000).

3.4 Data Analysis

3.4.1 Continuum Fitting

In order to separate the PAH emission features from the underlying continuum, we make use of the spline decomposition method (e.g Van Kerckhoven et al., 2000; Hony et al., 2001; Peeters et al., 2002; van Diedenhoven et al., 2004; Boersma et al., 2012; Stock et al., 2014, 2016; Shannon et al., 2015, 2016; Peeters et al., 2017) to define a local spline (LS), a global spline (GS), and the underlying dust (PL) continuum (Figure 3.2). For the LS continuum, we use anchor points at 5.37, 5.52, 5.83, 6.54, 7.07, 8.25, 9.15, 9.40, 9.89, 10.33, 10.76, and 11.82 μm. In order to better fit the continuum underneath the 12.7 μm complex, we extend our spline fits as two straight lines from 11.82 to 12.1 μm and 12.1 to 13.2 μm respectively. We do not fit the spectra beyond 13.2 μm due to the abrupt change in slope at the end of the spectra. The GS continuum fitting uses the same anchor points as the LS, except for the removal of the 8.25 μm anchor point. The difference between these two continua (LS and GS) is referred to as the 8 μm bump (e.g Peeters et al., 2017). The dust continuum consist of a straight line between anchor points at 5.5 μm and 10.1 μm as well as a straight line between 10.4 μm and 13.2 μm.

We find two very different shapes in the underlying dust continuum which is related to the position with respect to the illuminating source (Figure 3.2). Spectra obtained at positions closest to the star have a much steeper rise in continuum emission towards longer wavelengths (Figure 3.2, right panel). All other spectra that are located behind the ionization front (IF) into the PDR have a much shallower rise in continuum emission (e.g. Sellgren et al., 2010; Pilleri et al., 2012; Stock et al., 2016; Peeters et al., 2017; Andrews et al., 2018). In the case of the

spectra in front of the IF, we do not detect significant plateau continua emission and the steep slope of the underlying dust continuum does not allow a fit to a straight dust continuum from 5.5 to 10.1 μm, hence the GS fit is used to characterise this continuum similar to what was found for H II region spectra by Stock & Peeters (2017).

3.4.2   Flux Measurement

The fluxes of the major PAH bands are determined through integrating the LS continuum–subtracted spectra over the wavelength range of the feature. However, in the case of the 6.2, 11.2, and 12.7 μm features, another method is needed due to blending with weaker PAH features or atomic emission lines. Similar to Peeters et al. (2017), a two Gaussian fit of the 6.0 and (blue wing of the) 6.2 μm PAH bands was done with peak positions/FWHM of 6.02/0.12 μm and 6.232/0.156 μm respectively. We determine these values by allowing them to vary during the initial fitting procedure and subsequently take the average values over all the spectra. The 6.2 μm band flux is determined by subtracting the 6.0 μm Gaussian from the integrated flux of the LS subtracted spectra taken over the wavelength range spanning the 6.0 μm and 6.2 μm bands. We use a similar decomposition method to obtain the 11.2 μm emission feature flux. The 2 Gaussian fit of the 11.0 and (blue wing of the) 11.2 μm PAH bands has peak positions/FWHM of 11.003/0.15 μm and 11.262/0.227 μm respectively.

The 12.7 μm PAH band is significantly blended with the 12.8 μm [Ne II] line in all observations and, in some cases, with a weak 12.37 μm H I recombination line. To differentiate between these emission features, the decomposition method used in Stock et al. (2014), Shannon et al. (2015), and Stock et al. (2016) is employed. We use the NGC 2023 12.7 μm profile in the Southern Ridge PDR front detailed in Peeters et al. (2017) as template for 12.7 μm band. We perform a fitting procedure to the continuum–subtracted spectra in which we fit simultaneously two Gaussian functions to the 12.37 μm H I recombination line and the 12.8 μm [Ne II] line, and a 12.7 μm template profile which is scaled to align it with the spectra in the 12.4 to 12.7 μm range. The 12.7 μm band flux is obtained by integrating the continuum–subtracted spectra from 12.15 to 13.2 μm and subtracting the 12.37 μm H I line and the 12.8 μm [Ne II] fluxes determined from the Gaussian fits. We find an average peak position/FWHM of 12.829/0.13 μm for the Gaussian fitted to the 12.8 μm [Ne II] line for all of our spectra. We also note that it is only in spectra closest to the illuminating source where the 12.37 μm H I line flux was detected at the 3 σ level or higher. Thus for most spectra, the 12.37 μm H I recombination line does not influence the measurement of the 12.7 μm PAH strength.

A Gaussian decomposition was performed to extract individual components within the 7 to 9 μm spectral range, similar to Peeters et al. (2017); Stock & Peeters (2017). Taking the GS continuum–subtracted spectra, 6 Gaussians were simultaneously fitted to the prominent features within this range: 4 PAH Gaussian components at 7.6, 7.8, 8.2, and 8.6 μm, the 8.99 μm [Ar III] line, as well as the 7.46 μm Pfund α line (see Appendix B.2 for details). Figure 3.3 shows examples of this decomposition. The fit is unable to match the sharpness of the 7.6 μm peak due to the chosen FWHM (and they thus overshoot around ~7.8 μm).

Aside from the [Ne II] 12.8 μm line, lines that are isolated upon LS continuum subtraction are fit using a Gaussian profile. These include the 6.98 μm [Ar II] line, the 9.7 μm H$_2$ line, and the 10.5 μm [S IV] line. However, the 7.7 and 8.6 μm PAH emission features show significant blending with the 7.46 μm Pfund α line and the 8.99 μm [Ar III] line respectively in the majority
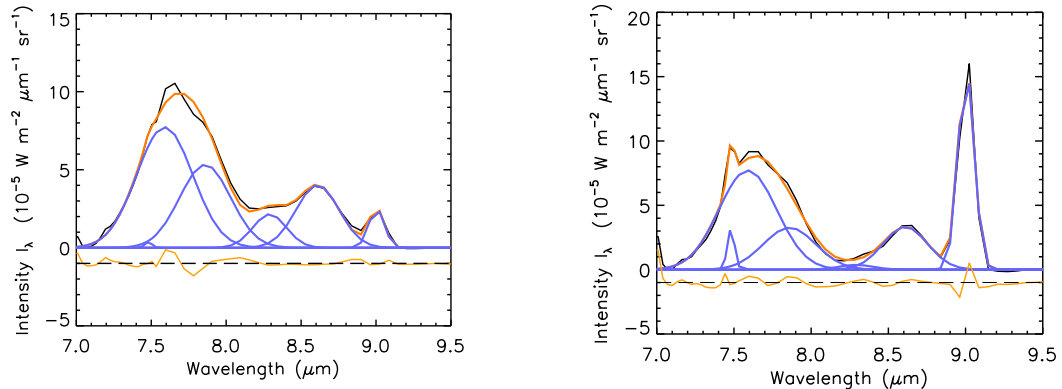
Figure 3.3: The 7 to 9 μm decomposition at positions behind (*Left*) and in front (*Right*) of the Orion Bar with respect to the illuminating source. The GS continuum–subtracted spectra are displayed in black, individual Gaussian components are shown in blue, and the combined fit in orange. The residuals (shown in yellow) and black dashed lines are offset by 1×10^{-5} for clarity.

of our spectra and are incorporated in the 6 Gaussian decomposition of the 7–9 μm region.

The signal-to-noise ratio of the PAH emission features is estimated as SNR = $F/(2 \times \text{rms} \times \sqrt{N} \times \Delta\lambda)$ where F is the feature's flux (in W m^{-2} sr^{-1}), rms the rms noise, N the number of wavelength elements within the feature, and $\Delta\lambda$ is the size of each wavelength element in the spectrum. The rms noise is determined from featureless portions of the spectra between 5.36–5.52, 9.2–9.4, and 9.95–10.3 μm. For atomic and H$_2$ lines, the signal-to-noise is the ratio of the peak line flux to the underlying rms noise.

3.5   Results

In this section we investigate the relationships between individual PAH emission bands, atomic spectral lines, H$_2$ emission line, the underlying plateaus and the dust continuum emission within our pointings across the Orion Bar. We use two separate methods to analyse these spectral features, namely linear projections and correlation plots. Our linear projections (or radial cuts) allow us to measure how these spectral features as well as their ratios vary i) with distance to the illuminating source, and ii) relative to the changing environmental conditions across the Orion Bar.

3.5.1   Line Projections

Figures. 3.4 and 3.5 show line profiles of the intensity of emission features and their ratios for the Orion Bar Combined and Orion Bar Ionized apertures[3]. We normalize these line profiles to their maximum value within each respective aperture. Only fluxes and emission ratios equal or

---

[3]We give a summary of all of the emission components for which we have derived line profiles in Appendix B.1.
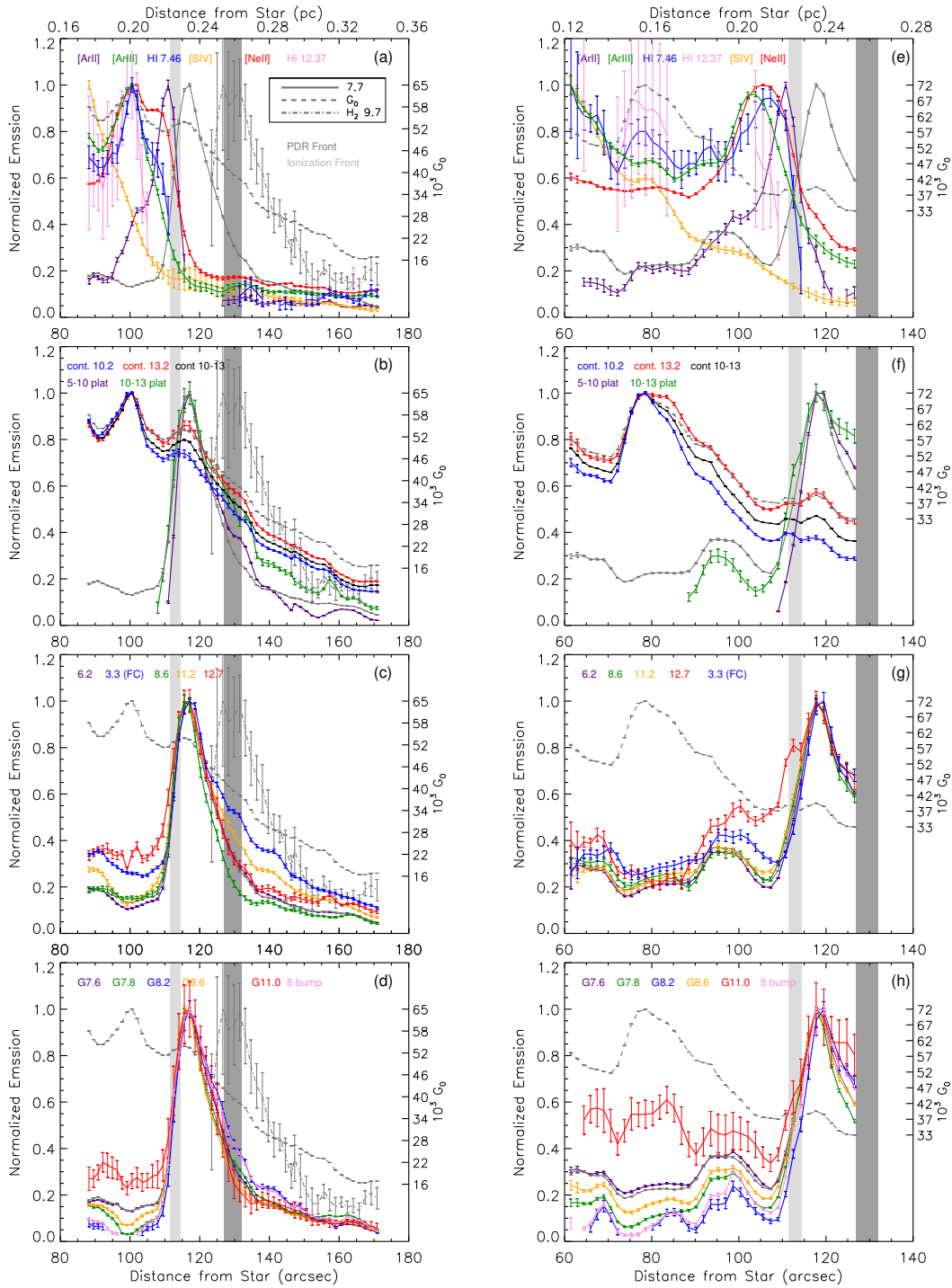
Figure 3.4: Orion Bar combined (left) and Orion Bar ionized (right) line profiles normalized to the peak values for each emission feature. The dark grey shaded region corresponds to PDR front position as defined by the peak of the 9.7 μm H_2 line and the light grey shaded region corresponds to the ionization front as defined by the [OI] 6300 Å line peak given in Salgado et al. (2016). G_0 profiles values are shown on the right y-axis in units of 10^3 Habings (see Section 3.6.2 for derivation).
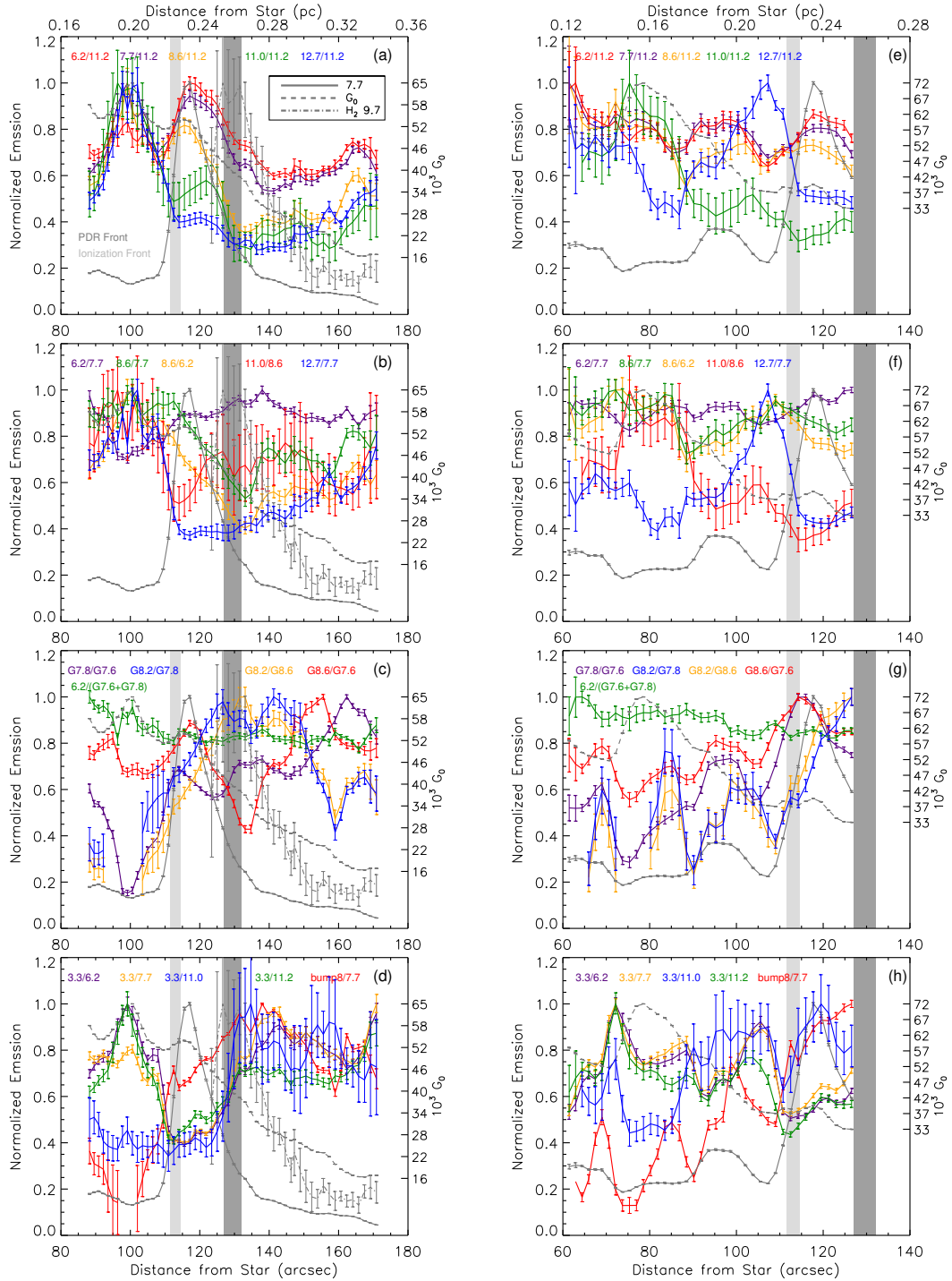
Figure 3.5: Orion Bar combined (left) and Orion Bar ionized (right) emission ratio profiles normalized to the peak values for each ratio. The dark grey shaded region corresponds to PDR front position as defined by the peak of the 9.7 μm H$_2$ line and the light grey shaded region corresponds to the ionization front as defined by the [OI] 6300 Å line peak given in Salgado et al. (2016). G$_0$ profiles values are shown on the right y-axis in units of 10^3 Habings (see Section 3.6.2 for derivation).

larger than 3 σ are presented here. We make use of the following groupings for the remainder of this section based on the relative position to the IF in each aperture as mentioned in Section 3.4.1, i.e in front of and behind the IF. For the following discussion, we further refer to the region between the IF and PDR front, encompassing the PAH peak, as the edge-on PDR and beyond the edge-on PDR front as 'further into the PDR' despite it being a face-on PDR (e.g. Boersma et al., 2012; van der Werf et al., 2013; Pabst et al., 2019). We refer to pixels in front of the IF as the H II region where we find the steep underlying dust continuum coinciding with the ionized cavity surrounding the Trapezium.

We find that all of the major PAH bands peak at the same distance from the illuminating source in both apertures between the edge-on PDR front, as defined by the 9.7 μm H_2 peak, and the edge-on ionization front, as defined by the [O I] 6300 Å line peak given in Salgado et al. (2016). The distance between the peak of the PAH emission and H_2 emission is 13.0 ± 3.6″, which agrees with the distance found between the 3.3 μm peak and the 2.122 μm H_2 peak of ~ 12 ± 2″ in Tielens et al. (1993). Salgado et al. (2016) found the ionization front to be located at 113 ± 1.5″, ~ 4″ in front of the PAH emission peak[4]. In this section, we will first discuss in detail the line projections along the OBC slit, followed by a discussion on the observed differences and similarities between the OBC and OBI slits.

Atomic Lines

In Figure 3.4 (a), the line profiles for each of the atomic emission lines peak inward of the ionization front towards the illuminating source in the following order: [Ar II], [Ne II], [Ar III], Pfund α, and [S IV] (which does not show a peak but a steady rise towards the star). Note that the order in which these atomic emission lines peak (aside from Pfund α) towards the star is directly related to the ionization potential of each respective species. The relative emission of these lines sharply drops from their peak emission moving away from the Trapezium cluster but they are still detected well beyond the IF.

Dust Emission

The dust continuum emission measured at 10.2 and 13.2 μm as well as the integrated 10-13.2 μm continuum emission generally agree with each other (Figure 3.4 (b)). These continua all have a strong peak at 100″ from the illuminating star, coinciding with the peak emission of [Ar III] and Pfund α. A secondary (local) continuum maximum, not seen in the [Ar III] and Pfund α emission, is found where the PAH emission peaks. These continuum measurements show a gradual decrease moving further away from the Trapezium cluster past the PAH emission peak into the PDR.

PAH Emission Features

All PAH bands, the Gaussian PAH sub-components from the 7-9 μm decomposition, the 5–10 and the 10–13 μm PAH plateaus show the same peak position within the PDR at 117″ from the illuminating star (see Figure 3.4 (c) and (d)). Moving towards the illuminating source, all of

---

[4]The cross–cut used by Salgado et al. (2016) crosses the IF at ~ RA, Dec: 5 35 19.4, -5 24 53.0 (J2000). This cross-cut intersects the OBI aperture at 113 ± 1.5″ from θ^1 Ori C. We assume the same position for the IF in OBC.

the PAH bands display a rapid decrease in emission strength but remain detected throughout (except for the G8.2 component and 3.6 μm bump). In contrast, further into the PDR, a more gradual decline occurs for all PAH emission features. Additionally, significant variations in the relative intensities of the PAH emission features become evident upon moving away from their shared peak position. In particular, the intensity at which the PAH features level off in the H ɪɪ region varies and does not seem to be solely governed by the ionization state of the feature's carrier. Further into the PDR, the drop in PAH band intensity (relative to the peak emission) varies with the 3.3, 11.2, 12.7, 6.2, 7.7, G11.0, and 8.6 μm band in decreasing order respectively. In other words, the PAH bands that are attributed to neutral species have a less pronounced decrease in relative flux in this region. Similarly, we find that the 7–9 μm Gaussian components show a decrease in relative intensity (with respect to the peak intensity) towards the illuminating source in the following order: G7.6, G8.6, G7.8, and G8.2 μm components. We note that the G8.2 component is very weak or absent in the H ɪɪ region. Further into the PDR, these components show a decrease in relative intensity in the reverse order to what is found in the H ɪɪ region: i.e. G8.2, G7.8, G7.6, and G8.6 μm. We note that the G7.6 μm component and LS derived 7.7 μm band have very similar spatial profiles in both apertures, reflecting the dominance of the G7.6 μm component to the 7.7 μm complex.

The 5–10 and 10–13 μm plateaus shown profiles very similar to the PAH bands within the edge-on PDR and have a gradual decline moving further into the PDR. The more significant aspect about these plateau profiles to note is the rapid drop at the IF to the point where they are no longer detected in the H ɪɪ region. Similarly, the 3.6 μm bump has a profile that is comparable with other PAH features, most notably the G8.2 μm component as it is derived from essentially the exact same spectral region.

PAH Emission Ratios

In Figure 3.5 (a), the 6.2/11.2, 7.7/11.2, 8.6/11.2, and 11.0/11.2 ratios are very comparable: these ratios show a broad maximum at the dust continuum peak, which coincides with the peak emission of [Ar ɪɪɪ] and Pfund α, and the PAH peak. Further into the PDR, these ratios all drop substantially, with a broad minimum behind the PDR front. Considering the relative strength of the maxima of these ratios at the dust continuum peak with their maxima at the PAH peak, these ratios can be organized in the following order: 11.0/11.2, 8.6/11.2, 7.7/11.2, 6.2/11.2. In other words, the 11.0/11.2 maximum at the dust continuum peak has the largest relative increase compared to its maximum at the PAH peak whereas the 6.2/11.2 shows the greatest relative decrease.

In Figure 3.5 (b), the 6.2/7.7 ratio shows little variation behind the IF. However, within the H ɪɪ region, the 6.2/7.7 ratio decreases to a minimum roughly co-spatial with the dust continuum peak. Interestingly, the 6.2/(G7.6 +G7.8) ratio shows very little variation (see Figure 3.5 (c)). This arises from the difference in the PAH behaviour being traced by the LS derived 7.7 μm band and the combined G7.6 and G7.8 μm components as they include emission from the 8 μm bump which is minimized within the H ɪɪ region (Figure 4.4). In contrast, the 8.6/7.7, 8.6/6.2 and 11.0/8.6 ratios are strong in the H ɪɪ region and weaker behind the IF.

The 12.7/11.2 and 12.7/7.7 emission ratios show overall similar trends, characterized by a strong peak near the dust continuum peak akin to the 11.0/11.2 ratio. However, despite each of these ratios showing a sharp decrease at the IF, these ratios differ with the 11.0/11.2 ratio as

they do not show any significant maxima near the PAH peak.

Regarding emission ratios between the 7–9 μm Gaussian components shown in Figure 3.5 (c), G7.8/G7.6 shows a very pronounced minimum at the dust continuum peak followed by a substantial rise towards the ionization front and a local minimum between the IF and the PDR front (as traced by H_2), followed by a rise moving further in the PDR. The G8.6/G7.6 ratio fluctuates across the line profile with local maxima roughly corresponding to the dust emission peak, the PAH emission peak and at 155″ further into the PDR. The G8.2/G7.8, G8.2/G8.6, and the 8 μm bump/7.7 emission ratios are comparable, with a strong minimum roughly corresponding with the dust continuum peak. Further from the illuminating star, these profiles shows a steep rise into the edge-PDR, which levels off near the edge-on PDR front. Further into the PDR, these ratios proceed to significantly drop again to a sharp local minimum found at $\sim 160″$ attributable to a 'blip' the G8.2 μm and 8 μm bump components here.

Overall, the 3.3/6.2, 3.3/7.7, 3.3/11.2 ratios all show similar trends with a strong peak near the dust continuum peak comparable with the 6–9/11.2 and 11.0/11.2 peaks here. However, each of these emission ratios involving the 3.3 μm have a minimum corresponding to the PAH peak followed by a subsequent rise further into the PDR. The 3.3/11.0 is unique amongst PAH ratios involving the 3.3 μm PAH emission feature as it shows very little variation in front of the IF and in the edge-on PDR. At the edge-on PDR front, this ratio increases considerably and plateaus further into the PDR within the large uncertainties.

Aperture Differences

The OBI aperture is a slightly different case in comparison to the OBC aperture as it does not intersect with the edge-on PDR front and extends much deeper into the ionized cavity surrounding the Trapezium cluster. The atomic lines show, in general, the same behavior as in the OBC aperture with the peak of the [Ne II], [Ar III] and H I Pfund α line being broader, encompassing the shoulder seen in the OBC slit (Figure 3.4 (e)). The 10–13.2 μm continuum profile (and the 10.2 and 14.2 μm continuum emission) is distinctly different in the OBI aperture with a continual rise towards the star and a broad peak much deeper into the H II region (Figure 3.4 (f)). Many of the atomic emission lines show a minor bump that can be associated with the dust continuum peak in the OBI aperture.

All of the major PAH bands excluding the 12.7 μm band show very similar profiles moving towards the source, with a somewhat broad local maximum centered at $\sim 98″$, a few arcseconds behind a corresponding small bump in the dust continuum profiles (Figure 3.4 (g) and (h)). Only minor variations in each profile are seen further inwards with a slight rise closest to the star. The emission ratio profiles between PAH features within the OBI aperture show very similar trends with those found for the OBC aperture in the H II region with each emission ratio generally having the same behaviour at the dust continuum peak and within the edge-on PDR (Figure 3.5 (e)–(h)). The most significant discrepancy between both apertures is the local maximum, the 'PAH bump', at $\sim 98″$ which is only found in the OBI aperture. In addition, the 12.7/11.2 and 12.7/7.7 ratios are notably different in the OBI aperture, with a strong peak in front of the IF and a broad minimum at the dust continuum peak. This peak coincides with the peak of the [Ne II] emission, which may influence the 12.15-13.2 μm decomposition we applied. Higher spectral resolution data from, for example, the James Webb Space Telescope, will settle this.

3.5.2 Correlation plots

We investigate possible intensity correlations between major PAH features in the 6–9 μm range as well as the 7–9 μm Gaussian components (Figure 3.6). We separate our data into two groupings based on the relative position to the IF: in the H II region (red) and the PDR (blue) as described in Section 3.4.1. For comparison, we include the observed correlation fits for the RN NGC 2023 (black line, Peeters et al., 2017) and the Orion Bar (green line, Galliano et al., 2008).

We observe a strong correlation between the 6.2 and 7.7 μm bands for the PDR spectra, which is significantly weaker within the H II region spectra (Figure 3.6 (a)). However, the 6.2 μm band and the sum of the G7.6 and G7.8 μm show a much tighter correlation in both types of spectra (Figure 3.6 (d)). This can be related to the line profiles of these features found in Figures. 3.4 and 3.5. We observe little variation in the 6.2/(G7.6 + G7.8) ratio but the 6.2/7.7 profile shows a large decrease in positions where the FUV radiation field was the strongest. If we compare (G7.6 + G7.8) μm directly with the 7.7 μm band (Figure 3.6 (e)), we find that they correlate equally strong as the 6.2 and 7.7 μm bands in the PDR spectra and better within the H II region spectra. We note the presence of a bi–modal distribution in the (G7.6 + G7.8) μm versus 7.7 μm relation, where the H II region data fit is steeper and located above the neutral data fit. This is seen to a lesser extent in the 6.2 versus 7.7 μm plot yet in the 6.2 versus (G7.6 + G7.8) μm plot, data points from both regions are strongly mixed. Comparing the 7.7 μm and the G7.6 μm component, we also find strong correlations in both the PDR and H II region.

Comparing the 6.2 and 8.6 μm bands (Figure 3.6 (b)), we again find a modest correlation in both the PDR and the H II region spectra, but numerous points are located well below the line of best fit for the PDR spectra. Notably, the 6.2 μm band and the G8.6 μm component are slightly better correlated in the PDR regime and are worse in the H II region (Figure 3.6 (h)). The 6.2 μm band versus G8.6 μm component plot also shows points far below the line of best fit and are worse in the H II region region. In both cases, we also see a separation between H II region and PDR data points. However, the PDR and H II region linear fits are reversed between the 6.2 versus 8.6 μm plot and the 6.2 versus G8.6 μm plot as the 8.6 is considerably weaker compared to the G8.6 in regions with weak or no G8.2 or 8 μm bump, i.e. the ionized gas in the H II region.

The 7.7 and 8.6 μm bands show the best correlation between the LS derived PAH features in the H II region spectra (Figure 3.6 (c)) with numerous points well above the line of best fit in the PDR region in a similar fashion as in the 6.2 versus 8.6 μm plot. However, the Gaussian sub-components show much more variation between each other. For instance, the G7.6 and G8.6 μm components show a strong correlation within the PDR spectra but there is significantly greater scatter found between them within the H II region spectra (Figure 3.6 (i)). The G7.8 and G8.2 μm components are moderately correlated in the H II regime and interestingly have a clear separation in data associated with the PDR and H II region spectra (Figure 3.6 (j)). The G7.8 and G8.6 μm components show moderate correlation in the PDR spectra and the H II region spectra but again have clear boundaries between both regimes (Figure 3.6 (k)). The G8.2 and G8.6 μm components also show two separate clusters of data points, but show a significantly better correlation in H II region spectra (Figure 3.6 (l)). Finally, comparing G8.6 with (G7.6 + G7.8) μm, we find a strong correlation within the PDR spectra and a lower correlation in the H II region spectra (Figure 3.6 (f)).
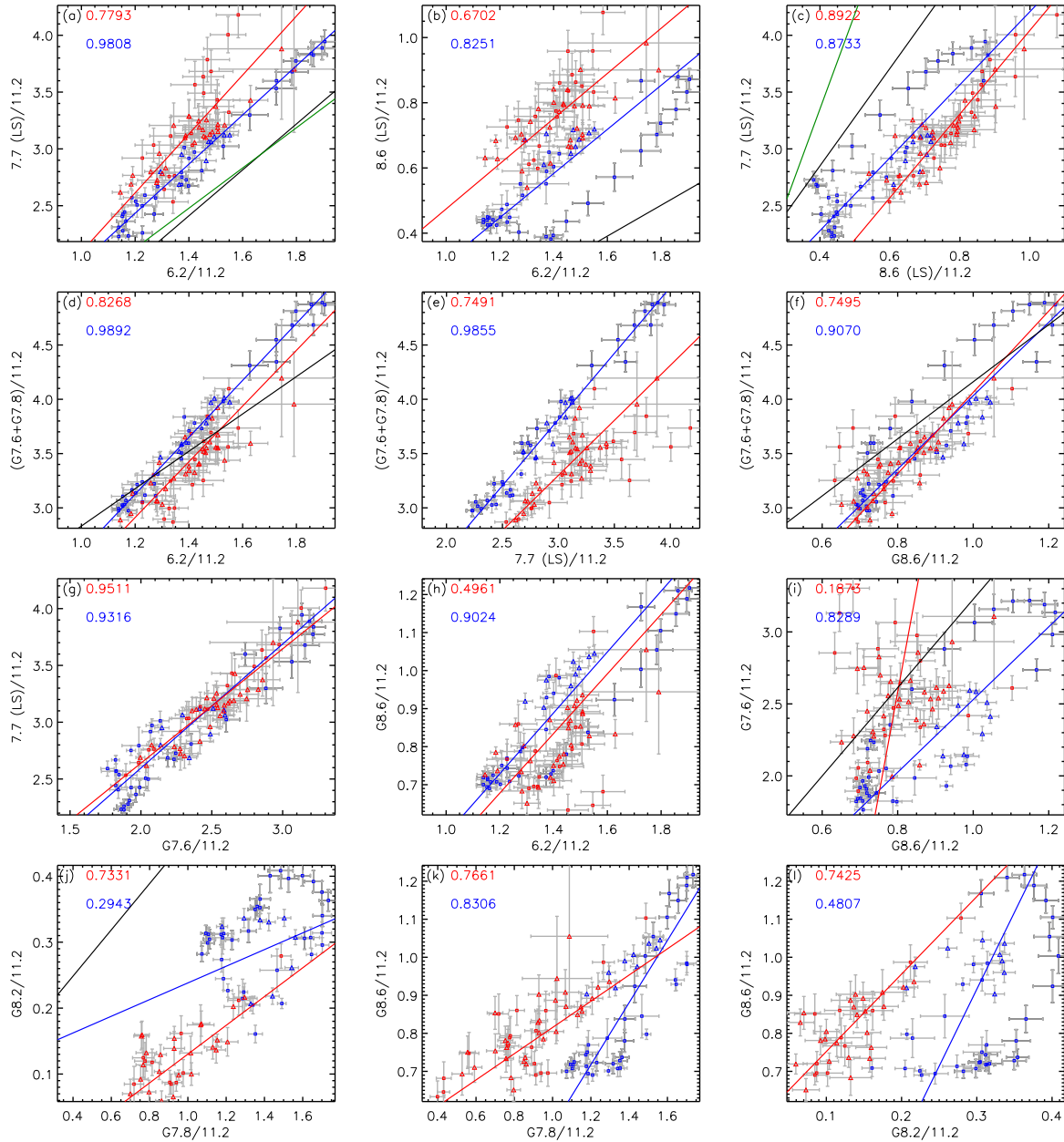
Figure 3.6: PDR spectra are shown in blue and H II region spectra for the Orion Bar Combined (squares) and the Orion Bar Ionized (triangles). Correlation coefficients for each respective region are given in the same color. Weighted and unweighted linear fits are shown as solid and dashed lines for each respective region given in the same color. The black and green lines correspond to the respective correlation fits found for NGC 2023 in Peeters et al. (2017) and the Orion Bar using the spline method in Galliano et al. (2008) respectively.
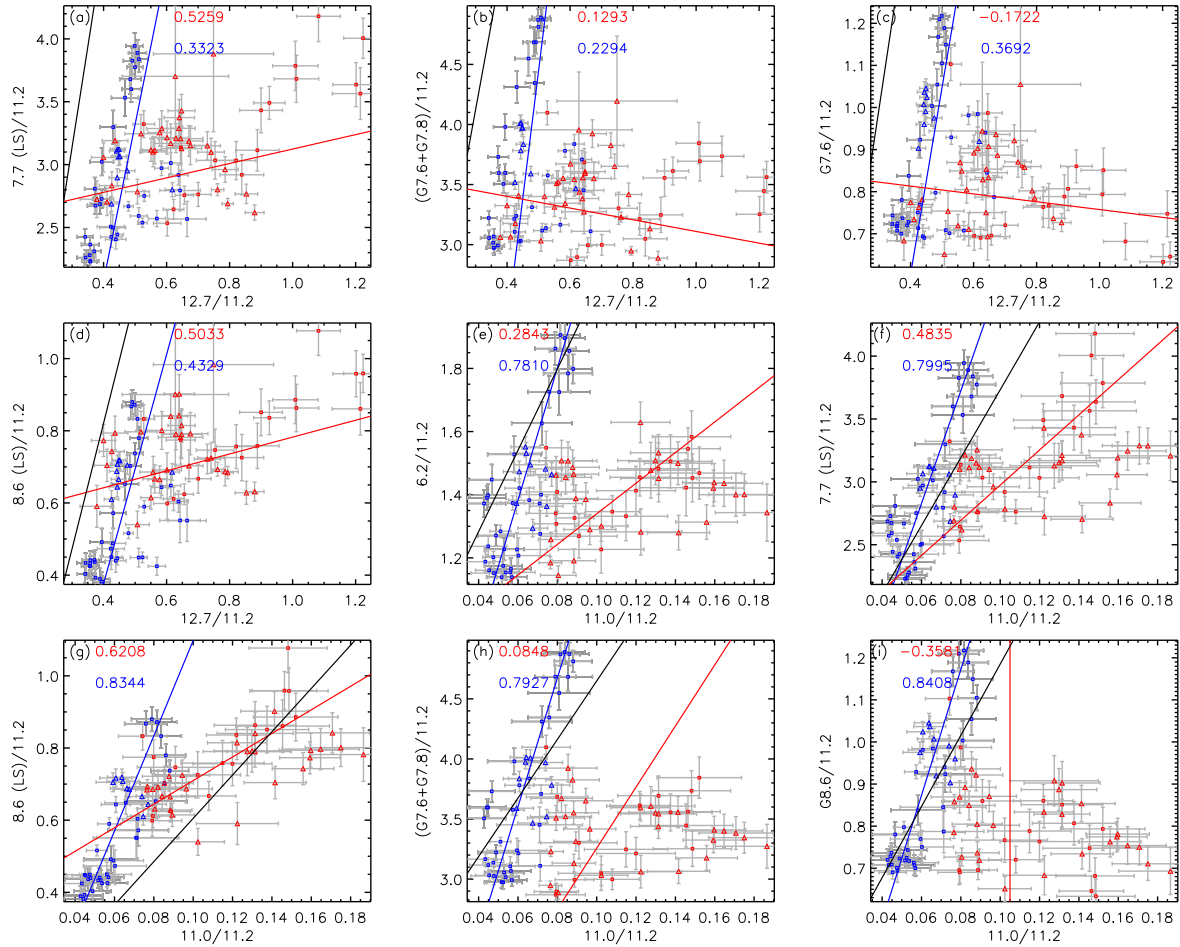
Figure 3.7: Orion Bar correlation plots II: PDR spectra are shown in blue and H ɪɪ region spectra for the Orion Bar Combined (squares) and the Orion Bar Ionized (triangles). Correlation coefficients for each respective region are given in the same color. Weighted and unweighted linear fits are shown as solid and dashed lines for each respective region given in the same color. The black lines correspond to the respective correlation fits found for NGC 2023 in Peeters et al. (2017).

In Figure 3.7, we compare the 6-9 μm bands and 7–9 μm Gaussian components with the 11.0 and 12.7 μm bands. We note that the behaviour of the 11.0 μm in the PDR and H II region spectra tends to change drastically, these correlation fits show two distinct distributions. The 6.2 μm band shows a reasonable correlations with the 11.0 μm band in the PDR spectra and a much weaker correlation within the H II region spectra (Figure 3.7 (e)). These trends are closely mimicked in the 11.0 μm band versus the sum of G7.6 and G7.8 μm plot (Figure 3.7 (h)), which we again note is very well correlated with the 6.2 μm band. The 7.7 and 11.0 μm bands are well correlated within the PDR spectra (Figure 3.7 (f)), but again falls off considerably in the H II region spectra. We find that the 8.6 μm shows the best correlation with the 11.0 μm band of the features probed (Figure 3.7 (g)), with strong to moderate correlations in the PDR and H II region spectra respectively. The G8.6 μm component shows a strong correlation with the 11.0 μm in the PDR spectra, but does not correlate at all in the H II region spectra, showing that it is clearly different from the LS derived 8.6 μm feature (Figure 3.7 (i)). We do not find any strong correlations with the 12.7 μm band. The 7.7 and 8.6 μm bands both show weak correlations with the 12.7 μm band with both slightly better correlated with the 12.7 μm within the H II region spectra (Figure 3.7 (a) and (d)). Interestingly, the 12.7 μm band and sum of G7.6 and G7.8 μm components (and the 6.2 μm band by extension) show even poorer correlations with both spectral regimes showing clear differences in behaviour (Figure 3.7 (b)). Comparing the 12.7 μm band with solely the G7.6 μm component gives a slightly better correlation than the sum of the G7.6 and G7.8 μm in the PDR spectra, while there is essentially no correlation within the H II region spectra (Figure 3.7 (c)).

3.6   Discussion

In Section 3.5, we presented the behaviour of the emission features observed towards the Orion Bar. Here, we investigate potential drivers of this behaviour such as the environmental conditions and properties of the underlying PAH populations detected in the IRS SL spectra.

3.6.1   Probing PDR Morphologies

In Section 3.5, we grouped the Orion spectra in both apertures into two groups based on the relative position of each pixel to the edge-on IF of the Orion Bar (Figure 3.8 (a)). Using this grouping, the correlations found are significantly worse than reported for the Orion Bar and other PDR sources in the literature (e.g. Galliano et al., 2008; Boersma et al., 2014a; Stock et al., 2016; Stock & Peeters, 2017; Peeters et al., 2017). One explanation for this lack of correlation may be due to a inadequate account of the different PDR morphologies present within our Orion pointings. We briefly alluded to the positions behind the edge-on PDR front in the Bar as being part of a face-on PDR in Section 3.5.1 as shown in diagrams depicting the structure of the Orion Nebula such as in Boersma et al. (2012); van der Werf et al. (2013); Pabst et al. (2019). From these diagrams, it is also clear that the spectra coming from the H II region includes emission from the face-on PDR located behind the ionized cavity along the line of sight.

In order to investigate the effects of PDR morphology on behaviour found within Figures 3.6 and 3.7, we now employ a different grouping of these spectra. In one group we only include
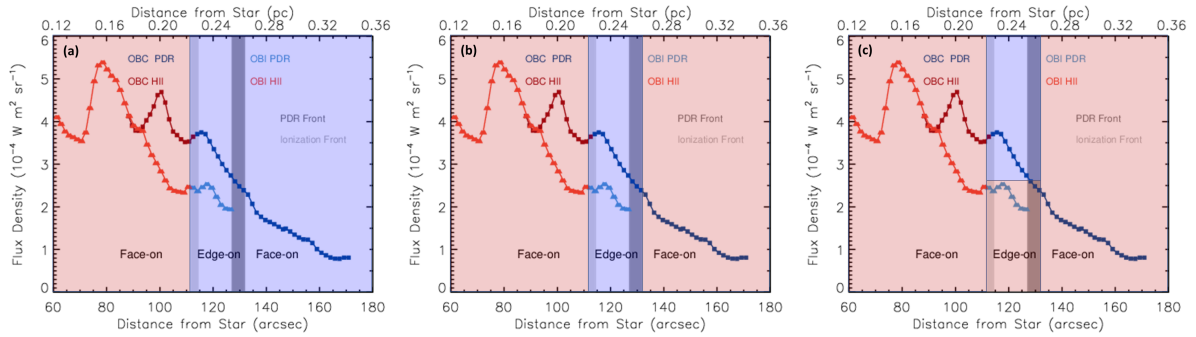
Figure 3.8: The 10–13.2 μm continuum profile for Orion Bar combined (squares) and Orion Bar ionized (triangles). We highlight in panel (a), the pixel grouping used for Figures 3.6 and 3.7, panel (b) for Figure 3.9 and panel (c) for Figure 3.10 (see Section 3.6.1 for details). OBC PDR and H II region pixels are in dark blue and red respectively. OBI PDR and H II region pixels are in light blue and red respectively. The dark grey shaded region corresponds to PDR front position as defined by the peak of the 9.7 μm H_2 line and the light grey shaded region corresponds to the ionization front as defined by the [OI] 6300 Å line peak given in Salgado et al. (2016). Face-on and Edge-on labels refer to positions where these are thought to be the dominant PDR morphologies as detailed in Section 3.6.1.

the spectra from the edge-on PDR, bounded by the edge-on IF and PDR front, and in the other, all spectra of the face-on PDR located in front of the IF and behind the edge-on PDR front of the Orion Bar (Figure 3.8 (b)). In Figure 3.9, we show correlations between the 6–9 μm PAH emission features using this grouping of edge-on and face-on PDRs. In the 6.2 versus 7.7 μm correlation plot (Figure 3.9 (a)), the vast majority of the edge-on PDR points are traced well by a line that lies below the face-on PDR points. The exception is a few of the OBI edge-on PDR points that seem to mix with the face-on PDR points. Thus, the spectra located behind the Bar agree better with those in front of the Bar rather than within the Bar. In both the 6.2 versus 8.6 and 8.6 versus 7.7 μm correlation plots (Figure 3.9 (b) and (c)), the 'line' of outliers located respectively below and above the majority of the data points in our sample can be traced back to the OBC edge-on PDR. Thus, the correlations found between the 6.2, 7.7, and 8.6 μm bands shown between the 'blue' data points in Figure 3.6 are fitting primarily the face-on PDR spectra located behind the Bar in the OBC aperture and the OBI edge-on PDR spectra. The latter oddly seems to show more similarities with the face-on PDR spectra than the OBC edge-on PDR spectra. This suggest that the environment of the Bar within the OBI aperture is notably distinct from that within the OBC aperture. We also note that the correlations between 6.2, 7.7 and 8.6 μm for all of the face-on PDRs (as traced in red in Figure 3.9) is much better than just the H II region spectra (as traced in red in Figure 3.6). Conversely, correlations involving the 8.6 μm band for pixels in the edge-on PDRs is markedly worse due to the discrepancy between the OBI and OBC spectra in the Bar.

To this end, we use a third grouping (Figure 3.8 (c)) in which the OBC edge-on PDR spectra are grouped by themselves with all of the face-on PDR and the OBI edge-on PDR spectra in a second group (Figure 3.10). In each of these plots, there appears to be a bi-linear trend that clearly separates the OBC edge-on spectra from the remainder of the spectra. The
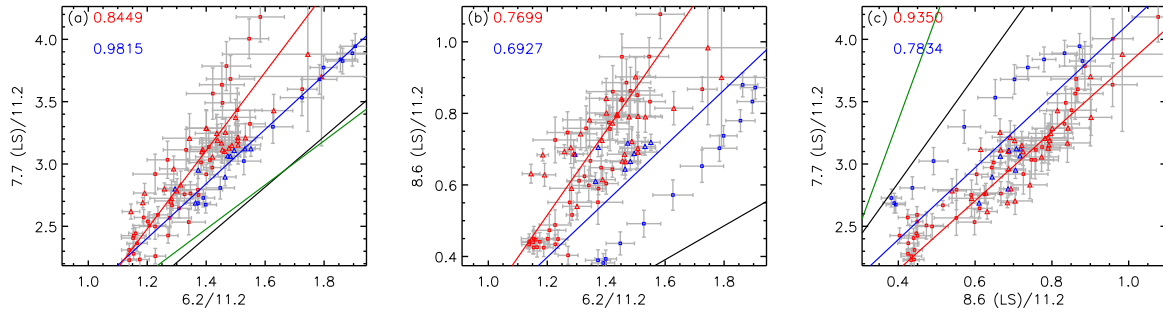
Figure 3.9: Orion Bar correlation plots III: Edge-on PDR spectra are shown in blue and face-on PDR spectra in red for the Orion Bar Combined (squares) and the Orion Bar Ionized (triangles). Correlation coefficients for each group are given in their respective color. Weighted and unweighted linear fits are shown as solid and dashed lines respectively for each respective region in their color. The black and green lines correspond to the respective correlation fits found for NGC 2023 in Peeters et al. (2017) and the Orion Bar using the spline method in Galliano et al. (2008) respectively.

addition of the OBI edge-on PDR to the face-on PDR spectra group shows a slight decline in correlations found within this set of spectra, suggesting that the OBI edge-on PDR has its own unique behaviour. With the exception of the OBI edge-on PDR spectra, these plots suggest that the relative morphology of a PDR can be discerned from the relative slope in the line of best fit for a given morphology. Other studies have shown the presence of bi-linear trends or bifurcation between different PAH emission features (e.g. Stock et al., 2016; Stock & Peeters, 2017, Chapter 4). This bifurcation has been attributed to probing different physical environments with the low G_0 diffuse ISM being distinct from high G_0 H II regions.

The level of photoprocessing we observe in a given PDR depends on the relative contribution of regions with different physical conditions along our line of sight (e.g. Chapter 2). In an edge-on PDR, when resolved, we are able to investigate how the PAH population changes moving from the dense molecular region into the PDR to the ionization front closer to a FUV radiation source. This is not possible for a face-on morphology as all these distinct zones are mixed within a single pixel or resolution element. As the PAH population changes within an extended source, an edge-on or face-on PDR morphology results in different fractional contributions to the total PAH emission of the various PAH subpopulations. The bi-linearity we find within our correlations thus indicate that these different PAH subpopulations have distinct intrinsic relative PAH intensities.

Next, we compare the PAH ratio trends we find for the OBC edge-on PDR data with those found by other studies. Galliano et al. (2008) studied ISOCAM observations of the Orion Bar which included the ionized region, the Orion Bar as well as the region behind the Bar. These observations thus cover all the different regions discussed above. These authors also find tight correlations between the 6.2 versus 7.7 and the 7.7 versus 8.6 μm bands. However, their correlation is offset from our data points (Figure 3.6 (a) and (c)). For both correlations, the data points corresponding to the OBC edge-on PDR are significantly closer to their correlation (and thus data points) than the remainder data points within our apertures. The origin of the offset
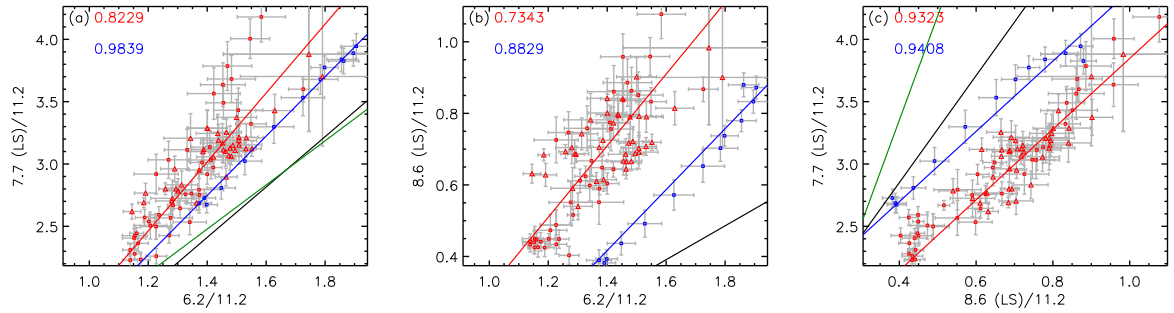
Figure 3.10: Orion Bar correlation plots IV: OBC edge-on PDR spectra are shown in blue and face-on along with OBI edge-on PDR spectra in red for the Orion Bar Combined (squares) and the Orion Bar Ionized (triangles). Correlation coefficients for each region are given in their respective color. Weighted and unweighted linear fits are shown as solid and dashed lines respectively for each respective region in their color. The black and green lines correspond to the respective correlation fits found for NGC 2023 in Peeters et al. (2017) and the Orion Bar using the spline method in Galliano et al. (2008) respectively.

between the trends in both datasets of the Orion Bar is currently unclear and warrants further investigation. However, such offsets are also seen for other sources. Indeed, for the reflection nebula NGC 2023 (Peeters et al., 2017) the correlations are in most cases displaced from our trends albeit parallel. Here as well, they are closest to what we found for the OBC edge-on PDR. Moreover, while not directly compared here, Stock et al. (2016) reported that the reflection nebula NGC 1333 shows correlations that closely mimic those of NGC 2023. Thus, the OBC edge-on PDR is much better representative of a prototypical PDR spectra that what we find in the face-on PDR spectra and the OBI edge-on PDR spectra.

One particularly interesting trend found in our data is the deviation of the 6.2 and 7.7 μm ratio from the usual very tight correlation in the H II region within the OBC aperture. This is evident from the line profile of 6.2/7.7 within the OBC aperture where we see a stark minimum at the G_0 peak (Figure 3.5 (b)). Notably, we do not find a similar trend in the line profile of the OBI aperture. The deviation in the behaviour of the 6.2 and 7.7 μm bands has been previously reported by Stock et al. (2014) and Whelan et al. (2013) within other H II regions. Stock et al. (2014) suggests this behaviour arises from the different vibrational assignments of these features, namely the 6.2 μm band is attributed to C–C stretching whereas the 7.7 μm band is a combination of the C–C stretching and C–H in plane bending modes (i.e. Allamandola et al., 1989). Indeed, they suggest this breakdown arises from the dominance of the C–H in plane bending mode within the ionized cavity. Based on this assessment, Stock et al. (2014) surmises that the 8.6/7.7 ratio should also show an increase within the ionized cavity as the 8.6 μm band is attributed to C–H in plane bending which they found to be consistent with their observations. In Figure 3.5 (b), we do indeed find a rise in the 8.6/7.7 ratio in the OBC aperture moving from the edge-on PDR front towards the H II region. This trend is opposite to that of the 6.2/7.7, which begins to drop at the edge-on PDR front towards the H II region. Despite the fluctuations of the 8.6/7.7 ratio in the OBI aperture, they are not in sync with changes in

the environment. This is supported by Figure 3.6 (a) where the 6.2 and 7.7 μm bands have a much weaker correlation in the H II region while conversely the 7.7 and 8.6 μm bands have a stronger correlation in this region relative to the PDR. This indicates that there is a substantial shift in the vibrational behaviour of the underlying PAH population as they are increasingly exposed to the stellar FUV radiation field as they move into the H II region.

3.6.2 Environmental Diagnostics

Deriving PDR Conditions

We determine the FUV radiation field strength, G_0, across our apertures following the method employed by Galliano et al. (2008). Briefly, these authors measured the very small grain (VSG) continuum emission from 10 to 16 μm to determine G_0 using the relationship $G_0 \propto I_{cont}^{1/1.3}$ and the absolute value of $G_0 = 4 \times 10^4$ at the PDR front taken from Tauber et al. (1994).

First, we measured the integrated strength of the dust continuum emission from 10–13.2 μm. To connect this 10–13.2 μm continuum flux with the 10-16 μm VSG continuum of Galliano et al. (2008), we use ISO-SWS spectra positioned across the Bar[5]. For these spectra, we determined the ratio of the integrated strength of the underlying dust continuum from 10–13.2 and 10–16 μm to be an average of 2.2 ± 0.1 over the five SWS pointings, indicating that these continua are effectively proportional. Using the absolute value of G_0 at the edge-on PDR front in the Bar as reported by Tauber et al. (1994), we calculate the G_0 profile for the OBC aperture using the following scaling relationship:

$$G_0(r) = G_0(\text{PDR}) \left(\frac{I_{10\text{–}13\,\text{cont}(r)}}{I_{10\text{–}13\,\text{cont}}(\text{PDR})} \right)^{1/1.3} \tag{3.1}$$

where PDR refers to the position of the PDR front and r refers to an arbitrary position in the OBC aperture. This results in G_0 ranging from 1.6–6.5 × 10^4 in this aperture with G_0 peaking in the H II region. The derived G_0 profile is shown in Figures 3.4 and 3.5.

We were not able to use the absolute value of G_0 at the PDR front for the OBI G_0 aperture since it does not intersect the PDR front. Instead, we take the average of the OBI 10–13.2 μm continuum between 87–95″ where we observe comparable strength with the OBC 10–13.2 μm continuum (Figure 3.8). As a consequence, we assume both apertures have similar G_0 at these positions and we use the mean G_0 of the OBC aperture in this overlap region of (5.686 ± 0.004) × 10^4 as the reference value in equation 3.1 for the OBI aperture. In addition, we use the mean OBI 10–13.2 μm continuum strength in the overlap region as the reference value for the corresponding continuum measurement. The resulting G_0 values range from 3.3–7.2 × 10^4 with a strong peak deep into the H II region. The derived G_0 profile is shown in Figures 3.4 and 3.5.

The G_0 profiles derived for the OBC and OBI apertures are quite different with respect to their absolute values within the edge-on PDR and their peak positions in the H II region. This is indicative of a non-uniform structure throughout the Bar, similarly to the divergent emission

---

[5]There are five ISO-SWS spectra available across the Orion Bar at a distance of 2.597′, 2.175′, 1.971′, 1.766′, 1.356′ from θ^1 Ori C referred to as positions D2, H2S1, D5, Brγ, and D8 respectively (e.g. Peeters et al., 2002; van Diedenhoven et al., 2004). Their target dedicated time (TDT) numbers, a unique identifier, are 69502005, 69501806, 83101507, 69502108, and 69501409 respectively, see Chapter 2 for their FOVs.

and ratio profiles as reported in Section 3.6.1. This supports previous results that have shown variations in the emission substructure of molecular species in the Bar (e.g. Goicoechea et al., 2017). For this reason, we analyse both of our apertures separately.

Furthermore, we derive the PAH ionization parameter, $\gamma = G_0 T^{0.5}/ n_e$ (Bakes & Tielens, 1994) where n_e is the electron density and T the gas temperature, using the same method as described in Galliano et al. (2008). We take the values for both gas density, n_H, and temperature at the PDR front of 5×10^4 cm^{-3} and 500 K respectively as derived in Tauber et al. (1994). The gas density is then converted to electron density using the assumption that all free electrons result from the photo-ionization of carbon and all gas–phase carbon is ionized, $n_e \simeq$ (C/H) $n_H \simeq 1.6 \times 10^{-4}$ n_H, where 1.6×10^{-4} is the interstellar gas-phase carbon abundance (Sofia et al., 2004). Under the assumption that the electron density and gas temperature remains constant within both pointings, we derive a γ value for all spectra. We find γ ranges from ~ 1.5–5.8×10^3 in the PDR positions and from ~ 3.0–6.4×10^3 in the H II region positions.

PAHs as PDR Tracers

In Figure 3.11, we compare our Orion Bar data with the previously established relationship of Stock & Peeters (2017) between G_0 and G7.8/G7.6. We observe a strong anti-correlation between these two parameters with G7.8/G7.6 being high in low G_0 environments, consistent with Stock & Peeters (2017). In the left panel of this figure, we first compare these parameters in the PDR and H II region grouping (see 3.5.2) of the OBC and OBI apertures separately. We find a strong anti-correlation in the OBC aperture, a significantly weaker correlation in the OBI H II region, and a strong positive correlation in the OBI PDR aperture. The latter, however, only probes a very small range in G_0. Compared to the results of Stock & Peeters (2017), our linear fits are significantly steeper. This may be attributed to i) the much smaller range of G0 values covered here and ii) the fact that we only probe high UV field regions relative to the range given in Stock & Peeters (2017). In fact, if we only consider the H II region observations of Stock & Peeters (2017), the slope of their relation will increase substantially. Additionally, it should be noted that these authors only consider the global, spatially integrated, values of G_0 and G7.8/G7.6 in each of the sources they included in their relationship, which resulted in considerable uncertainties in G_0.

We discussed in Section 3.6.1 that the PDR versus H II region grouping fails to take the underlying differences in PDR morphology into account. In order to understand the effects of PDR morphology on the G7.8/7.6 ratio versus G_0, we use a different grouping of our data, i.e. the grouping with the OBC edge-on PDR in one group and all of the face-on and the OBI edge-on PDR in the second group (Figure 3.11, right panel). In the OBC edge-on PDR, we find a moderate anti-correlation but more interestingly, the linear fit to these data points agrees within the uncertainties with the Stock & Peeters (2017) relationship that excludes the diffuse ISM. Additionally, we find that the grouping including the face-on PDRs and the OBI edge-on PDR has a very strong correlation between G7.8/7.6 ratio and G_0 with a steeper slope than the (Stock & Peeters, 2017) relationships. This suggests that an edge-on and face-on PDR morphology may generally also yield a different linear relationship between G7.8/G7.6 and G_0. Despite the differences between these studies and between face-on and edge-on PDRs, it is clear that the the G7.8/G7.6 has the potential to become a useful tracer of the FUV radiation field for a wide
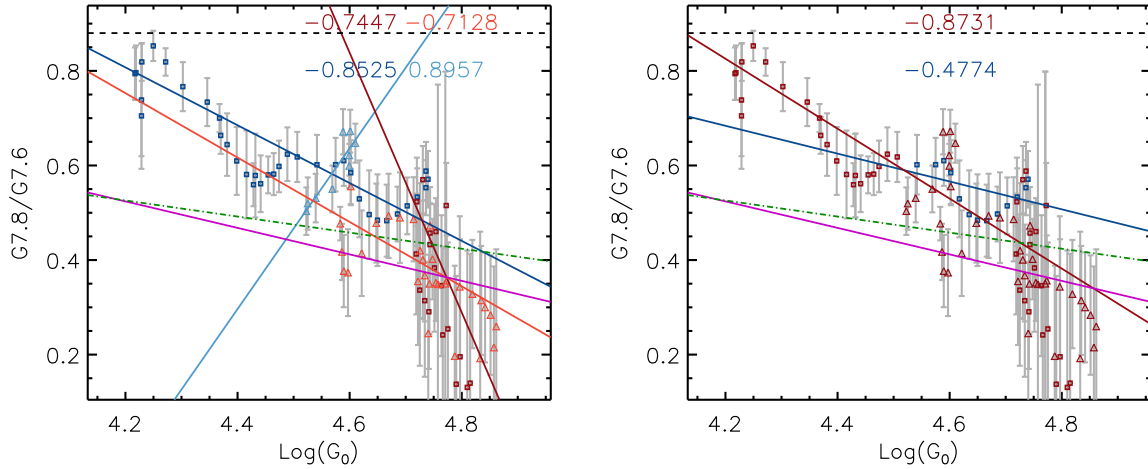
Figure 3.11: G_0 versus G7.8/G7.6: Orion Bar combined (squares) and Orion Bar ionized (triangles). *left* OBC PDR and H II region pixels are in dark blue and red respectively and OBI PDR and H II region pixels are in light blue and red respectively. *right* OBC edge-on PDR in dark blue and all face-on and OBI edge-on PDRs in dark red. Correlation coefficients for each respective region are given in the same color as listed above. Weighted linear fits are shown as solid lines for each region in their respective color. The linear fits derived in Stock & Peeters (2017) are given as a green dot-dashed line and magenta solid line where they do and do not include the Ophiuchus diffuse cloud pointings. The maximum G7.8/G7.6 ratio of 0.88 found in the outskirts of W49A by Stock & Peeters (2017) is shown as a black horizontal dashed line.

variety of PDRs.

Next, we investigate the relationship between the PAH ionization parameter, γ, and the 6.2/11.2 ratio and compare with the results reported by Galliano et al. (2008) (see Figure 3.12). Overall, we do not observed a very strong relationship between these parameters. However, as before, we consider the OBC and OBI apertures in the H II region and the PDR separately. In this case, we find strong and modest correlations between these parameters in the PDR and H II region, respectively, for the OBC aperture, and a negligible correlation for both regions within the OBI aperture. These linear fits are much shallower than the relationship derived by Galliano et al. (2008) with the exception of the OBC PDR. Interestingly, these authors derived their relationship based on selected positions within the edge-on PDR for Orion along with two pointings from a reflection nebula and a planetary nebula (which have $\gamma < 10^3$). Our edge-on PDR data points seem to be just below the Galliano et al. (2008) fit in both apertures.

We have established previously that the grouping of the face-on PDR spectra behind the Bar with the edge-on PDR in the OBC aperture fails to trace the PAH emission ratio behaviour in both regions (Section 3.6.1). In this case, the data points attributed to the OBC face-on PDR in Figure 3.12 below $\gamma < 2000$ follow a different trend in comparison to the OBC edge-on PDR region points above this threshold causing this fit to be much poorer than if we consider these regions separately. Thus, we again make use of the grouping with the all of the edge-on PDRs and all of the face-on PDRs are separated (Figure 3.12, right panel).The combination of the
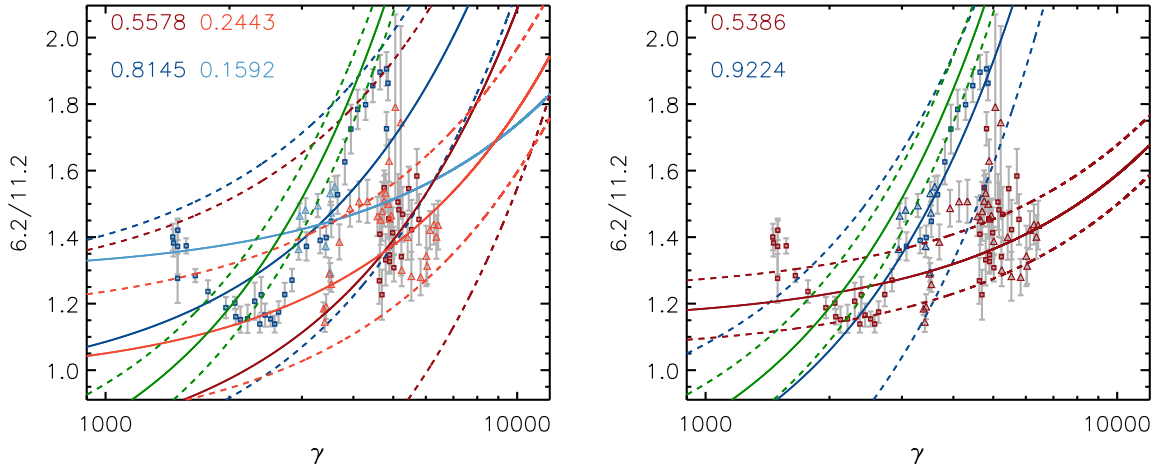
Figure 3.12: PAH ionization parameter γ versus 6.2/11.2: Orion Bar combined (squares) and Orion Bar ionized (triangles). *left* OBC PDR and H II region pixels are in dark blue and red respectively and OBI PDR and H II region pixels are in light blue and red respectively. *right* All edge-on PDRs in dark blue and all face-on PDRs in dark red. Correlation coefficients for each region are given in the same color as listed above. Weighted linear fits and their 1 σ fit uncertainties are shown as solid and dashed lines respectively for each region in their respective color. The linear fit derived by Galliano et al. (2008) is shown as a solid green line with dashed green lines representing the 1 σ deviations.

OBC and OBI edge-on PDRs gives a tight correlation between the 6.2/11.2 ratio and γ despite the disagreement that has been found between these edge-on PDRs in most other relationships we have considered. The combined edge-on PDRs agree quite well with the Galliano et al. (2008) fit within the corresponding fit uncertainties. In contrast, the combined face-on PDRs do not seem to be well correlated with respect to 6.2/11.2 ratio and γ. This suggest that the relationship between these parameters only seems to hold within edge-on PDRs.

3.7 Conclusion

In this chapter, we investigate the characteristics of the PAH emission features across the Orion Bar through the use of *Spitzer* IRS SL spectroscopic observations consisting of two apertures that cross the Bar at different locations along with *SOFIA* FLITECAM imaging observations. We make use of the spline decomposition method to separate the PAH emission features from the underlying continuum components. We measure the fluxes on the various emission components found within both spectral apertures including the PAH emission and related components, the atomic recombination lines, the H_2 lines, and the underlying dust continuum. Variations in these spectral components are found using line profiles taken with respect to distance from the primary illuminating source in the Orion Nebula. Correlations between the PAH related features are considered based on the relative position to the ionization front of the Orion Bar as well as the different PDR morphologies present in each aperture, these being edge-on and

face-on. Finally, we compare specific PAH emission ratios with the derived profiles of the FUV radiation field and the PAH ionization parameter. Our major findings are as follows:

- All of the PAH-related emission is found to have a strong peak located within the Orion Bar. Variations in PAH features become more prominent away from this peak into the H II region in front of the Bar and further into the PDR. Additional maxima or mimima in the PAH emission profiles and PAH ratio profiles were found to typically coincide with the G_0 peaks as defined by the dust continuum emission profile in each aperture.

- Grouping the spectra based on PDR morphology yielded much tighter correlations between the PAH emission features in comparison to grouping based on relative position to the ionization front in general. PAH emission correlations in many cases demonstrated two distinct trends that were attributed to the edge-on PDR of the Bar and the face-on PDRs located in front of and behind the Bar.

- The PAH emission within the edge-on PDRs between both apertures is found to behave differently suggesting the Bar is not a uniform structure.

- Deviation from the well-known tight relationship between the 6.2 and 7.7 μm bands is found to occur at the peak of the radiation field within the H II region. This was found to correspond with the enhancement of the 8.6/7.7 profile suggesting a shift in the relative strength of the intrinsic vibrational modes in this region.

- We are able to replicate the anti-correlation found between the G7.8/G7.6 and G_0 of Stock & Peeters (2017) in both the H II region and the PDR. Using a grouping based on PDR morphology showed that the OBC edge-on PDR displayed a similar linear relationship as was found by Stock & Peeters (2017) whereas the face-on PDRs showed a steeper relationship.

- We replicate the linear relationship found between 6.2/11.2 and the ionization parameter of Galliano et al. (2008) within the edge-on PDR spectra. In contrast, the face-on PDR spectra show a much weaker (or no) relationship between these parameters.

To summarize, the Orion Bar PDR has clearly earned its reputation as the prototype edge-on PDR. We show clear stratification of the relative intensities of the PAH emission features within the different layers of the Orion Bar yielding insight into the physical and chemical structure of this well-studied environment. However, the murkier face-on PDRs on both sides of the Bar also deserve closer scrutiny as few observed PDRs are as unambiguous as the Orion Bar. Novel JWST observations within the coming years of the Orion Bar will allow us to further advance our understanding of astronomical PAHs and their relationship with the PDR environments.

Acknowledgements

Chapter 4

PAH emission in the Reflection Nebula NGC 1333

C. Knight[1], E. Peeters[1,2,3], M. G. Wolfire[4], D.J. Stock[1]

[1]*Department of Physics and Astronomy, University of Western Ontario, London, ON N6A 3K7, Canada; cknigh24@uwo.ca*

[2]*Institute for Earth and Space Exploration, University of Western Ontario, London, ON, N6A 3K7, Canada*

[3]*Carl Sagan Center, SETI Institute, 189 N. Bernardo Avenue, Suite 100, Mountain View, CA 94043, USA*

[4]*Department of Astronomy, University of Maryland, College Park, MD 20742, USA*

4.1 Introduction

The mid-infrared (MIR) spectra of a vast number astronomical sources are dominated by prominent emission features at 3.3, 6.2, 7.7, 8.6, 11.2, and 12.7 μm along with weaker associated bands found at 5.2, 5.7, 6.0, 11.0, 12.0, 13.5, and 14.2 μm. These features are widely attributed to the infrared fluorescence of polycyclic aromatic hydrocarbons (PAHs) (e.g. Léger & Puget, 1984; Allamandola et al., 1985, 1989; Puget & Léger, 1989) and related carbonaceous species such as PAH clusters, polycyclic aromatic nitrogen heterocycles (PANHs, Hudgins et al., 2005; Bauschlicher et al., 2008) or PAHs with functional groups attached (e.g. Joblin et al., 1996a; Sloan et al., 1997; Pilleri et al., 2015; Maltseva et al., 2016; Shannon & Boersma, 2019). These species are all characterized by their shared molecular composition, made up primarily of a planar collection of fused benzene rings with hydrogen atoms located on the outer edges. These molecules are electronically excited by the absorption of far-ultraviolet (FUV) photons from a nearby stellar source. This energy is rapidly redistributed to lower lying vibrational states, where these molecules cascade back to their ground state by radiating MIR photons corresponding to vibration relaxation. Astronomical sources where these bands have been routinely observed include: H II regions, young stellar objects (YSOs), post-AGB stars, planetary nebulae (PNe), reflection nebulae (RNe), external galaxies as well as the diffuse ISM (e.g. Hony et al., 2001; Verstraete et al., 2001; Peeters et al., 2002; Berné et al., 2007; Smith et al., 2007a; Galliano et al., 2008; Boersma et al., 2012; Shannon et al., 2016; Stock et al., 2016).

The spectral fingerprints of these PAHs show significant variation with respect to the relative intensities, profile shape, and peak positions between sources and spatially within extended

sources. Intensity variations are mainly attributed to the molecular charge state, i.e. the PAH emission in the 6–9 μm range increases in cationic species, whereas the 3.3 and 11.2 μm bands are more prominent in neutral species (Allamandola et al., 1989), the 12.7 μm band has both cationic and neutral components (Peeters et al., 2012; Boersma et al., 2013; Shannon et al., 2016, e.g.). To a lesser extent, intensity variations are driven by the size distribution of a PAH population because smaller molecules tend to have less vibrational modes available, hence they have more energy per mode or reach a higher internal temperature upon the absorption of a FUV photon (Schutte et al., 1993; Croiset et al., 2016, Chapter 2). Additionally, intensity variations in PAH bands in the 10–15 μm range are attributed to structural differences in their carriers, i.e the 11.2 μm band is stronger in compact–symmetrical species whereas the 12.7 μm band becomes more prominent in species with an irregular edge structure (e.g. Hony et al., 2001).

PAH molecules are observable in photo-dissociation regions (PDRs). These are regions where the FUV photons of energies between > 6 eV and < 13.6 eV (i.e. the ionization energy of hydrogen) control the physics and chemistry of the gas and which includes primarily neutral hydrogen and molecular hydrogen dominated, IR-luminous regions that encompass H II regions around young, massive stars (Melnick et al., 1979; Storey et al., 1979; Russell et al., 1980, 1981). PDRs extend to a wide variety of neutral environments, in fact they account for all atomic and a minimum of 90% of the molecular gas in the Galaxy (Hollenbach & Tielens, 1999).

In addition to PAH emission features, observed emission features within PDRs include the far-infrared (FIR) dust continuum, H_2 emission lines, the atomic fine structure lines of species such as [O I] and [C II], and CO rotational lines. These emission features have all proven to be useful in predicting the physical conditions of PDR environments through the use of PDR modelling (e.g. Tielens & Hollenbach, 1985b; Wolfire et al., 1990; Kaufman et al., 1999; Young Owl et al., 2002; Kaufman et al., 2006; Wolfire et al., 2010; Neufeld & Wolfire, 2016). These models use underlying assumptions about thermal balance, gas chemistry, ionization balance and elemental abundances (Hollenbach & Tielens, 1997) to derive how the emission lines change as function of environment, using such parameters as gas temperature (T), gas density (n_H) and FUV radiation field strength (G_0). However, PAH emission features remain one avenue of measuring the physical conditions of PDR environments that is still in its infancy.

Recent efforts have uncovered some promising correlations between PAH emission features and PDR physical conditions. Based on three distinct PDR environments, Galliano et al. (2008) have empirically determined a quantitative relationship between the observed 6.2/11.2 PAH emission and the PAH ionization/recombination ratio or the PAH ionization parameter $\gamma = G_0 \, T^{0.5}/ \, n_e$ (Bakes & Tielens, 1994), where n_e is the electron density. Similarly, Boersma et al. (2015) found a relationship between the 6.2/11.2 emission ratio and the ionization parameter in the RN NGC 7023, where they fit spectra within the the RN with a collection of PAH species from the NASA Ames PAH IR Spectroscopic database (PAHdb, Bauschlicher et al., 2010; Boersma et al., 2014a; Bauschlicher et al., 2018) to calculate the ionization parameter. Additionally, it has been shown that the 7.7 μm PAH complex can be decomposed into four Gaussian components (Peeters et al., 2017). The ratio of two of these components, G7.8/G7.6, has been shown to have a linear relationship with G_0 over a wide range range of PDR environments (Stock & Peeters, 2017). Finally, through the use of the spectral fitting program, PAHTAT, an empirical relationship between the fraction of carbons contained within

very small grains (VSG) and G_0 has been established over a wide range of PDR environments (Pilleri et al., 2012).

Unfortunately each of the above relationships between PAH emission and environmental conditions have outstanding issues that must be resolved before they become more applicable to astronomy at large. For instance, the correlations between the 6.2/11.2 and γ determined by Galliano et al. (2008) and Boersma et al. (2015) disagree with each other by an order of magnitude in γ. Another important issue with the latter relationships is the individual parameters that make up γ (i.e. G_0, n_e, and T) cannot be isolated. Hence, this correlation alone does not provide enough information to properly characterize the PDR environment. Likewise, the Stock & Peeters (2017) relationship between G7.8/G7.6 and G_0 suffers from a bias in their data set towards higher values of G_0, with almost no representation from more quiescent regions. Moreover, due to a lack of FIR observations at a comparable resolution to the MIR observations, the Stock & Peeters (2017) relationship is currently forced to make simple assumptions to derive an estimate for G_0. The Pilleri et al. (2012) correlation between fraction of carbon locked in VSG and G_0 also has its limitations as this method is unable to properly measure the rising dust continuum found in spectral observations of H II regions and star-forming galaxies.

In this work, we aim to further investigate the relation between the PAH emission features and PDR physical conditions using matching apertures and spatial resolution for observations of the RN NGC 1333. We use archival *Spitzer* MIR spectral maps to characterize the PAH emission features and the relevant emission ratios. We obtain *SOFIA* FIR spectroscopic maps to measure three dominant PDR cooling lines: [O I] 63, 146 μm and [C II] 158 μm. We use archival *Herschel* FIR photometric observations to measure the FIR dust continuum. We derive maps of the PDR physical conditions in this region by comparing the cooling line observations along with FIR dust continuum observations with the relevant PDR models. We then relate the PAH emission to the derived PDR conditions to i) compare with the previously established empirical relationships of Galliano et al. (2008) and Stock & Peeters (2017), and, ii) develop new diagnostic tools between these quantities. In Section 4.2 we introduce NGC 1333. Section 4.3 presents to the observations and data reduction applied. Section 4.4 reviews the methodology used to measure the MIR and FIR emission involved in this study. We present our major results in terms of emission maps, correlations and PDR modelling in Section 4.5 and provide an interpretation of these results in Section 4.6. Finally, we give a summary of these findings in Section 4.7.

4.2   NGC 1333

NGC 1333 primarily refers to a large star-forming region located within the Perseus cloud complex (e.g. Liseau et al., 1988; Gutermuth et al., 2008; Walawender et al., 2008), however it originally referred to the RN at the core of this region (Figure 4.1). In this paper we will use the original nomenclature when referring to NGC 1333 (Strom et al., 1976). Astrometry of H_2O masers within the star–forming region of NGC 1333 has shown this complex is at a distance of 235 ± 18 pc from the Sun (Hirota et al., 2008). This RN is illuminated primarily by SVS 3, a B type star located at the center of the RN with the B6 star BD +30° 549 illuminating the nebulous region at 3.5′ to the northeast of SVS 3 (see Figures 4.1 and 4.2, Strom et al., 1976; Harvey et al., 1984). Young Owl et al. (2002) performed a study of the FIR cooling

lines of the PDR gas within the RN and found a far ultraviolet radiation field strength of 4800 times the interstellar average as well as gas density and temperature of 2×10^4 cm^{-3} and 690 K respectively.

There have been several notable MIR studies of NGC 1333 which are focused on PAH emission features. Bregman et al. (1993) used ground–based spectral imaging of the nebula around SVS 3 to show that the 3.3 and 11.2 μm bands are spatially distinct. In particular, the 3.3 μm emission peaks further from SVS 3 than the 11.2 μm emission and has a distribution comparable to a limb–brightened shell. Joblin et al. (1996a) showed how the relative intensity of the aliphatic 3.4 μm band to the 3.3 μm band increased significantly in the diffuse ISM surrounding the RN with respect pointings near SVS 3, suggesting that interstellar PAHs are highly methylated. Other ground–based MIR spectroscopic observations of NGC 1333 found the 8.6 μm band peaked at the location of SVS 3, while the 11.2 μm peaked 10″ south of SVS 3, suggesting this was evidence for the existence of ionized PAHs in the ISM (e.g. Joblin et al., 1996b; Sloan et al., 1999). Another ground–based MIR spectroscopic study, showed that the relative intensities of PAH emission features in the 8–13 μm range in NGC 1333 and another well–studied RN NGC 2023 are comparable (Roche et al., 1994). More recently, Stock et al. (2016) did a survey of MIR-bright regions using *Spitzer* IRS SL observations including both NGC 1333 and NGC 2023, where it was again found that correlations between the observed PAH emission features are similar in both sources (For a recent overview of the observed PAH emission features in NGC 2023 see Peeters et al., 2017). Moreover, using space–based ISOCAM spectral imaging Bregman & Temi (2005) observed a shift in the central wavelength of the 7.7 μm band in NGC 1333, where it shifted from 7.75 to 7.65 μm with decreasing distance to SVS 3. These authors found that the 11.2/7.7 ratio also decreases with proximity to the star which they relate to PAH ionization.

4.3 The Data

4.3.1 Observations

Spitzer

We present observations obtained with the Infrared Spectrograph (IRS Houck et al., 2004) on–board the *Spitzer* Space Telescope (Werner et al., 2004b). We retrieved Spitzer-IRS 5-14 μm short–low (SL) spectral mapping observations from the Spitzer archive (AORKEY 14587648, PI T. Bergin). These observations have a spectral resolution ranging from 60 to 128 over three orders of diffraction: SL1, SL2, and SL3. The SL mode has a pixel size of 1.8″, with a slit with of of 3.6″ and a slit length of 57″. The position of the IRS SL aperture used is shown in Figure 4.1.

SOFIA

The Field-Imaging Far-Infrared Line Spectrometer (FIFI-LS) on–board SOFIA is an integral field FIR spectrometer which includes two independent grating spectrometers with wavelength ranges from 51–210 μm and 115–200 μm respectively (Colditz et al., 2018; Fischer et al., 2018). Both channels have a 5×5 pixel projection onto the sky, with centers offset by 10″. The
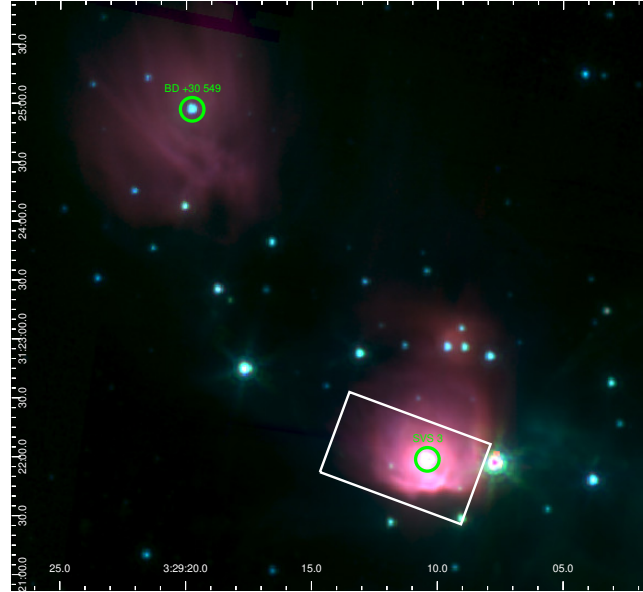
Figure 4.1: Spitzer IRAC Mosaic of NGC 1333 RN region (Gutermuth et al., 2008). IRAC 3.6, 4.5, and 8.0 μm are shown in blue, green and red respectively. Illuminating sources BD +30°549 and SVS 3 are indicated by green circles and the Spitzer IRS SL aperture is shown as a white rectangle.

short and long wavelength channels have a pixel size of $6'' \times 6''$ and $12'' \times 12''$ respectively which translates to a 0.5 and 1.0 arcminute–square FOV respectively. The 5×5 pixels are re-organized along a 25×1 line and subsequently dispersed into 16 pixels in the spectral dimension. Spectral resolution ranges from 600–2000 depending on the observed wavelength, which tends to be higher towards the longer wavelengths in both spectrometers.

We obtained FIFI-LS spectral observations of NGC 1333 for the following cooling lines: [O I] 63, 145 μm and [C II] 158 μm (PID: 05_0110, PI: E. Peeters). These data cubes have a PSF FWHM of $6.4''$, $14.6''$, and $15.9''$ respectively. Our observations are centered at (3:29:09.3, +31:21:47.2) (J2000) and are comprised of 4 parallel pointings with a stepsize of $30''$.

Herschel

We obtained FIR photometric observations taken with the Photodetector Array Camera and Spectrometer (PACS; Poglitsch et al., 2010) on–board the *Herschel* Space Observatory (Pilbratt et al., 2010) from the Herschel Science archive. PACS includes a dual–band photometer with an instantaneous FOV of $3.5' \times 1.75'$ that has bandpass combinations of either 60–85 μm and 125–210 μm (70/160 μm filter) or 85- 125 μm and 125–210 μm (100/160 μm filter). The 70 and 100 μm bands have a pixel scale of $3.2''$ while the 160 μm band have a pixel scale of $6.4''$. The absolute flux uncertainties for the 70, 100, 160 μm filters are $\pm$ 10, 10, and 20% respectively (Poglitsch et al., 2010).

These observations consist of imaging data of the Perseus Complex in the 70, 100 and 160 μm bands (PID: KPGT_pandre_1, OBS_ID: 1342190326 and 1342227103) created with
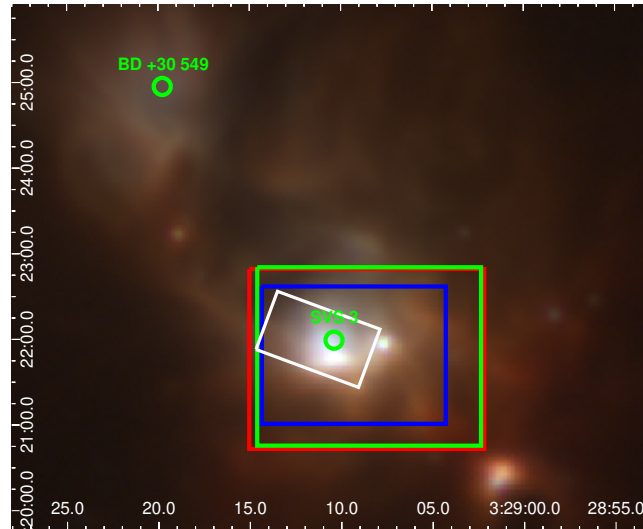
Figure 4.2: Hershel PACS Mosaic of NGC 1333 RNe Region. PACS 70, 100, and 160 μm are shown in blue, green and red respectively. All images are shown on a square root scale for clarity. Illuminating sources BD +30°549 and SVS 3 are indicated by green circles and the Spitzer IRS SL, FIFI–LS [O I] 63 μm, 146 μm and [C II] 158 μm apertures are shown as white, blue, green, and red rectangles respectively.

the JScanam task (Figure 4.2). Notably the 70 μm map was taken in the SPIRE/PACS parallel mode with a nominal scan velocity of 60″ s^{-1} corresponding to a PSF FWHM of 5.86″ × 12.16″. The 100 and 160 μm maps were taken in the PACS photo mode with a nominal scan speed of 20″ s^{-1} corresponding to PSF FWHMs of 6.89″ × 9.74″ and 11.31″ × 13.32″ respectively.

4.3.2   IRS Reduction

The SL raw data were processed with the S18.18 pipeline by the Spitzer Science Center. The resulting bcd data products were further processed using cubism (Smith et al., 2007a). We applied a *wavesamp* of 0.04–0.96 to exclude spurious data at the extremities of the SL slit and cubism's automatic bad pixel generation (σ_{TRIM} = 7 and Minbad-fraction = 0.5 and 0.75 for respectively global and record bad pixels). Remaining bad pixels were removed manually. The resulting SL2 and SL3 data cubes were regridded to the SL1 spatial aperture. We clip the original SL1 data cube to a 24 × 41 pixel aperture around the NGC 1333 SVS 3 where we find appreciable PAH emission.

We found order mismatches between the different orders of the SL module (SL1, SL2, and SL3). To remedy this issue, scaling factors of < 20% were applied to the SL2 and < 10% to the SL3 to scale these orders to the SL1 data, with the exception of some outlier pixels in the southwest and southeastern corners of the FOV considered which are masked out. We also masked out two prominent YSOs in the western edge of the considered FOV, as they exhibit strong silicate absorption and extinction. The SL1 and scaled SL2 data are combined into a single spectrum for each pixel.
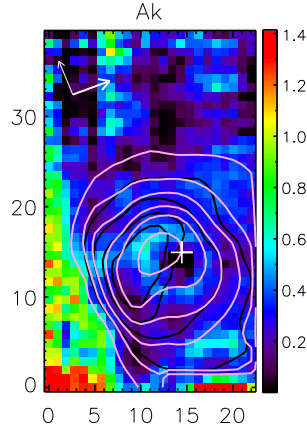
Figure 4.3: NGC 1333 extinction map in units of A_k. North and East are indicated by the thick and thin white arrows respectively in the upper left corner of the map. Contours of the 11.2 and 7.7 μm emission are shown respectively in black (1.0, 1.4, 1.8, and 2.2 $\times 10^{-5}$ W m^{-2} sr^{-1}) and pink (1.0, 2.0, 3.0, 4.5, 6.0 and 9.5 $\times 10^{-5}$ W m^{-2} sr^{-1}). The position of SVS 3 is indicated by a white cross.

4.4   Analysis

4.4.1   IRS SL Continuum and Extinction

To correct the spectra for extinction, we apply the 'modified Spoon method' (Stock et al., 2013, 2014, 2016). The Spoon method (Spoon et al., 2007) is an iterative fitting procedure that interpolates a power law continuum with anchor points at 5.5 and 14.5 μm of the form y = a x^k and then calculates the natural log of the ratio of this continuum at 9.8 μm to the observed flux at 9.8 μm. This is referred to as the optical depth of the 9.8 μm silicate absorption feature, $\tau_{9.8}$. In some cases the 14.5 μm is affected by silicate absorption, leading to an underestimation of $\tau_{9.8}$. The spectrum is then dereddened using the derived $\tau_{9.8}$ and the Spoon method is reapplied to get a new value for $\tau_{9.8}$. This process is reiterated until the anchor point at 14.5 μm does not change, at which point the final continuum at 9.8 μm is compared to the observed flux at 9.8 μm in the original spectrum. However, RN typically have a more linear shaped continua (i.e. Berné et al., 2007; Stock et al., 2016; Peeters et al., 2017). Thus we use a linear fit to the continua for this procedure as done by Stock et al. (2016), referred to as the modified Spoon method. We define a linear continuum of the form, y = a + 9.90 b, where b is the slope between anchor points of 5.5 and 13.9 μm and a is the flux at 5.5 μm minus b $\times$ 5.5 μm. This process is iterated upon until the observed flux at 9.8 μm and the continuum at 9.8 μm agree within 5%. We then deredden our spectral data by dividing by our final silicate extinction, A_k = 1.079 $\tau_{9.8}$ (Stock et al., 2013). We show a map of the extinction in Figure 4.3. We find that the extinction is very high ($A_k > 1$) in the southwestern edge of the map and the western edge near the two YSOs.

We make use of the spline decomposition method (e.g. Hony et al., 2001; Peeters et al., 2002; van Diedenhoven et al., 2004; Boersma et al., 2012; Stock et al., 2014; Shannon et al.,
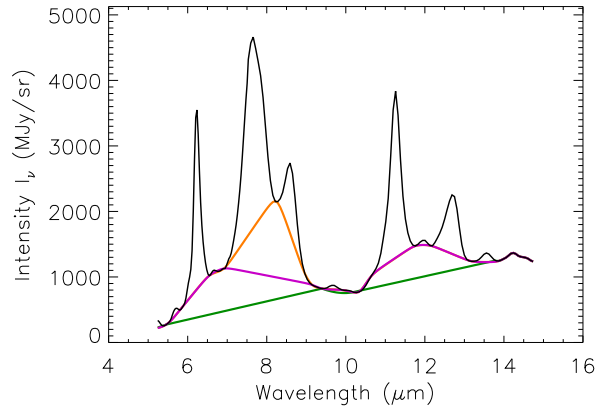
Figure 4.4: Typical SL spectrum from the RN within NGC 1333 are shown. The orange line traces the local spline continuum (LS), the magenta line traces the global spline continuum (GS), and the green line traces the underlying dust continuum (PL).

2015, 2016; Stock et al., 2016; Peeters et al., 2017) to fit the continuum in each of the spectra as local spline (LS), global spline (GS), and the underlying dust continuum (PL). An example of the typical spectrum and its continua is shown in Figure 4.4. For the LS continuum, we apply anchor points at 5.36, 5.46, 5.86, 6.58, 6.92, 8.28, 9.15, 9.40, 9.89, 10.14, 10.51, 10.76, 11.8,12.13, 13.18, and 13.49 μm. A spectral artefact arises beyond 14 μm, therefore, we exclude that wavelength range. The GS continuum uses all the same anchor points as the LS except for the removal of 8.28 μm point. The PL continuum is fit using straight lines between anchor points at 5.46 and 9.40 μm and 10.14 to 13.8 μm. We refer to the broad emission component in the 7–9 μm range between the LS and GS as the 8 μm bump. Likewise, we define the broad emission components between GS and the PL continua as the 5–10 μm and 10–15 μm plateaus. We use the term 'plat7 GS' to refer to the 5–10 μm plateau under the GS continuum and bounded below by the PL continuum. Likewise, we use the term 'plat11' to refer to the 10-14 μm plateau under the GS continuum and bounded below by the PL continuum. An example of the spectra observed within the RN of NGC 1333 is shown in Figure 4.4.

4.4.2 IRS SL Flux measurement

The fluxes of the major PAH bands are in general derived by integrating the continuum–subtracted spectra. In the case of the 6.2 and 11.2 μm bands, there is significant blending with the weaker 6.0 and 11.0 μm bands respectively. We fit Gaussians to the 6.0 and the (blue part of the) 6.2 μm simultaneously with λ (FWHM) of 6.027 (0.10) and 6.228 (0.18) μm respectively. We obtain these parameters by taking the average peak position for both Gaussians in pixels with sufficiently high 7.7 μm flux ($\geq 1.0 \times 10^{-5}$ W m^{-2} sr^{-1}). The peak positions are then fixed and the average FWHM over the same set of pixels is determined and subsequently fixed as well. We then subtract the flux of 6.0 μm Gaussian from the integrated 6.0 + 6.2 μm flux. The same treatment is used to disentangle the 11.0 and 11.2 μm bands where we use Gaussians λ (FWHM) of 10.979 (0.21) and 11.261 (0.258) μm respectively.

The 12.7 μm feature blends with the 12.3 μm H$_2$ line. Therefore, we use a decomposition

method similar to that used in previous studies (Stock et al., 2014, 2016) to isolate the 12.7 μm emission band. In short, the NGC 2023 12.7 μm profile at the PDR front from Peeters et al. (2017) is scaled to the 12.7 μm band between 12.4–12.8 μm. We subtract this scaled profile from the spectra and a Gaussian component is used to fit the 12.3 μm H$_2$ line. We then integrate each spectra from 12.15–13.1 μm and subsequently subtract the 12.3 μm H$_2$ Gaussian component to measure the 12.7 μm flux.

Following Peeters et al. (2017) and Stock & Peeters (2017), we decompose the PAH emission in the 7-9 μm range using four Gaussians, refered to as G7.6, G7.8, G8.2, and G8.6 components. We begin with a constrained fit to each component where the peak positions and FWHMs are allowed to vary within a 0.2 and 0.25 μm range respectively. The starting values for these parameters are set to the average RN values found by Stock & Peeters (2017, Table 1). Each Gaussian is then fixed to the average peak position found for the pixels where the 7.7 LS integrated flux is above a threshold value of 1.0×10^{-5} W m^{-2} sr^{-1}. The average FWHMs over the set of pixels is determined and fixed as well. The fitting procedure is run once more with the following fixed λ (FWHM) values for G7.6, G7.8, G8.2, and G8.6 μm: 7.58 (0.497), 7.90 (0.443), 8.25 (0.29), and 8.57 (0.41) μm respectively. For additional details and example fits of the above decompositions, see Stock et al. (2016); Stock & Peeters (2017); Peeters et al. (2017).

We estimate the signal–to–noise ratio of the PAH emission features as SNR = F/(2 × rms × $\sqrt{N}$ × $\Delta\lambda$) where F is the feature's flux (in W m^{-2} sr^{-1}), rms the rms noise, N the number of wavelength elements within the feature, and $\Delta\lambda$ is the size of each wavelength element in the spectrum. The rms noise is determined from featureless portions of the spectra between 9.3–9.5, 13.3–13.5, and 13.7–13.9 μm. For atomic and H$_2$ lines, the signal-to-noise is the ratio of the peak line flux to the underlying rms noise.

4.4.3   FIFI-LS Flux measurement

We make use of the SOSPEX spectral cube analysis software (Fadda & Chambers, 2018) to measure the FIR cooling line fluxes. We apply an atmospheric correction to all spectra. Specifically, for the [O I] 63 μm line, we apply an atmospheric correction equal to the median value of the atmospheric transmission, $\sim$ 0.56, due to the atmospheric transmission curve having a large drop towards the red end of this spectral range. For the [O I] 146 μm line, we apply an atmospheric correction equal the median value of the atmospheric transmission, over the wavelength range of the spectra, $\sim$ 0.8, due to a significant broad absorption band corresponding with the reference wavelength of the line. For the [C II] 158 μm line, we apply an atmospheric correction equal to the value of the atmospheric transmission at the reference wavelength of the line, $\sim$ 0.85, to avoid a broad absorption band at 157.5 μm (Lord, 1992).

We fit a straight line to anchor points to both ends of each spectral line to define the underlying continuum over the entire spectral cube with the boundary condition that the continuum must have positive values. The continuum for each pixel is then set to the median value within the surrounding pixels. To measure the line intensities, we use a Gaussian model for [O I] 63 μm and a Voigt model for [O I] 146 and [C II] 158 μm (Dario Fadda, private communication).

We convolve the [O I] 63 and 146 μm flux maps to match the larger PSF of the [C II] 158 μm map. For example, the width of the Gaussian kernel for the [O I] 63 μm to 158 μm
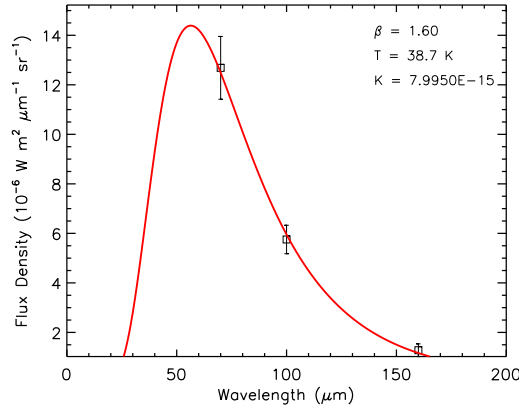
Figure 4.5: Example of the SED fitting procedure used to fit the PACS data. The data is shown as black squares and the modified blackbody fit is shown in red. The fit parameters for this pixel are given in the upper right.

convolution is $w = \sqrt{(15.9)^2 - (6.4)^2}$, where $6.4''$ and $15.9''$ are the [O I] 63 μm and 158 μm PSFs respectively (e.g. Houde & Vaillancourt, 2007). The FIR maps are then converted to units of W m^{-2} sr^{-1} and regridded to the largest spatial resampling size of $2''$ for the red spectrometer of FIFI–LS and clipped to the FOV of the [O I] 63 μm map allowing us to compare both data sets at a matching spatial resolution and FOVs.

4.4.4 FIR SED Fitting

We use PACS images at 70, 100, and 160 μm to measure the FIR dust continuum emission. We first convolve each of these images to the largest PSF in our data set, that of the [C II] 158 μm observation, using a 2D Gaussian kernel to account for the asymmetric PSFs of the PACS data. We extract a sub image of the convolved PACS maps equal to the FOV of the [C II] 158 μm map and regrid to the PACS 160 μm pixel scale. We then fit the data with a modified blackbody function of the form:

$$I(\lambda, T) = \frac{K}{\lambda^\beta} B(\lambda, T) \tag{4.1}$$

where K is a scaling parameter, β is the spectral index, T is the dust temperature and $B(\lambda,T)$ is the Planck function (e.g. Abergel et al., 2010; Berné & Tielens, 2012; Andrews et al., 2018). We use starting values of $\beta = 1.8$, T = 20 K and K = 1.0×10^{-15}. The obtained modified blackbody fits to the PACS data points agrees with the observations within the absolute flux uncertainties for each pixel (Figure 4.5). The FIR flux is determined by integrating the area under the fitted function for each pixel.

4.4.5　Matching Apertures

In order to compare the MIR IRS SL spectral maps with the FIR FIFI-LS and PACS maps, we convolved the maps to the lowest common resolution as was done in previous sections. As the [C II] 158 μm observation has the larger PSF of this dataset, all of the other maps are convolved to this spatial resolution. In our comparison of the MIR and FIR maps in Section 4.6.2, subimages of the FIR maps are extracted to match the IRS SL FOV, the smallest FOV within this dataset.

4.5　Results

4.5.1　IRS Results

In this section, we probe the relationships between the PAH emission features, the underlying plateaus, the H_2 emission, and the dust continuum emission obtained from the IRS SL data. We present our maps at the native pixel scale of the SL cube to explore this data at the highest resolution possible. Beyond this section, where we compare these maps with the FIR data in section 4.6.2, we convolve the IRS maps to the lowest common resolution as discussed in section 4.4.5.

SL Maps

In Figure 4.6, we show the spectral maps of the fluxes of the various spectral components within the IRS SL spectral cube of NGC 1333 including the PAH features, plateau components, and H_2 lines. We set the range of the colorbar to the minimum and maximum intensities shown in each map. Note that the black areas correspond to the pixels that have been masked for various reasons as described in section 4.3.2.

The major trends present within these maps are as follows. To first order, each of the major PAH features appears to share a similar concentric ovular morphology with intensities peaking just to the south of the stellar source, SVS 3, and gradually dropping with distance from this source. All PAH bands show deviations in symmetry from this concentric ovular morphology. In particular, the southern edge of the RN has a much steeper drop in emission relative to the other edges. This corresponds to regions with increased extinction.

The morphologies of the 6.2, 7.7, 8.6, and 11.0 μm PAH bands all show a similar condensed shape in their peak emission, which contrast with the much more elongated peak emission in the spatial distribution of the 11.2 μm PAH band, the 5–10 μm plateau, and the 10–15 μm plateau. The spatial distribution of the 8 μm bump and the 12.7 μm PAH band is a mix between these condensed and elongated morphologies. We also note the presence of a diffuse emission 'plateau' in the PAH morphologies moving westward from the center in a pixel range of approximately x = 10–20 and y = 3–5, which may be attributed to the two YSOs that are located at the western edge of these map. This emission plateau is much more readily apparent in the 11.2 μm band and the emission components that share a similar peak morphology. Continuum emission at 13.9 μm is much more spatially concentrated compared to the PAH emission with peaks almost on top of SVS 3. The H_2 S(3) 9.7 μm morphology deviates from the above trends: it is clearly concentrated to the southwest of SVS 3 with a peak co-spatial with the 10–15 μm

plateau and one near the YSO at the western edge of the map. We do not have $3\,\sigma$ detection of H_2 S(2) 12.3 μm line over much of the RN inhibiting any conclusive trends.

In Figure 4.7, we present the spectral maps of the four Gaussian components in the 7–9 μm decomposition. Upon first inspection, it is evident that the G7.6 and G8.6 μm components show a remarkably similar morphology which is comparable to that of the major PAH bands in the 7–9 μm range. The spatial distribution of the G7.8 and G8.2 μm components is very similar but is distinct from that of the G7.6 and G8.6 components with an elongated shape in their peak emission as well as both having an extended emission 'plateau' towards the western edge of the map. However, the peak intensity of the G7.8 μm component is more concentrated near the 7.7 μm emission peak while the G8.2 μm morphology better mimics that of the 11.2 μm band. These results support the conclusions of Peeters et al. (2017) in NGC 2023 regarding the behaviour of four Gaussian components.

In Figure 4.8, we compare the spatial distribution of PAH emission ratios that have previously been shown to be relevant in PDR studies (e.g. Galliano et al., 2008; Boersma et al., 2013; Stock & Peeters, 2017). First, we compare the ratio of each of the respective major PAH bands in the 6–9 μm to the 11.2 μm. In each of these ratio maps, we see a circular peak very close to the position of the star which are more concentrated and symmetric compared to the 7.7 μm emission. The overall morphology deviates from circular symmetry with enhanced emission towards the west, i.e. north of the 11.2 μm peak and in the direction of the YSO located at the bottom of the map. Furthermore, the spatial distribution of the 8.6/11.2 emission is more extended compared to the 6.2/11.2 and 7.7/11.2 morphology. We note two long filaments (vertical and diagonally in pixel coordinates respectively) in the 6.2/11.2 and 7.7/11.2 ratios that extends into the eastern reaches of these maps.

The spatial distribution of the G7.8/G7.6 ratio exhibits a minimum throughout much of the RN where we find the 6–9/11.2 ratios are highest. Only in the outskirts is an appreciable increase found in this ratio, with a maxima located in the eastern edge of this map where PAH emission is essentially at its lowest[1].

IRS Correlation Plots

Figure 4.9 presents a selection of observed intensity correlations found between PAH related emission components within the IRS SL data. To investigate the effects of extinction in our data, we group this data based into three regimes of extinction: low $A_K < 0.5$; intermediate $0.5 < A_k < 1$; and high $A_k > 1$. In general, all correlations show an improvement when we only account for the low extinction pixels, which fortunately coincides with the bulk of the RN.

We find very tight correlations between the 6.2 and 7.7 μm LS PAH bands (Figure 4.9 (a)). The 8.6 LS μm band also shows a strong correlation with both of these bands (Figure 4.9 (b) and (c)). Notably, we find that the 6.2, 7.7 GS and 8.6 GS μm bands show even tighter correlations with each other than the LS counterparts (Figure 4.9 (e), (f) and (g)). This is most evident for the correlations involving the 8.6 GS μm band. In addition, at high values, the 7.7 and 8.6 (both LS and GS) level off instead of linearly increase.

---

[1] We note that the 7–9 μm decomposition had generally much poorer fits to the 7.7 μm peak in these eastern pixels. This is attributed to a weak bump at $\sim 7.2\,\mu$m which the G7.6 μm component tries to fit resulting in an underestimation of the peak in the 7.7 μm band. Consequently we find that these pixels correspond to G7.8/G7.6 > 1.0, thus we consider these pixels to be unreliable in tracing this ratio.
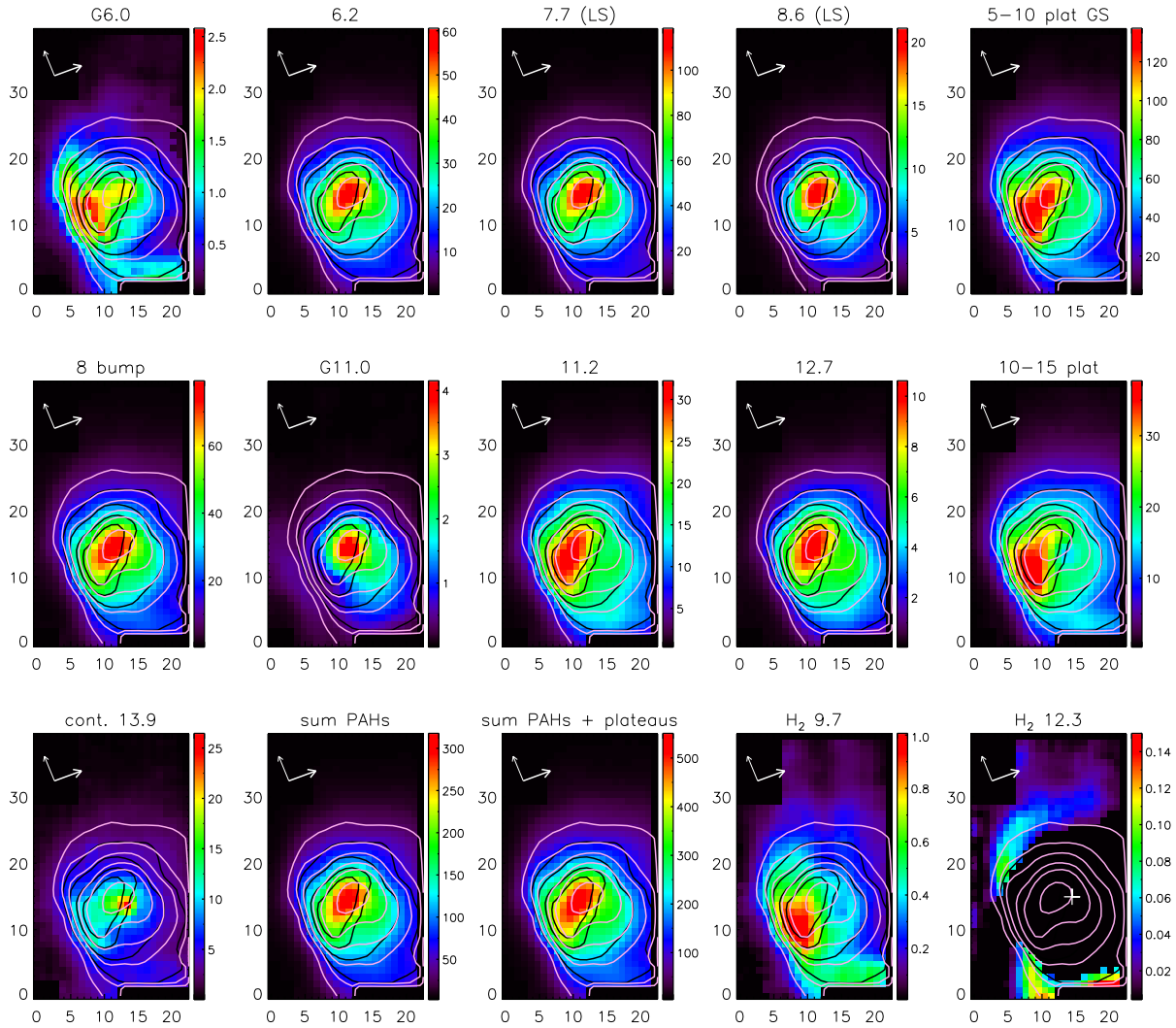
Figure 4.6: Spatial distribution of the emission features in the 5– 15 μm IRS SL data within the NGC 1333 SVS 3 region. PAH band and continuum intensities are given in units of 10^{-6} W m^{-2} sr^{-1} and 100 MJy sr^{-1} respectively. Contours of the 11.2 and 7.7 μm emission are shown respectively in black (1.0, 1.4, 1.8, and 2.2 × 10^{-5} W m^{-2} sr^{-1}) and pink (1.0, 2.0, 3.0, 4.5, 6.0 and 9.5 × 10^{-5} W m^{-2} sr^{-1}). North and East are indicated by the thick and thin white arrows respectively in the upper left corner of each map.The position of SVS 3 is indicated by a white cross in the H$_2$ S(2) 12.3 μm map.
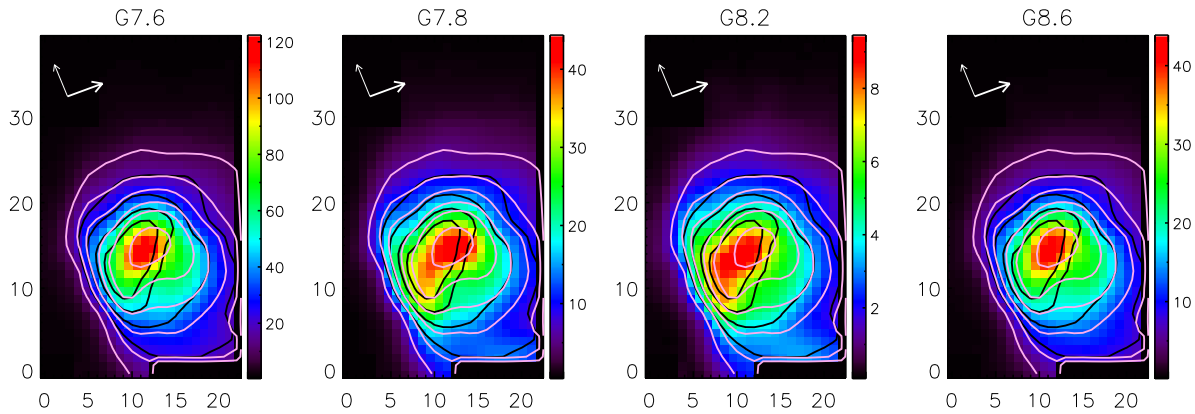
Figure 4.7: Spatial distribution of the Gaussian Components in the 7–9 μm range of the IRS SL data within the NGC 1333 SVS 3 region. Color bars of band intensities are given in units of 10^6 W m^{-2} sr^{-1}. Contours of the 11.2 and 7.7 μm emission are shown respectively in black (1.0, 1.4, 1.8, and 2.2×10^{-5} W m^{-2} sr^{-1}) and pink (1.0, 2.0, 3.0, 4.5, 6.0 and 9.5×10^{-5} W m^{-2} sr^{-1}). North and East are indicated by the thick and thin white arrows respectively in the upper left corner of each map.
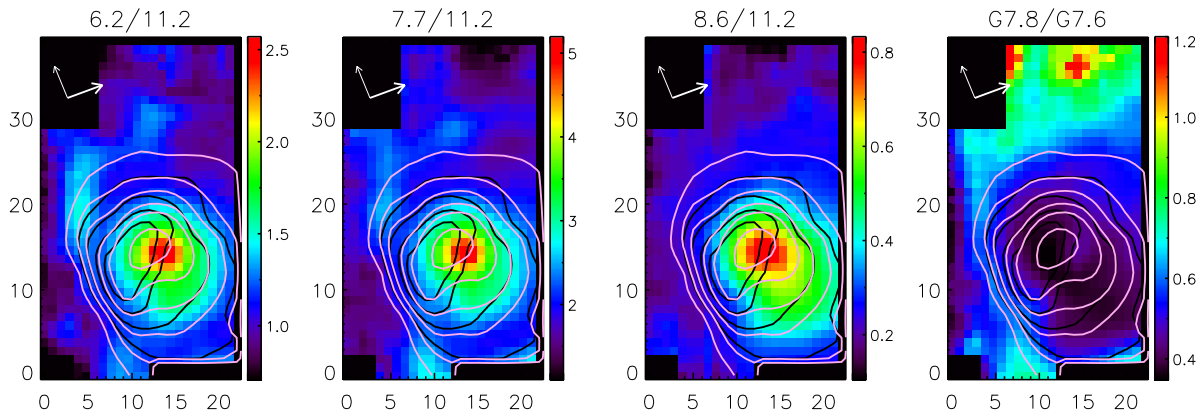
Figure 4.8: Spatial distribution of ratios of major PAH bands and Gaussian Components in the 7–9 μm range of the IRS SL data within the NGC 1333 SVS 3 region. Contours of the 11.2 and 7.7 μm emission are shown respectively in black (1.0, 1.4, 1.8, and 2.2×10^{-5} W m^{-2} sr^{-1}) and pink (1.0, 2.0, 3.0, 4.5, 6.0 and 9.5×10^{-5} W m^{-2} sr^{-1}). North and East are indicated by the thick and thin white arrows respectively in the upper left corner of each map.

The G7.6 and G8.6 μm components have the best correlation of all features (Figure 4.9 (i)), while the 6.2 μm band and the G8.6 μm also show very tight correlations (Figure 4.9 (k)). In contrast, the G7.8 and G8.2 μm only correlate modestly (Figure 4.9 (j)).

The 12.7 μm band correlates strongest with the 8.6 LS μm band (Figure 4.9 (o)). However, instead of exhibiting a linear correlation, there are two regimes present. At low 8.6/11.2 values, a steep increase in the 12.7/11.2 is seen while at intermediate and high 8.6/11.2 values, the corresponding increase in 12.7/11.2 is more moderate. A similar behavior is seen in the relation of the 12.7 μm band with the 6.2, 7.7, and G7.6 μm bands overall though they exhibit enhanced "scatter" which seem to occur in a similar pattern (Figure 4.9 (m), (n), and (p)). The 11.0 μm band shows a bifurcated pattern for all correlations considered. One of the branches is entirely composed of spectra with moderate to high extinction while the other branch is dominated by regions with low extinction. Given the uncertainty related to extinction measurements, we restrict ourselves to low extinction areas. The 11.0 μm band exhibit strong correlations with the 6.2, 7.7, and 8.6 μm bands (Figure 4.9 (r), (s) and (t)). Its behaviour with the 12.7 μm band shows a similar pattern as that of the 12.7 versus 8.6 μm band: for the lower range of 12.7/11.2 values, little to no variation is seen in the 11.0/11.2 and only for the upper range of 12.7/11.2 values, a clear correlation is observed (Figure 4.9 (q)).

The 5–10 μm plateau does not correlate well with the 6.2 and 7.7 μm bands, primarily because of a bi–linear trend that seems to stem from this plateau. This bi–linear trend is also evident between the 6.2 and G8.2 μm correlation with both branches containing pixels with low extinction.

4.5.2   FIFI–LS Maps

In Figure 4.10, we show the FIFI-LS spectral maps of the three FIR cooling line fluxes. Each of these maps is convolved to the PSF of the [C II] 158 μm observations and regridded to the PACS 160 μm map grid (see Section 4.4.3). In each case, these emission lines show a simple concentric morphology with emission peaking near the illuminating source. However, the [O I] 146 μm peak intensity is offset from the source position (to the southeast) as is the 7.7 μm PAH peak emission, whereas [O I] 63 and [C II] 158 μm peaks are nearly co–spatial with the star. The [C II] emission is slightly displaced from the central star to the northeast and exhibits significant emission to the north and north east of the star. Another notable difference is the [O I] 63 μm is significantly more centrally concentrated relative to the other FIR cooling lines which cannot be discounted because this map has been convolved to match the [C II] 158 μm resolution.

4.5.3   PACS Maps

In Figure 4.2, we show the PACS 70, 100, 160 μm images in blue, green and red respectively. These maps shows a very similar concentric morphology within the RN with peak emission found to south of SVS 3 in each case. They also show emission extending to the west of SVS 3 with a secondary peak corresponding to the YSO IRAS 03260 +3111E. In Figure 4.11, we show the FIR dust continuum emission map derived from the PACS images as detailed in section 4.4.4. This map is essentially identical in spatial morphology to the individual PACS maps.
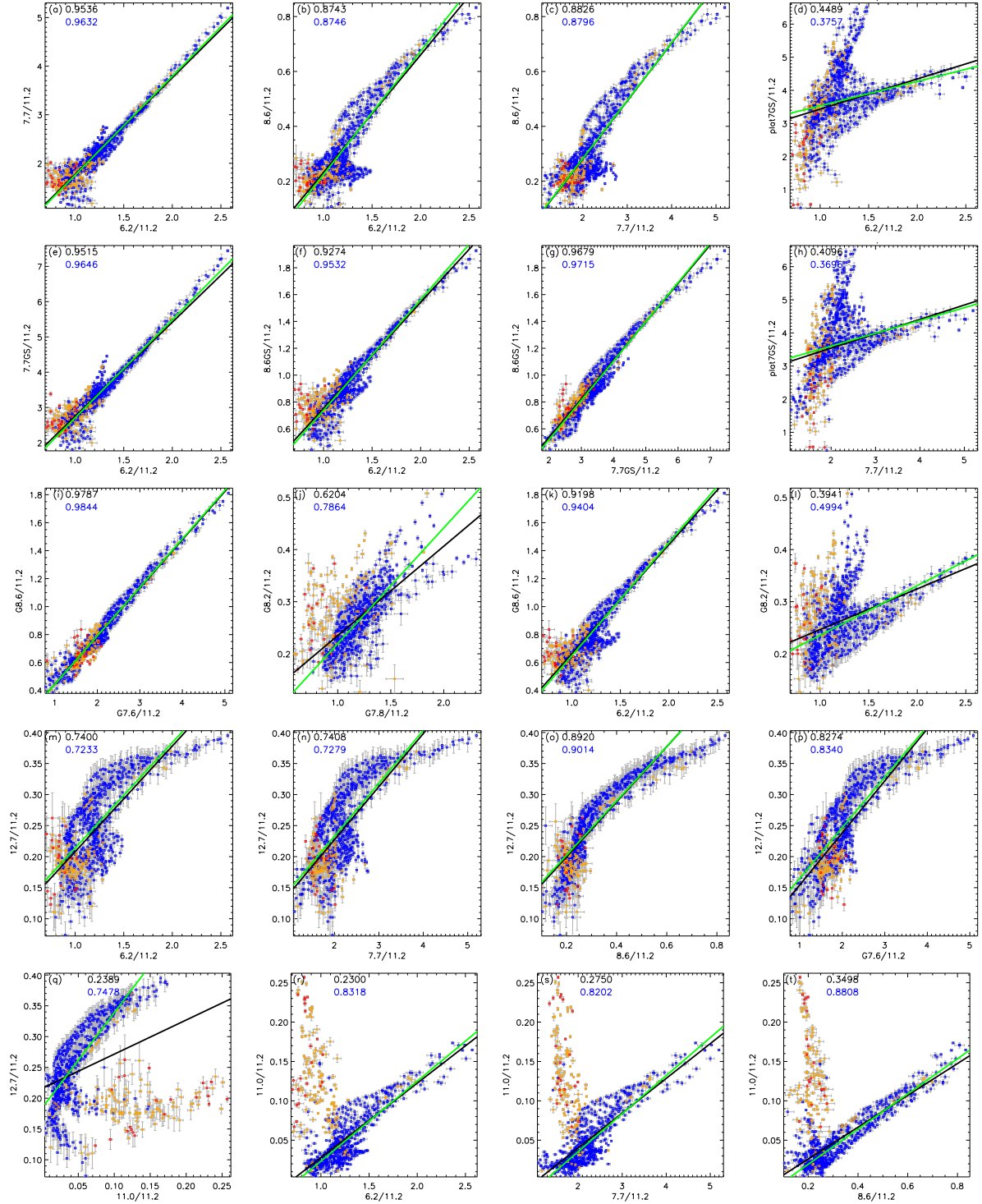
Figure 4.9: Correlation plots between PAH features in NGC 1333 IRS SL. The data is sorted into three separate regimes based on the degree of extinction (Section 4.4.1): points with $A_k < 0.5$ are given as blue squares, points with $0.5 < A_k < 1$ are shown as orange squares, and points with $A_k > 1$ are shown as red squares. Correlation coefficients are given in the top left of each panel for the entire map in black and for only the pixels with $A_k < 0.5$ in blue. Linear fits are shown for all pixels in black and for only the pixels with $A_k < 0.5$ in green.
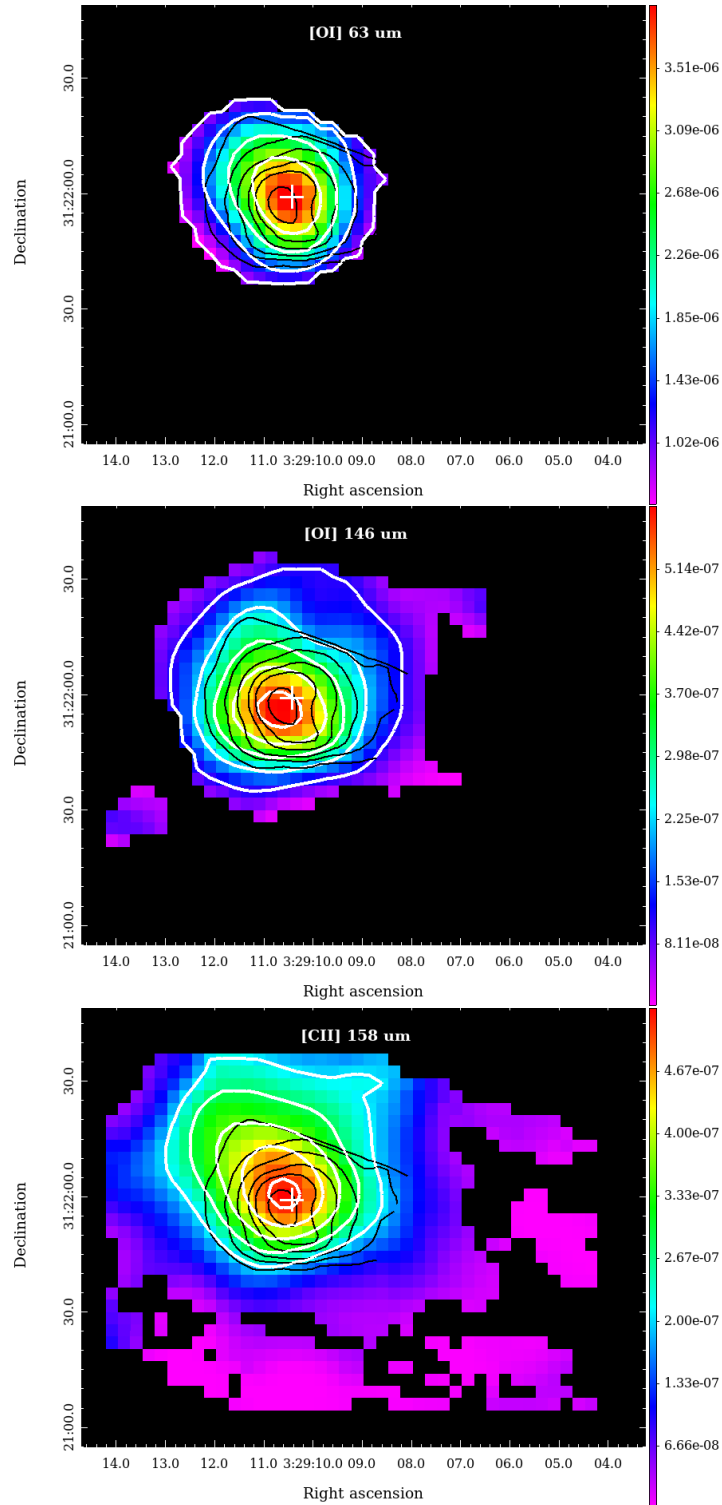
Figure 4.10: FIR Cooling line fluxes derived from SOSPEX. *Top* The [O I] 63 μm line fluxes with white contours of 0.60, 1.43, 2.26, 3.09, 3.92 $\times$ 10^6 W m^{-2} sr^{-1}. *Middle* The [O I] 146 μm line fluxes with white contours of 1.06, 2.17, 3.27, 4.38, 5.48 $\times$ 0^7 W m^{-2} sr^{-1}. *Bottom* The [C II] 158 μm line fluxes with white contours of 2.05, 2.81, 3.59, 4.35, 5.12 $\times$ 10^7 W m^{-2} sr^{-1}. Contours of the PAH 7.7 μm flux are shown in black at 1.0, 2.0, 3.0, 4.5, 6.0 and 9.5 $\times$ 10^{-5} W m^{-2} sr^{-1}. The position of SVS 3 is shown as a white cross. Pixels below the 3 σ noise level of each respective map are shown in black.
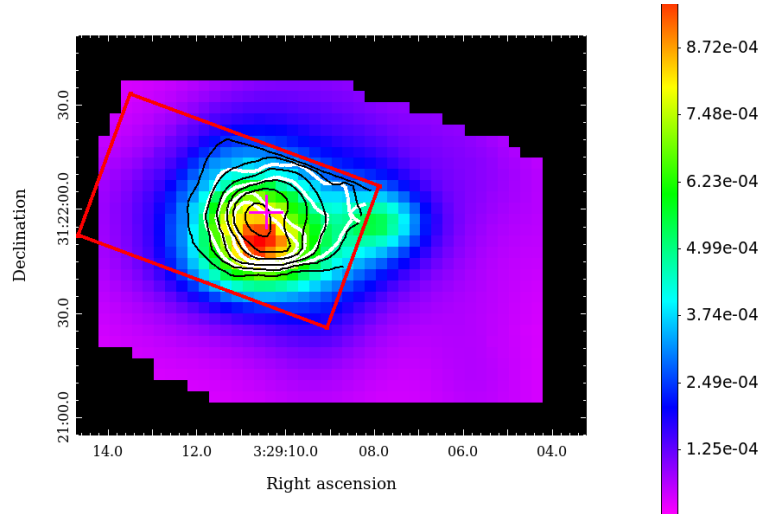
Figure 4.11: The FIR dust continuum in units of W m^{-2} sr^{-1}. The IRS SL aperture is shown as a red rectangle. Contours of the 11.2 and 7.7 μm emission are shown respectively in white (1.0, 1.4, 1.8, and 2.2 $\times$ 10^{-5} W m^{-2} sr^{-1}) and black (1.0, 2.0, 3.0, 4.5, 6.0 and 9.5 $\times$ 10^{-5} W m^{-2} sr^{-1}). The position of SVS 3 is shown as a magenta cross. North is up and east is to the left. Pixels below the 3 σ noise level are shown in black.

4.5.4 PDR Modelling

We make a simple estimate for the FUV radiation field strength (between 6 and 13.6 eV) using the FIR dust continuum emission:

$$G_0 \simeq \frac{1}{2} \frac{I_{\text{FIR}}}{1.3 \times 10^{-7}} \qquad (4.2)$$

where we assume a face–on PDR morphology (Hollenbach & Tielens, 1997) and take G_0 in units of the Habing field (1.3 $\times$ 10^{-7} W m^{-2} sr^{-1}; Habing, 1968). We use i) this FIR dust continuum derived G_0 along with the FIR cooling lines [O I] 63 and [C II] 158 μm and ii) the [O I] 63/ [C II] 158 PDR model as a function of gas density and FUV radiation field strength from the Photo Dissociation Region Toolbox (PDRT) software (Kaufman et al., 2006; Pound & Wolfire, 2008) to determine the gas density and temperature. Several of the chemical and thermal processes in the model have been updated with recent rates. In particular the photo-dissociation and photo-ionization rates of Heays et al. (2017) are used and the collisional excitation rates of [O I] from Lique et al. (2018) and (Lique private communication). These model grids have resolution elements of 0.125 in log G_0 and n_H. These grids cover a range of -3.3–3.7 in log G_0 and a range of 1–7 cm^{-3} in log n_H. We observe the median [O I] 146/63 ratio in pixels where [O I] 63 μm line has a 3 σ detection to be 0.154, higher than 0.1 which Ossenkopf et al. (2015) suggest is a sign for self-shielding. To account for the self–shielding of [O I] 63 μm, we multiply our [O I] 63 μm observations by a factor of 2 (e.g. Schneider et al., 2018). We compare the observed 2 $\times$[O I] 63/ [C II] 158 ratio and G_0 in each pixel with the [O I] 63/ [C II] 158 model grid in G_0 and n_H to predict the gas density, n_H, based on where the observed quantities intersect the grid. We use the derived densities along with the G_0 values to derive a gas temperature by comparing our predicted values with a model grid for gas temperature, T, as a function

of gas density and FUV radiation field strength. We then convert the gas density to electron density using the assumption that all free electrons result from the photoionization of carbon and all gas–phase carbon is ionized (e.g. Galliano et al., 2008), $n_e \simeq$ (C/H) $n_H \simeq 1.6 \times 10^{-4}\, n_H$, where 1.6×10^{-4} is the interstellar gas–phase carbon abundance (Sofia et al., 2004). From this, we derive the PAH ionization parameter ($\gamma = G_0\, T^{0.5}\, /\, n_e$ Bakes & Tielens, 1994).

We find that the derived G_0, n_H, and T are of the same order of magnitude as the results of the FIR analysis performed by Young Owl et al. (2002) for this region: 10^3, 10^4 cm^{-2}, and 10^2 K respectively. Slight discrepancies in the absolute values found between both studies may be attributed to a difference in spatial resolution. Indeed, Young Owl et al. (2002) consider a single pointing for each line with beam sizes $> 40''$ whereas our maps have been convolved to the [C II] 158 μm PSF of 15.9$''$ and resampled to the PACS 160 μm grid with a pixel scale of 3.2. Thus we are effectively probing a spatial resolution of approximately an order of magnitude higher.

The resulting maps of the PDR conditions are shown in Figure 4.12. Except for the G_0 map, these maps are cut by the [O I] 63 μm 3 σ detection limit. The G_0 and T maps show a high degree of spherical symmetry emanating from their nearly co–spatial peaks. Likewise, the morphology of the PAH ionization parameter is similar to that of G_0. Oddly however, each of these three parameters peak to the south of SVS 3 where they almost overlap with the PAH 11.2 μm emission peak. In contrast, the gas density map shows very little variation, with a large plateau at $\sim 2.3 \times 10^4$ cm^{-3} over much of the nebula and a substantial rise towards the southern edge of the map beyond the PDR front as traced by H$_2$ S(3) 9.7 μm (Figure 4.6).

4.6   Discussion

4.6.1   PAH Relative Intensities

While we report significant correlations between various PAH features, clear deviations from these tight correlations and anomalous groups of pixels exist within our FOV (see Figure 4.9) that deserve a more in–depth investigation. We have illustrated that in particular for the 11.0 μm band, the degree of extinction introduces such an anomalous group of pixels. Clearly, due to its weakness and being located in the wing of the silicate absorption feature, the 11.0 μm band is more affected by extinction (correction) in comparison to the major PAH bands. However, significant scatter remains when we only account for the low extinction regime. Here we apply other weighting schemes in order to better characterize these discrepancies. In Figure 4.13, we show a selection of the correlation plots shown in Figure 4.9 where we apply a color to each pixel based on the PAH 7.7 LS μm flux (top two rows) and the 8.6/11.2 ratio (bottom two rows). We use the same color scale as shown for the 7.7 μm map in Figure 4.6 and for the 8.6/11.2 μm map in Figure 4.8 for easy comparison.

In panels (a), (b) and (c) of Figure 4.13, we compare the correlations between the major PAH bands in the 6–9 μm range. When only considering positions where the 7.7 μm flux is $> 10^{-5}$ W m^{-2} sr^{-1}, the correlations are tighter than in the case of the low silicate regime of Figure 4.9. This cut-off value for 7.7 μm flux distinguishes between the nebula itself and the outskirts in the FOV which correspond to the more diffuse ISM (see Fig 4.6). Thus, these bands are much better correlated in irradiated PDRs than in the diffuse ISM. In addition, when
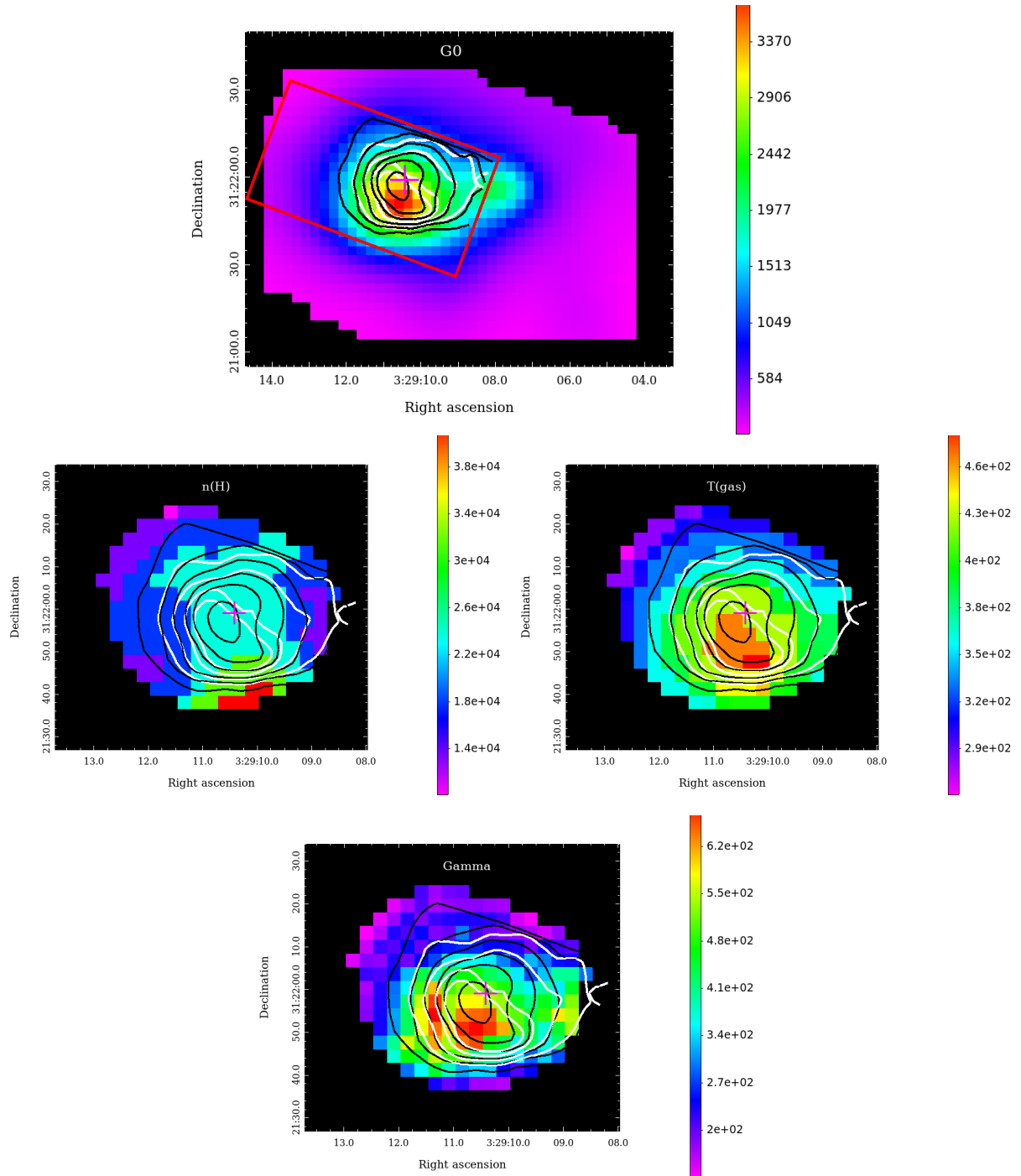
Figure 4.12: The environmental conditions in NGC 1333 derived from FIR data and PDR models. *Top* The FUV radiation field strength, G_0, in units of the Habing field. The IRS SL aperture is shown as a red rectangle. *Center left* The gas density, n_H, in units of cm^{-3}. *Center right* The gas temperature, T, in units of K. *Bottom* The ionization parameter, $\gamma = G_0\, T^{0.5}\, /\, n_e$. Contours of the 11.2 and 7.7 μm emission are shown respectively in black (1.0, 1.4, 1.8, and 2.2 × 10^{-5} W m^{-2} sr^{-1}) and white (1.0, 2.0, 3.0, 4.5, 6.0 and 9.5 × 10^{-5} W m^{-2} sr^{-1}). Pixels where [O I] 63 μm emission line has a SNR < 3 are shown in black for center and bottom panels. The position of SVS 3 is indicated by a magenta cross in each map. North is up and east is to the left.
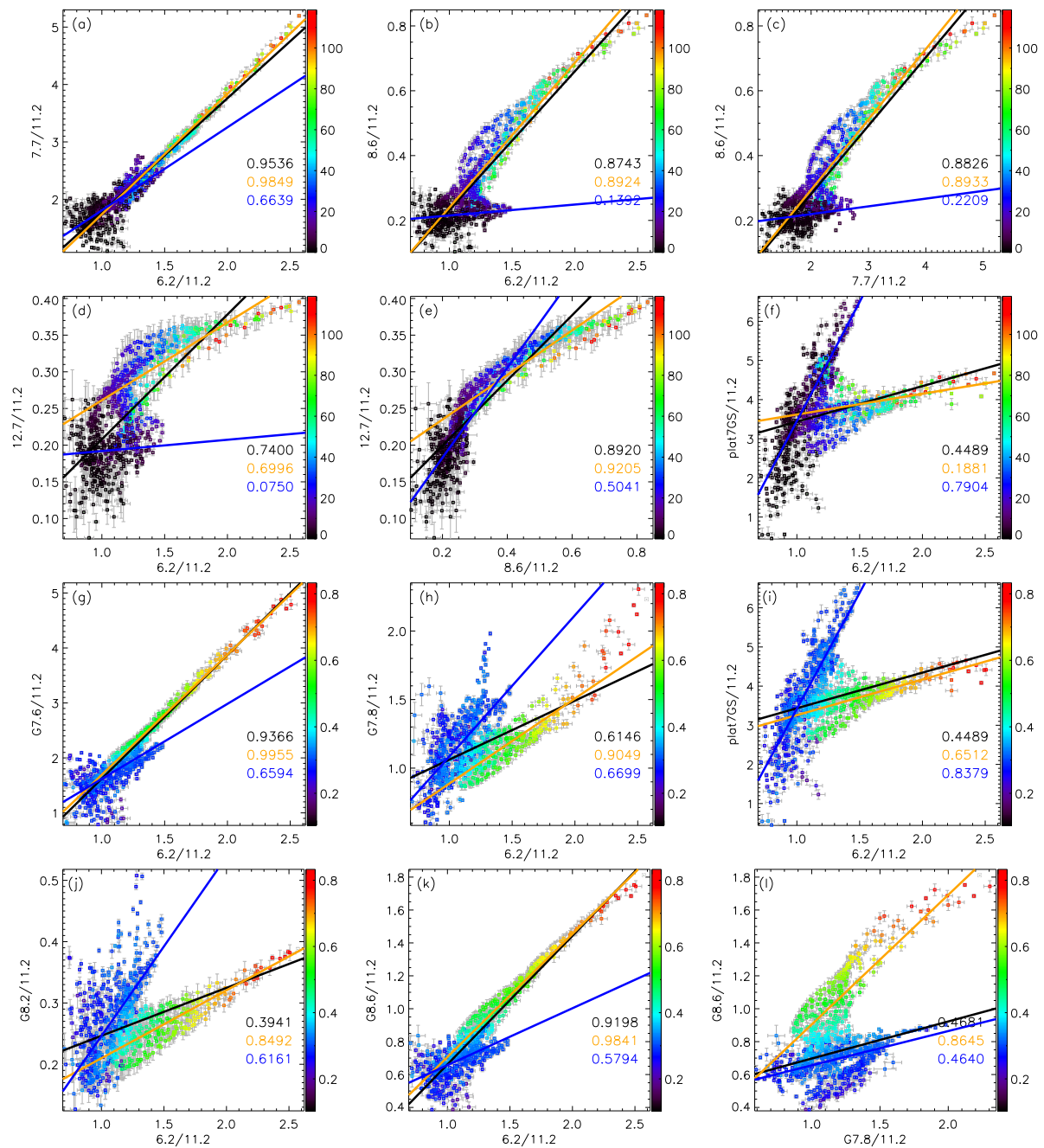
Figure 4.13: Correlation plots between PAH features in NGC 1333. The data is color–coded to the PAH 7.7 LS μm flux with the values given in units of 10^{-6} W m^{-2} sr^{-1} (top two rows) and to the PAH 8.6 LS/11.2 ratio (bottom two rows). Correlation coefficients are given in the bottom right of each panel for the entire map (black) and for the pixels where the 7.7 μm LS flux > 10^{-5} W m^{-2} sr^{-1} (orange) and $\leq 10^{-5}$ W m^{-2} sr^{-1} (blue, top two rows) and for the pixels where the 8.6/11.2 ratio > 0.3 (orange) and $\leq$ 0.3 (blue, bottom two rows). Linear fits are shown in the same respective colors as for the regimes defined for the correlation coefficients.

the 8.6 μm band is considered, a stumpier second correlation is observed for locations where the 7.7 μm flux is $\leq 10^{-5}$ W m^{-2} sr^{-1}, i.e. the diffuse ISM. This second branch exhibits little change in the 8.6 μm band intensity while a larger change is seen in the 6.2 or 7.7 μm band intensity. Another notable anomaly is the 'arc' found in the correlation of the 6.2 versus 8.6 μm bands and the 7.7 versus 8.6 μm bands while it is absent in the correlation of the 6.2 versus 7.7 μm bands. The majority of the pixels in the arc exhibit a low degree of extinction excluding extinction as its origin. However, the pixels in the arc are located in the western edge of the FOV and thus the PAH emission may be affected by the nearby YSO. Similarly, it is only when considering the 8.6 μm band that at high ratio values the data levels off. We note that the arc disappears and the degree of levelling off decreases significantly when considering the G8.6 component instead of the 8.6 μm band (which were obtained with different underlying continua).

Concerning correlations with the 12.7 μm band (Figure 4.13 (d) and (e)), two major regimes are present characterized by high and low 12.7/11.2 (i.e. > 0.25 or < 0.25 respectively). This boundary corresponds approximately to the region between the two lowest contours in our 7.7 μm map (Figure 4.6), representing the transition from the nebula to the diffuse ISM. In the lower flux regimes, there is significant scatter with a much wider range in 12.7/11.2 compared those found in the other ionic bands normalized to 11.2 μm band. In particular, the 6.2 or 7.7 versus 12.7 relation exhibit two separate arcs in this low 12.7/11.2 regime that seem to make up opposite halves of a circular trend. Based on the 7.7 μm band intensity, the right arc is largely located in the transition region between the nebula and the diffuse ISM, the left arc is relegated to the diffuse emission outside of the PDR while the nebula represents the high 12.7/11.2 regime.

A similar behaviour with pixel location is seen for the strong bi-linear trend observed between the 6.2 μm band and 5–10 μm plateau (Figure 4.13 (f)). The branch representing a large change in the plateau emission relative to the 11.2 μm band has a high correlation coefficient and low ionization degree (as traced by 8.6/11.2 intensity ratio in Figure 4.13 (i)). This branch arises from the diffuse ISM. In contrast, the second branch exhibiting a smaller range in plateau intensity normalized to the 11.2 μm band represents the nebula where a medium to high degree of ionization is found. Bi-linear trends arising from different regions are also found between the 6.2 μm band and the four Gaussian components (Figure 4.13 (g), (h), (j), (k) and (l)), in particular for the G8.2 and G7.8 components. An 8.6/11.2 value of about 0.3 distinguishes the nebula from the diffuse ISM and the transition between both (Figure 4.8). Using this boundary condition, one branch arises from the nebula and exhibits a strong correlation while the other branch arises from the diffuse ISM and the transition region between the nebula and the diffuse ISM and shows more scatter. The diffuse ISM branch is very pronounced and distinct for the G8.2 component and subsequently the G7.8 component while for the G7.6 and G8.6 this branch is highly blended with the nebula branch and shows much less variation. In addition, the G7.8 and G8.2 components normalized to the 11.2 μm band show a stronger increase for a given increase in 6.2/11.2 for the diffuse ISM branch than the branch arising in the nebula while the opposite holds for the G7.6 and G8.6 components.

Finally, we note the existence of a third branch for relations between the G7.8 component and the G7.6 component, G8.6 component, or 8 μm bump (Figure 4.13 (l) shows the second correlation). Specifically, the relationship between these set of bands is different in the nebula, the diffuse ISM as well as the transition region between both with the third brand representing

the latter. Moreover, the third branch is parallel with the branch representing the nebula. The common factors in this set of relations is the G7.8 component and the almost 'identical' characteristics of the G7.6 and G8.6 components (cf. these bands exhibit the strongest correlation between any PAH bands). As the relation of the G7.8 with the G8.2 component exhibits a single linear correlations, albeit with significant scatter, and the G8.2 component exhibit bi-linear trends with the G7.6 and G8.6 components, the existence of the third branch confirms that the G7.8 and G8.2, as defined here, do not completely arise from the same PAH population.

Multi-linear trends in the relation between various PAH ratios have already been reported in the literature. Specifically, Stock et al. (2016) demonstrated that correlations between the 12.7 and 7.7 μm bands, normalized to the 11.2 μm band, showed different linear trends with respect to the different physical environments they probed from most quiescent environments to harsher environments associated with H II regions with PDRs characteristic of RNe in between. Using the same sample, Stock & Peeters (2017) reported a bifurcation in the correlations between the G7–9 μm Gaussian components involving G7.8 and G8.2 μm, normalized to the 11.2 μm band intensity. They associate the G7.8 μm with diffuse regions and the G7.6 μm with irradiated PDRs, consistent with the results reported above. The presented analysis here and by these authors thus clearly demonstrates that the relative behaviour of the PAH bands (i.e. how the band intensities normalized to the 11.2 μm band intensity of different PAH bands relate to each other) depends on the type of environment in which they reside, the diffuse ISM, the irradiated PDR or the transition region between these environments. Note that we detect a discrete set of trends or branches (e.g. one, two or three) and not a continuous distribution.

This implies that (some of) the PAH bands arise from multiple PAH subpopulations or from multiple grand-PAHs (Andrews et al., 2015) that i) each have distinct relative PAH intrinsic intensities, and ii) have different relative abundances in these different environments. For instance, the fact that we only see one branch or linear relationship between the G7.6 and G8.6 components and between the 6.2 and 7.7 μm bands indicates that both sets of bands arises from either a single PAH subpopulations or from PAH subpopulations which are co-located across the entire FOV (i.e. for all three environments: the diffuse ISM, the irradiated PDR and the transition region). In contrast, when we observe two linear relationships or branches for a set of PAH bands, e.g. the 6.2 and the 8.6 μm band, indicates these bands arise from at least two distinct subpopulations that have relative abundances dependent on the environment in which they reside. As a consequence, this then indicates that, similar to the 7.7 μm band, the 6.2 μm band arises from at least two distinct PAH subpopulations. The latter was already implied by the fact that the 6.2 μm band correlates very strongly with the 7.7 μm band which has been found to arise from at least two subpopulations (Peeters et al., 2017, this chapter). In this chapter, we thus present support of this hypothesis by the unique behaviour of the PAH emission in the diffuse ISM versus the nebula.

We have found the PAH emission bands and their associated ratios have a dependence on their environment qualitatively. Probing the relationships between PAH emission ratios and the physical conditions in the different regions found within this source quantitatively could provide insight into a novel way to use PAH emission as PDR diagnostics. We further explore this in Section 4.6.2.
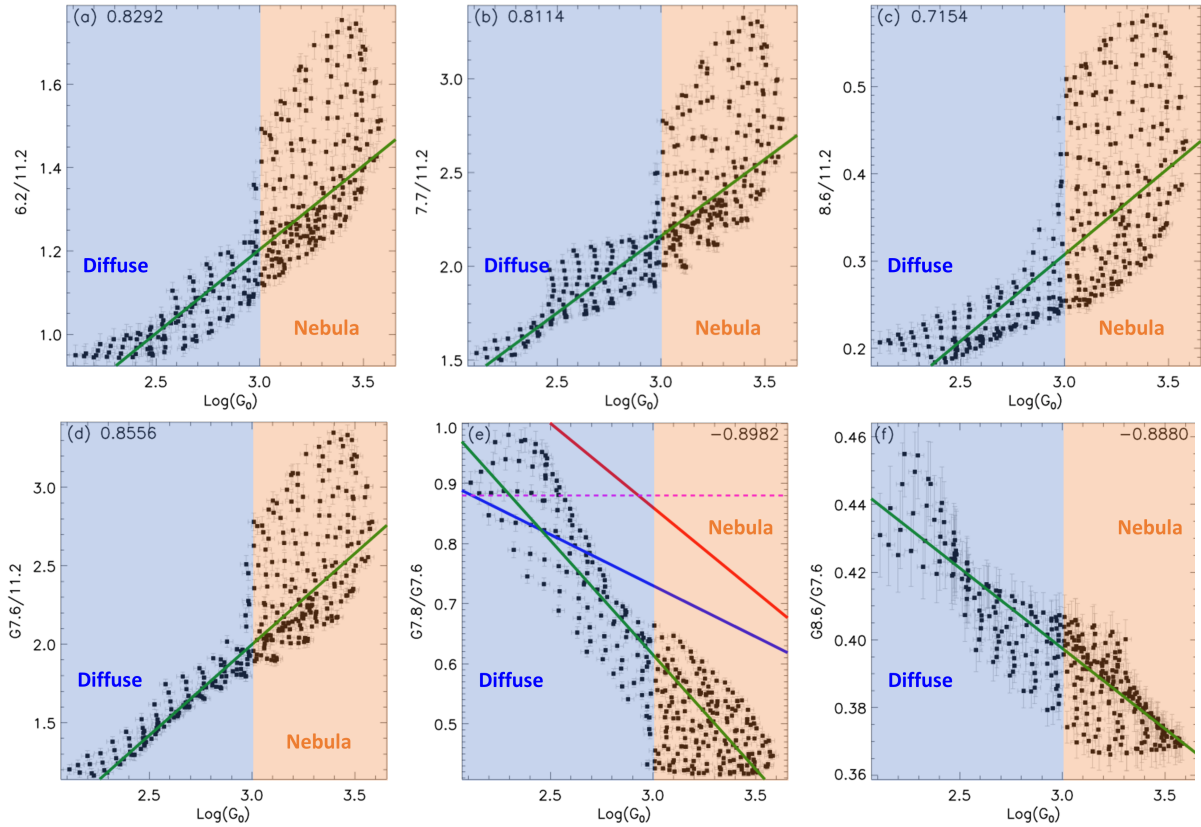
Figure 4.14: Correlation between the strength of the FUV radiation field, G_0, and PAH emission ratios in NGC 1333. Correlation coefficients are given in the upper right or upper left of each plot. Linear fits between $\log(G_0)$ and each PAH ratio is shown by a green line. We divide each plot into two regimes based on the relative strength of the FUV radiation field: $\log(G_0) \geq 3$ in orange corresponds to the irradiated RNe and $\log(G_0) \leq 3$ in blue corresponds to the diffuse ISM. In the bottom center panel, we show linear fits of Stock & Peeters (2017), with (blue) and without (red) inclusion of low G_0 regions. In this panel, the maximum G7.8/G7.6 ratio of 0.88 found in the diffuse outskirts of W49A by Stock & Peeters (2017) is shown as a magenta horizontal dashed line.
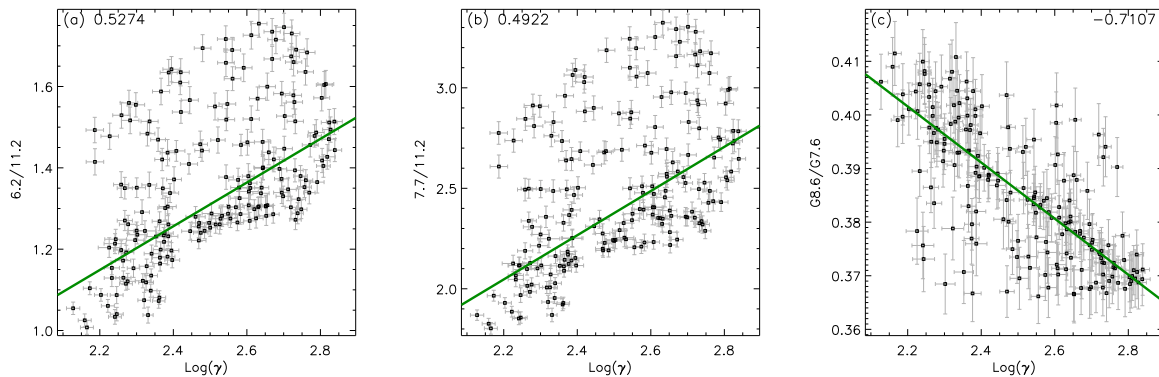
Figure 4.15: Relationship between the PAH ionization parameter, γ, and PAH emission ratios in NGC 1333. The correlation coefficient are given in the upper right or upper left of each plot. Linear fits between $\log(\gamma)$ and each PAH ratio are shown as a green line.

4.6.2   PAHs as PDR Diagnostics

In Figure 4.14, we compare the strength of the FUV radiation field (G_0; as derived from the FIR dust continuum) with selected PAH ratios at the [C II] 158 μm resolution. The three major PAH bands in the 6–9 μm range as well the G7.6 μm component normalized to the 11.2 μm band show very similar, positive, trends with G_0 (Figure 4.14 (a), (b), and (c)). The G7.6/11.2 intensity ratio has the best positive correlation with G_0 of all PAH (and PAH-related) bands (Figure 4.14 (d)). These positive correlations reflect the fact that all four ratios trace the PAH ionization state which is driven, in part, by a stronger radiation field. We observe two separate regimes: a tight correlation between each ratio and G_0 for lower ranges of each quantity, while, for $G_0 > 10^3$, we find substantial scatter for all four PAH ratios. In this regime, the observed relation rather gives a lower boundary to the considered PAH ratio. These stronger radiation field strengths are found within the nebula (see Figure 4.12). The increased range in these PAH ratios for a given FUV radiation strength across the nebula likely reflects the larger variation present in the electron density and gas temperature across the nebular compared to the outskirts as these parameters also determine the PAH ionization parameter and thus the PAH ionization fraction.

Figure 4.14 (e) also shows a strong anti-correlation between G7.8/G7.6 and G_0 of the form:

$$I_{7.8}/I_{7.6} = 1.7575 \; - \; 0.3797 \log G_0 \tag{4.3}$$

In contrast with the ratios discussed above, this relationship does not show increased scatter for strong FUV radiation fields ($G_0 > 10^3$). This dependence of G7.8/G7.6 on G_0 strongly supports the results of Stock & Peeters (2017). These authors found a strong anti–correlation of G7.8/G7.6 with G_0 for a sample of integrated PDRs over a wide range of physical conditions. Here we show that this also holds true within a spatially resolved source. However, we find that the slope of our fit (equation 4.3) is significantly larger than the slope of both fits given by (Stock & Peeters, 2017, see Figure 4.14). This contradicts their prediction that the inclusion of diffuse ISM regions or regions with a weak FUV radiation field will cause a shallower correlation between G7.8/G7.6 and G_0. One explanation for this discrepancy may be the lack

of data at low G_0 in the Stock & Peeters (2017) study and the large uncertainties involved in estimating G_0 as mentioned in section 4.1. In particular, here only a single method is employed to derive G_0 values while Stock & Peeters (2017) resort to multiple methods which likely result in systematic effects. While we do not probe G_0 values as low as the Ophiuchus positions in Stock & Peeters (2017), we do encounter G7.8/G7.6 ratios greater than those found in the diffuse outskirts of W49A, which has been argued to be representative of PAH spectra for diffuse ISM sightlines (Stock et al., 2014). In fact, pixels where G7.8/G7.6 > 0.88 seem to fall in between the two correlations from Stock & Peeters (2017), suggesting their predictions are not too far off for the diffuse ISM.

In Figure 4.14 (f), we find another strong anti-correlation between G8.6/G7.6 and G_0. Given that the G7.6 and G8.6 components exhibit the strongest correlation of all PAH bands (when normalized to the 11.2 μm band) for NGC 1333 (Figure 4.9) and for NGC 2023 (Peeters et al., 2017), this is somewhat surprising. However, we note that the range of variation in G8.6/G7.6 is quite small (of ~ 0.1) while G_0 varies over almost two orders of magnitude. Nevertheless, the observed anti-correlation with G8.6/G7.6 suggests that our simple four Gaussian decomposition needs further improvement to disentangle the components contributing to the 7 to 9 μm emission. Alternatively, or in addition, it may reflect the different band assignments of the 7.6 and 8.6 μm PAH emission. Indeed, while both the G7.6 and G8.6 μm components are attributed to compact symmetric cationic PAH species, the G7.6 μm emission arises from PAHs with sizes ranging from 50 – 100 carbon atoms whereas, with a few exceptions, the G8.6 μm PAH band is only detected in larger PAHs (with a size range from 96 – 150 carbon atoms, e.g. Bauschlicher et al., 2008, 2009; Ricca et al., 2012; Peeters et al., 2017). This tight correlation with G_0 may be suggestive of photo-processing of the larger compact to smaller compact PAHs as they are increasingly exposed to the radiation field.

In Figure 4.15, we compare the map of the ionization parameter, γ, derived from the PDR models with a few relevant PAH ratios. We note that convolving the IRS spectral maps to the PSF of the [C II] 158 μm observation and accounting for the 3 σ detection limits of the [O I] 63 μm map in our PDR models restricts this comparison primarily to pixels within nebula as shown in Figure 4.12. In Figure 4.15 (a) and (b), we do not find a significant correlation between 6.2/11.2 and 7.7/11.2 with γ. Nevertheless, no low PAH ratios are found for medium to high values of the PAH ionization parameter. Here as well, the observed relation (fit) gives a lower boundary to the considered PAH ratio. This is in contrast with the strong correlation between γ and 6.2/11.2 found by Galliano et al. (2008) and Boersma et al. (2015). We note the different regimes in γ considered in this study compared to Galliano et al. (2008) and Boersma et al. (2015): both of these studies consider regions where $\gamma > 10^4$. Nevertheless, this discrepancy may arise from the methodology we used to derive the PDR conditions: Galliano et al. (2008) assumed a fixed n_H and T for the Orion Bar whereas we derived both n_H and T using PDR models. Additionally, these models may not be sensitive enough to probe the PDR at the same resolution as the MIR and the FIR maps. In Figure 4.15 (c), compares γ with G8.6/G7.6 where we do see a modest anti-correlation. However, there is significant scatter and the range in G8.6/G7.6 is ~ 0.05. Hence, this may as well reflect the imperfectness of the four Gaussian decomposition.

In summary, from this comparison between PAH emission ratios and PDR conditions in and around the RN NGC 1333 there is clearly evidence to support the case for the emission features as viable PDR diagnostics in particular with respect to G_0.

4.7   Conclusion

In this chapter, we characterize the PAH emission and investigate its dependence on the physical conditions for the RN NGC 1333 by using a *Spitzer*–IRS spectral map from 5–15 μm, *SOFIA* FIFI–LS spectral maps of the FIR cooling lines [O I] at 63 and 146 μm and [C II] at 158 μm and *Herschel* PACS images at 70, 100 and 160 μm. We derive maps for the PDR's physical conditions using the FIR cooling lines and the FIR dust continuum emission determined from SED fitting of the PACS images in combination with the PDR models of Kaufman et al. (2006) and Pound & Wolfire (2008). The derived physical conditions are in agreement with previous PDR modelling efforts of Young Owl et al. (2002). Subsequently, we compare the MIR PAH emission with the PDR conditions determined from the FIR data using matching apertures and spatial resolution for the MIR and FIR data.

Within the nebula, we find a distinction in the behaviour between the PAH emission bands in the 6–9 μm range and the 11.2 μm band along with the underlying plateaus between 5–10 and 10–15 μm with respect to the distance from the illuminating source, SVS 3. Namely, the 6–9 μm PAH bands are much more condensed within the nebula relative the 11.2 μm band and the plateaus. This dichotomy is also reflected in the 7–9 μm Gaussian components where the G7.6 and G8.6 μm components show a similar structure to the 6–9 μm bands whereas the G7.8 and G8.2 μm components are more comparable to the 11.2 μm band group.

In addition, we find the PAH characteristics of the nebula and the diffuse outskirts to be distinct from each other. Specifically, the PAH emission features within the nebula tend to be stronger and more tightly correlated with respect to the PAH features from the diffuse regions. In several cases, we find separate linear correlations for the diffuse emission and the nebula suggesting their PAH population consist of distinct subpopulations with different underlying properties. This supports previous evidence of multi-linear trends discovered between PAH ratios with respect to different physical environments.

We investigate previously reported relationships between PAH emission ratios and the physical condition within the relatively simple PDR geometry of the RN NGC 1333. We find strong correlations between the ratio of the 6–9 μm bands to the 11.2 μm band and the FUV radiation field strength particularly within the diffuse ISM. We also find strong negative correlations between ratios of the 7–9 μm Gaussian components, G7.8/G7.6 and G8.6/G7.6, with respect to G_0. This supports a similar relationship found by Stock & Peeters (2017) between G7.8/G7.6 and G_0 for a sample of PDRs covering 3 orders of magnitude in G_0. We did not find strong correlations between the ionization parameter and the 6.2/11.2 contradicting the previously established relationships of Galliano et al. (2008) and Boersma et al. (2015). However, we did find there is a promising correlation between G8.6/G7.6 and γ that warrants additional investigation.

To conclude, PAHs have much potential as PDR diagnostics. Further refinement of these correlations between PAH emission and PDR conditions will solidify the value of the PAH emission features in PDR studies. A robust survey of PAH and FIR observations in spatially resolved PDR sources within the Galaxy is the next step to accomplish this goal. With the imminent launch of JWST and the FIR access of SOFIA, a new golden age of astronomy will allow astronomers to characterize PDR environments and their PAH emission in our own Milky way as well as in extragalactic sources.

Acknowledgements

Chapter 5

Conclusions

In this thesis, we investigated the characteristics of the PAH emission features in nearby Galactic PDRs with respect to the properties of the underlying carriers and their physical environment. The main topics we tried to shed light on include:

How does the PAH size distribution vary within spatially resolved PDRs and with the strength of the incident FUV radiation field?

In Chapter 2, we present observations from *SOFIA* FLITECAM and the *Spitzer* IRAC and IRS SH mode in three well-known photo-dissociation Regions (PDRs), the RNe NGC 7023 and NGC 2023 and to the southeast of the Orion Bar, each of which are well suited to probe PAH emission. We investigate the spatial behaviour of the FLITECAM 3.3 μm filter as a proxy for the 3.3 μm PAH band, the IRS SH derived integrated 11.2 μm PAH band, and the IRAC 8.0 μm filter as a proxy for the sum of the 7.7 and 8.6 μm PAH bands. The resulting ratio of IRAC 8.0/11.2 provides an approximate measure of PAH ionization while the ratio of 11.2/3.3 combined with emission models of PAHs of varying sizes (e.g. Ricca et al., 2012; Croiset et al., 2016; Maragkoudakis et al., 2020) provides a measure of the average PAH size.

In both RNe, we find that the average PAH size and relative PAH ionization reaches a minimum near the PDR front and increases with proximity to the respective illuminating stars. The average PAH sizes derived for NGC 2023 are greater than those found for NGC 7023 at all points. As NGC 2023 has a stronger FUV radiation field intensity than NGC 7023, both results indicate that PAH size is dependent on the radiation field intensity. These results provide additional evidence of a rich carbon-based chemistry driven by the photo-chemical evolution of the omnipresent PAH molecules within the interstellar medium.

In contrast, no major trend was found for the average PAH size or relative ionization with respect to the illuminating source in the region southeast of the Orion Bar. We attribute this to the face-on morphology of the PDR found between the Orion Bar and the Veil. In a face-on PDR, no stratification of the key zones in the PDR can be observed as they are mixed within the line of sight. More data is needed to better characterize the PAH population in this region.

How do the major PAH emission features vary with respect to different astronomical environments?

In Chapters 3 and 4, we make use of *Spitzer* IRS SL observations of the Orion Bar and the RN NGC 1333 respectively. We measure the fluxes from the PAH emission features, atomic recombination lines, H_2 lines, and the underlying dust continuum present within the spectra. The Orion Bar and NGC 1333 both show evidence of spatial variations in the relative intensities of PAH emission features. These variations are found to be highly dependent on the distance from the illuminating source and thus the FUV radiation field strength. There is a clear spatial sequence in the relative strength of the PAH emission features with respect to distance from the illuminating sources that is indicative of photoprocessing driving the chemical evolution of each PAH population.

Within the Orion Bar spectra, we find a decoupling of the usual tight relationship between the 6.2 and 7.7 μm bands within the H ɪɪ region with a minimum in the 6.2/7.7 ratio at the G_0 peak. Correspondingly, we find the 8.6/7.7 ratio is enhanced with the H ɪɪ region. This suggests there is a shift in the relative strength of the intrinsic vibrational modes of the emitting population that is driven by the FUV radiation field.

Furthermore, the Orion Bar observations show significant scatter in several well-known strong PAH correlations. Considering data arising from the H ɪɪ gas (i.e. in front of the ionization front) and from the neutral region (i.e. behind the ionization front) did not alleviate this discrepancy. However, grouping these spectra based on the PDR morphology instead shows two distinct trends for several of these PAH correlations indicating that the emission in edge-on and face-on PDRs exhibit different relationships between the relative PAH intensities. Similarly, comparing the PAH emission in NGC 1333 within the diffuse outskirts, we find that the relative emission is stronger and better correlated in the RN. The relative behaviour of the PAH bands normalized to the 11.2 μm band depends on the type of environment in which they reside namely: the diffuse ISM, the irradiated PDR or the transition region between these environments. We detect a discrete set of trends or branches (e.g. one, two, of three) between emission features that we attribute to these different environments. This implies that some of the PAH bands arise from multiple PAH subpopulations or from multiple grand–PAHs (Andrews et al., 2015) with distinct relative PAH intrinsic intensities and different relative abundances in these different environments.

How can PAHs be used as PDR diagnostics for future studies?

In Chapters 3 and 4, we use observations of the Orion Bar and the RN NGC 1333 respectively to test previously reported correlations between the PAH emission features and the PDR physical conditions (e.g. Galliano et al., 2008; Pilleri et al., 2012; Boersma et al., 2013; Stock & Peeters, 2017). We use different methods to derive the PDR conditions for both sources. Hence, we consider their results separately.

Orion Bar We follow the method of Galliano et al. (2008) to derive a FUV radiation field intensity, G_0, profile in both IRS apertures using a relationship between G_0 and the dust continuum emission. Assuming that the electron density and gas temperature do not vary within these apertures, we subsequently derive the PAH ionization parameter, γ.

We find comparable relationships between G_0 and the G7.8/G7.6 ratio as reported by Stock & Peeters (2017) and between γ and the 6.2/11.2 ratio as reported by Galliano et al. (2008). However, we report differences in these relationships derived for edge-on and face-on PDRs. Notably the fits from the edge-on PDR spectra showed the best agreement with both Stock & Peeters (2017) and Galliano et al. (2008), while the fits from the face-on PDR deviated significantly from the previous studies.

NGC 1333   We make use of *SOFIA* FIFI-LS observations to measure the FIR cooling lines at [O I] 63, 146 and [C II] 158 μm, archival *Herschel* PACs observations to measure the FIR dust continuum emission and use previously obtained *Spitzer* IRS SL data to measure the PAH emission features (Stock et al., 2016). From the FIR dust continuum emission, we estimate the intensity of the FUV radiation field, G_0, within NGC 1333 (Hollenbach & Tielens, 1997). Combining this FIR dust continuum emission with the FIR cooling lines into PDR models (Kaufman et al., 2006; Pound & Wolfire, 2008) allows us to estimate the electron density, n_e, and gas temperature, T_{gas}, within NGC 1333. We convert all images onto a grid of matching aperture and spatial resolution to allow a comparison of the PAH emission with these physical conditions.

We derived linear relationships between the ratios of the 6–9 μm bands to the 11.2 μm band with G_0. Correlations between these parameters were found to be stronger within the diffuse ISM compared with the nebula. We also find a strong anti-correlation between G7.8/G7.6 with G_0 and G8.6/G7.6 with G_0. We were unable to find any significant correlations between the ratios of the 6–9 μm bands to the 11.2 μm band with γ contradicting the results of Galliano et al. (2008) and of the edge-on PDR in the Orion Bar (Chapter 3). The lack of relationship between 6.2/11.2 and γ found in this source in comparison to the strong relationship derived by Galliano et al. (2008) for the Orion Bar may be attributable to the different assumptions made in deriving the ionization parameter: Galliano et al. (2008) assumed a fixed n_H and T for the Orion Bar whereas we derived both n_H and T using PDR models.

5.1   Future Work

With the James Webb Space Telescope (JWST) planned to become operational in the next decade, there is an abundance of opportunities to study astronomical PAHs and their relationship with PDRs in greater detail than ever before. Galactic nearby MIR bright sources such as those encountered in this thesis can be revisited with improved angular resolution and greater sensitivity not possible with the previous generation of space-based observatories. In particular, with higher spatial resolution we can probe individual key areas within nearby PDRs such as the Orion Bar at the scale on which PAH processing occurs. Higher sensitivity will allow us to detect the weaker PAH bands or PAH emission from extragalactic sources in greater detail than ever before. The medium spectral resolution of JWST coupled with the higher spatial resolution will greatly advance studies of the spectral substructure of the PAH emission features and their relative profiles building on these results within the past 30 years (e.g. Bregman et al., 1989; Cohen et al., 1989; Peeters et al., 2002; van Diedenhoven et al., 2004; Bregman & Temi, 2005; Sloan et al., 2007; Matsuura et al., 2014) and will allow for futher refinement of PAH emission decomposition methods such as the 7–9 μm Gaussian decomposition (Peeters et al.,

2017; Stock & Peeters, 2017, Chapters 3 and 4). In addition, JWST is capable of covering all of the major PAH bands with the on–board suite of instruments eliminating the need for the use of multiple observations to cover this range. Obtaining access to a spatially resolved spectral mapping of all the major PAH bands of an extended source allows us to investigate various PAH properties such as charge, size, and structure (e.g. Croiset et al., 2016; Maragkoudakis et al., 2018, 2020, Chapter 2). These improvements will yield a better understanding of the relationship between the PAH bands as well as the role UV processing plays in the physical and chemical evolution of their carriers.

Significant results for astronomical PAH research are expected early in the life cycle of JWST with the Early Release Science program ID 1288 titled:"Radiative Feedback from Massive Stars as Traced by Multiband Imaging and Spectroscopic Mosaics". This program intends to perform spectral mapping from 1–28.5 μm across the Orion Bar with an effective aperture of $\sim 27'' \times 3''$, angular resolution from 0.2″–1.14″, and a spectral resolution of 1550–3250 covering the H II region, the edge-on PDR and extending well into the southeastern face-on PDR behind the Bar (i.e. improved PAH emission measurements for Chapters 2 and 3). Additionally, NIR and MIR imaging of the Bar will be done with filters covering the 3.3, 7.7, 8.6, and 11.2 μm bands. This program will employ cross-calibration of MIR spectra and images, further constraining the relative contributions of spectral features including the PAH emission bands, the PAH plateaus and the underlying dust continuum emission within a given filter and/or spectral aperture. This will allow us to refine the methodology of using photometric observations to trace PAH emission (Chapter 2). Other relevant highlights of this program include creating template spectrum using BSS (e.g. Berné et al., 2007), using PAHdb theoretical and experimental PAH spectra to fit the Orion Bar spectra (e.g. Boersma et al., 2013), and using the PDRT to derive the physical parameters from the latest PDR models (e.g. Neufeld & Wolfire, 2016). To summarize, the results from this program will allow us to better constrain the results of Chapters 2–4, such as more precise estimates of PAH size and ionization, investigating the influence of edge-on versus face-on PDR morphologies on the observed PAH emission, and deriving higher resolution PDR models than previously obtained.

To understand the impact of new space-based observatories have had on PAH-based research, we need only look back to *Spitzer*. Since its launch over 17 years ago, *Spitzer* has advanced our understanding of the PAH emission features in nearby sources such as NGC 2023 and NGC 7023 through the use of spectral mapping which allows us to link spectral characteristics to the spatial morphology (e.g. Berné et al., 2007; Peeters et al., 2012; Boersma et al., 2013; Shannon et al., 2015; Stock et al., 2016; Peeters et al., 2017; Stock & Peeters, 2017). With JWST, the power of spectral mapping will be brought to a whole new level. Furthermore, the number of MIR sources available for spatially resolved PAH studies will grow substantially. To summarize, JWST, along with its on–board suite of instruments, will revolutionize PAH research.

As discussed in Chapters 3 and 4, the PAH emission features have immense potential to be used in the study of PDRs. However, there are significant discrepancies between previous attempts at empirical calibrations of PAH emission with the PDR physical conditions (c.f. Section 1.5.3). Hence more data is needed to fortify and calibrate these relationships for the full range of observed environments. A large survey of PAH emission features within Galactic PDRs over a wide range of FUV radiation field strengths, G_0, and gas densities, n_H, will give more confidence in the general use of PAH emission as PDR diagnostics. This can be done by

obtaining FIR cooling line and PAH emission observations with matching apertures and spatial resolution as was done in Chapter 4 for the RN NGC 1333. *SOFIA* will be invaluable for this purpose in the coming decade as it is the sole observatory to offer FIR spectral mapping with on–board instruments such as FIFI-LS and GREAT (e.g. Andrews et al., 2018; Pabst et al., 2019; Goicoechea et al., 2020, Chapter 4). Through the use of FIR cooling lines and FIR dust continuum emission measurements as input into PDR models, spatially resolved maps of G_0 and n_H, and T can be derived (e.g. Wolfire et al., 1990; Kaufman et al., 1999, 2006; Hollenbach et al., 2012). Comparing the trends found in maps of the PAH emission ratios such as 6.2/11.2 (Galliano et al., 2008; Boersma et al., 2013), G7.8/G7.6 (Stock & Peeters, 2017), or the fraction of carbons locked in VSG (Pilleri et al., 2012) to the physical parameters derived from PDR models with a comprehensive data set of PDR covering a wide range in G_0 and n_H will constrain relationships between PAHs and their environment to an unprecedented level. With the launch of JWST planned for this decade, the availability of a large survey of these PAH diagnostics could prove to be an invaluable resource to the extragalactic astronomy community in particular, as the aforementioned FIR cooling lines tend to be significantly harder to resolve at these distances and the corresponding PAH emission is readily available.

Bibliography

Aapo Hyvärinen, J. K. . E. O., ed. 2001, Independent Component Analysis (Wiley)

Abergel, A., et al. 2002, A&A, 389, 239

—. 2010, A&A, 518, L96

Aitken, D. K., Roche, P. F., Spenser, P. M., & Jones, B. 1979, A&A, 76, 60

Allain, T., Leach, S., & Sedlmayr, E. 1996, A&A, 305, 602

Allamandola, L. J. 2011, in EAS Publications Series, Vol. 46, EAS Publications Series, ed. C. Joblin & A. G. G. M. Tielens, 305–317

Allamandola, L. J., Hudgins, D. M., & Sandford, S. A. 1999, ApJ, 511, L115

Allamandola, L. J., Tielens, A. G. G. M., & Barker, J. R. 1985, ApJ, 290, L25

—. 1989, ApJS, 71, 733

An, J. H., & Sellgren, K. 2003, ApJ, 599, 312

Andrews, H., Boersma, C., Werner, M. W., Livingston, J., Allamandola, L. J., & Tielens, A. G. G. M. 2015, ApJ, 807, 99

Andrews, H., Peeters, E., Tielens, A. G. G. M., & Okada, Y. 2018, A&A, 619, A170

Bakes, E. L. O., & Tielens, A. G. G. M. 1994, ApJ, 427, 822

Bauschlicher, Jr., C. W., Peeters, E., & Allamandola, L. J. 2008, ApJ, 678, 316

—. 2009, ApJ, 697, 311

Bauschlicher, Jr., C. W., et al. 2010, ApJS, 189, 341

Bauschlicher, Charles W., J., Ricca, A., Boersma, C., & Allamandola, L. J. 2018, ApJS, 234, 32

Berné, O., Cox, N. L. J., Mulas, G., & Joblin, C. 2017, A&A, 605, L1

Berné, O., Joblin, C., Rapacioli, M., Thomas, J., Cuillandre, J.-C., & Deville, Y. 2008, A&A, 479, L41

Berné, O., Montillaud, J., & Joblin, C. 2015, A&A, 577, A133

Berné, O., & Tielens, A. G. G. M. 2012, Proceedings of the National Academy of Science, 109, 401

Berné, O., et al. 2007, A&A, 469, 575

Boersma, C., Bauschlicher, C. W., Allamandola, L. J., Ricca, A., Peeters, E., & Tielens, A. G. G. M. 2010, A&A, 511, A32

Boersma, C., Bregman, J. D., & Allamandola, L. J. 2013, ApJ, 769, 117

—. 2014a, ApJ, 795, 110

—. 2015, ApJ, 806, 121

—. 2016, ApJ, 832, 51

Boersma, C., Hony, S., & Tielens, A. G. G. M. 2006, A&A, 447, 213

Boersma, C., Rubin, R. H., & Allamandola, L. J. 2012, ApJ, 753, 168

Boersma, C., et al. 2014b, ApJS, 211, 8

Boissel, P., Joblin, C., & Pernot, P. 2001, A&A, 373, L5

Bregman, J. D. 1989, in IAU Symposium, Vol. 135, Interstellar Dust, ed. L. J. Allamandola & A. G. G. M. Tielens, 109

Bregman, J. D., Allamandola, L. J., Witteborn, F. C., Tielens, A. G. G. M., & Geballe, T. R. 1989, ApJ, 344, 791

Bregman, J. D., Rank, D., Sandford, S. A., & Temi, P. 1993, ApJ, 410, 668

Bregman, J. D., & Temi, P. 2005, ApJ, 621, 831

Burton, M. G., Howe, J. E., Geballe, T. R., & Brand, P. W. J. L. 1998, PASA, 15, 194

Calzetti, D., et al. 2007, ApJ, 666, 870

Cami, J., Bernard-Salas, J., Peeters, E., & Malek, S. E. 2010, Science, 329, 1180

Carroll, B. W., & Ostlie, D. A. 2007, An introduction to modern astrophysics. (Addison-Wesley)

Cesarsky, D., Lequeux, J., Abergel, A., Perault, M., Palazzi, E., Madden, S., & Tran, D. 1996, A&A, 315, L305

Cesarsky, D., Lequeux, J., Ryter, C., & Gérin, M. 2000, A&A, 354, L87

Chan, K. W., et al. 2000, in ESA Special Publication, Vol. 456, ISO Beyond the Peaks: The 2nd ISO Workshop on Analytical Spectroscopy, ed. A. Salama, M. F. Kessler, K. Leech, & B. Schulz, 59

Cherchneff, I., Barker, J. R., & Tielens, A. G. G. M. 1992, ApJ, 401, 269

Chokshi, A., Tielens, A. G. G. M., Werner, M. W., & Castelaz, M. W. 1988, ApJ, 334, 803

Clayton, D. D., Deneault, E. A.-N., & Meyer, B. S. 2001, ApJ, 562, 480

Cohen, M., Tielens, A. G. G. M., & Allamandola, L. J. 1985, ApJ, 299, L93

Cohen, M., Tielens, A. G. G. M., Bregman, J. D., Witteborn, F. C., Rank, D. M., Allamandola, L. J., Wooden, D., & Jourdain de Muizon, M. 1989, ApJ, 341, 246

Colditz, S., et al. 2018, Journal of Astronomical Instrumentation, 7, 1840004

Cordiner, M. A., et al. 2019, ApJ, 875, L28

Croiset, B. A., Candian, A., Berné, O., & Tielens, A. G. G. M. 2016, A&A, 590, A26

Cuadrado, S., Goicoechea, J. R., Pilleri, P., Cernicharo, J., Fuente, A., & Joblin, C. 2015, A&A, 575, A82

Draine, B. T. 1978, ApJS, 36, 595

Duley, W. W., & Williams, D. A. 1981, MNRAS, 196, 269

—. 1988, MNRAS, 231, 969

Engelbracht, C. W., et al. 2006, ApJ, 642, L127

Fadda, D., & Chambers, E. T. 2018, in American Astronomical Society Meeting Abstracts, Vol. 231, American Astronomical Society Meeting Abstracts #231, 150.11

Fazio, G. G., et al. 2004, ApJS, 154, 10

Field, D., Gerin, M., Leach, S., Lemaire, J. L., Pineau Des Forets, G., Rostas, F., Rouan, D., & Simons, D. 1994, A&A, 286, 909

Fischer, C., et al. 2018, Journal of Astronomical Instrumentation, 7, 1840003

Fleming, B., France, K., Lupu, R. E., & McCandliss, S. R. 2010, ApJ, 725, 159

Frenklach, M., Clary, D. W., Gardiner, W. C., & Stein, S. E. 1985, Symposium (International) on Combustion, 20, 887

Frenklach, M., & Feigelson, E. D. 1989, ApJ, 341, 372

Gaia Collaboration et al. 2016, A&A, 595, A1

—. 2018, A&A, 616, A1

Galliano, F., Galametz, M., & Jones, A. P. 2018, ARA&A, 56, 673

Galliano, F., Madden, S. C., Tielens, A. G. G. M., Peeters, E., & Jones, A. P. 2008, ApJ, 679, 310

Gatley, I., et al. 1987, ApJ, 318, L73

Geballe, T. R., Tielens, A. G. G. M., Allamandola, L. J., Moorhouse, A., & Brand, P. W. J. L. 1989, ApJ, 341, 278

Giard, M., Bernard, J. P., Lacombe, F., Normand, P., & Rouan, D. 1994, A&A, 291, 239

Gillett, F. C., Forrest, W. J., & Merrill, K. M. 1973, ApJ, 183, 87

Goicoechea, J. R., et al. 2015, ApJ, 812, 75

—. 2017, A&A, 601, L9

—. 2020, A&A, 639, A1

Goto, M., et al. 2003, ApJ, 589, 419

Gutermuth, R. A., et al. 2008, ApJ, 674, 336

Habart, E., Boulanger, F., Verstraete, L., Walmsley, C. M., & Pineau des Forêts, G. 2004, A&A, 414, 531

Habing, H. J. 1968, Bull. Astron. Inst. Netherlands, 19, 421

Haraguchi, K., Nagayama, T., Kurita, M., Kino, M., & Sato, S. 2012, PASJ, 64, 127

Harvey, P. M., Wilking, B. A., & Joy, M. 1984, ApJ, 278, 156

Heays, A. N., Bosman, A. D., & van Dishoeck, E. F. 2017, A&A, 602, A105

Hirota, T., et al. 2008, PASJ, 60, 37

Hogg, D. W., Tremonti, C. A., Blanton, M. R., Finkbeiner, D. P., Padmanabhan, N., Quintero, A. r. D., Schlegel, D. J., & Wherry, N. 2005, ApJ, 624, 162

Hollenbach, D., Kaufman, M. J., Neufeld, D., Wolfire, M., & Goicoechea, J. R. 2012, ApJ, 754, 105

Hollenbach, D. J., & Tielens, A. G. G. M. 1997, ARA&A, 35, 179

—. 1999, Reviews of Modern Physics, 71, 173

Hony, S., Van Kerckhoven, C., Peeters, E., Tielens, A. G. G. M., Hudgins, D. M., & Allamandola, L. J. 2001, A&A, 370, 1030

Houck, J. R., et al. 2004, in Proc. SPIE, Vol. 5487, Optical, Infrared, and Millimeter Space Telescopes, ed. J. C. Mather, 62–76

Houde, M., & Vaillancourt, J. E. 2007, PASP, 119, 871

Hudgins, D. M., & Allamandola, L. J. 1999, ApJ, 516, L41

Hudgins, D. M., & Allamandola, L. J. 2004, in Astronomical Society of the Pacific Conference Series, Vol. 309, Astrophysics of Dust, ed. A. N. Witt, G. C. Clayton, & B. T. Draine, 665

Hudgins, D. M., Bauschlicher, Jr., C. W., & Allamandola, L. J. 2005, ApJ, 632, 316

Hudgins, D. M., Sandford, S. A., & Allamandola, L. J. 1994, The Journal of Physical Chemistry, 98, 4243, pMID: 12269375

Joblin, C., Tielens, A. G. G. M., Allamandola, L. J., & Geballe, T. R. 1996a, ApJ, 458, 610

Joblin, C., Tielens, A. G. G. M., Geballe, T. R., & Wooden, D. H. 1996b, ApJ, 460, L119

Jones, A. P. 2004, in Astronomical Society of the Pacific Conference Series, Vol. 309, Astrophysics of Dust, ed. A. N. Witt, G. C. Clayton, & B. T. Draine, 347

Jones, A. P., Tielens, A. G. G. M., & Hollenbach, D. J. 1996, ApJ, 469, 740

Kaiser, R. I., Parker, D. S. N., & Mebel, A. M. 2015, Annual Review of Physical Chemistry, 66, 43

Kaufman, M. J., Wolfire, M. G., & Hollenbach, D. J. 2006, ApJ, 644, 283

Kaufman, M. J., Wolfire, M. G., Hollenbach, D. J., & Luhman, M. L. 1999, ApJ, 527, 795

Kounkel, M., et al. 2018, AJ, 156, 84

Kroto, H. W., & Jura, M. 1992, A&A, 263, 275

Kurucz, R. L. 1993, VizieR Online Data Catalog, 6039

Latter, W. B. 1991, ApJ, 377, 187

Léger, A., & Puget, J. L. 1984, A&A, 137, L5

Lemaire, J. L., Field, D., Gerin, M., Leach, S., Pineau des Forets, G., Rostas, F., & Rouan, D. 1996, A&A, 308, 895

Lepp, S., & Dalgarno, A. 1988, ApJ, 324, 553

Lique, F., Kłos, J., Alexander, M. H., Le Picard, S. D., & Dagdigian, P. J. 2018, MNRAS, 474, 2313

Liseau, R., Sandell, G., & Knee, L. B. G. 1988, A&A, 192, 153

Lord, S. 1992, NASA Technical Memorandum, 103957, 153

Maltseva, E., et al. 2016, ApJ, 831, 58

Maragkoudakis, A., Ivkovich, N., Peeters, E., Stock, D. J., Hemachandra, D., & Tielens, A. G. G. M. 2018, MNRAS, 481, 5370

Maragkoudakis, A., Peeters, E., & Ricca, A. 2020, MNRAS, 494, 642

Matsuura, M., et al. 2014, MNRAS, 439, 1472

Megeath, S. T., et al. 2012, AJ, 144, 192

Melnick, G., Gull, G. E., & Harwit, M. 1979, ApJ, 227, L29

Menten, K. M., Reid, M. J., Forbrich, J., & Brunthaler, A. 2007, A&A, 474, 515

Miller, J. A., & Melius, C. F. 1992, Combustion and Flame, 91, 21

Mori, T. I., Sakon, I., Onaka, T., Kaneda, H., Umehata, H., & Ohsawa, R. 2012, ApJ, 744, 68

Moutou, C., Verstraete, L., Sellgren, K., & Leger, A. 1999, in ESA Special Publication, Vol. 427, The Universe as Seen by ISO, ed. P. Cox & M. Kessler, 727

Neufeld, D. A., & Wolfire, M. G. 2016, ApJ, 826, 183

O'Dell, C. R., Kollatschny, W., & Ferland, G. J. 2017, ApJ, 837, 151

Ossenkopf, V., Koumpia, E., Okada, Y., Mookerjea, B., van der Tak, F. F. S., Simon, R., Pütz, P., & Güsten, R. 2015, A&A, 580, A83

Pabst, C., et al. 2019, Nature, 565, 618

Papoular, R., Conrad, J., Giuliano, M., Kister, J., & Mille, G. 1989, A&A, 217, 204

Peeters, E., Allamandola, L. J., Hudgins, D. M., Hony, S., & Tielens, A. G. G. M. 2004a, in Astronomical Society of the Pacific Conference Series, Vol. 309, Astrophysics of Dust, ed. A. N. Witt, G. C. Clayton, & B. T. Draine, 141

Peeters, E., Bauschlicher, Jr., C. W., Allamandola, L. J., Tielens, A. G. G. M., Ricca, A., & Wolfire, M. G. 2017, ApJ, 836, 198

Peeters, E., Hony, S., Van Kerckhoven, C., Tielens, A. G. G. M., Allamandola, L. J., Hudgins, D. M., & Bauschlicher, C. W. 2002, A&A, 390, 1089

Peeters, E., Spoon, H. W. W., & Tielens, A. G. G. M. 2004b, ApJ, 613, 986

Peeters, E., Tielens, A. G. G. M., Allamandola, L. J., & Wolfire, M. G. 2012, ApJ, 747, 44

Pilbratt, G. L., et al. 2010, A&A, 518, L1

Pilleri, P., Joblin, C., Boulanger, F., & Onaka, T. 2015, A&A, 577, A16

Pilleri, P., Montillaud, J., Berné, O., & Joblin, C. 2012, A&A, 542, A69

Poglitsch, A., et al. 2010, A&A, 518, L2

Pound, M. W., & Wolfire, M. G. 2008, Astronomical Society of the Pacific Conference Series, Vol. 394, The Photo Dissociation Region Toolbox, ed. R. W. Argyle, P. S. Bunclark, & J. R. Lewis, 654

Puget, J. L., & Léger, A. 1989, ARA&A, 27, 161

Rapacioli, M., Joblin, C., & Boissel, P. 2005, A&A, 429, 193

Ricca, A., Bauschlicher, Jr., C. W., Boersma, C., Tielens, A. G. G. M., & Allamandola, L. J. 2012, ApJ, 754, 75

Roche, P. F., Aitken, D. K., & Smith, C. H. 1989, MNRAS, 236, 485

—. 1994, MNRAS, 269, 649

Rosenberg, M. J. F., Berné, O., Boersma, C., Allamandola, L. J., & Tielens, A. G. G. M. 2011, A&A, 532, A128

Rubin, R. H., Simpson, J. P., O'Dell, C. R., McNabb, I. A., Colgan, S. W. J., Zhuge, S. Y., Ferland, G. J., & Hidalgo, S. A. 2011, MNRAS, 410, 1320

Russell, R. W., Melnick, G., Gull, G. E., & Harwit, M. 1980, ApJ, 240, L99

Russell, R. W., Melnick, G., Smyers, S. D., Kurtz, N. T., Gosnell, T. R., Harwit, M., & Werner, M. W. 1981, ApJ, 250, L35

Russell, R. W., Soifer, B. T., & Willner, S. P. 1977, ApJ, 217, L149

Sakata, A., Wada, S., Tanabe, T., & Onaka, T. 1984, ApJ, 287, L51

Salgado, F., Berné, O., Adams, J. D., Herter, T. L., Keller, L. D., & Tielens, A. G. G. M. 2016, ApJ, 830, 118

Sandell, G., Mookerjea, B., Güsten, R., Requena-Torres, M. A., Riquelme, D., & Okada, Y. 2015, A&A, 578, A41

Schneider, N., et al. 2018, A&A, 617, A45

Schutte, W. A., Tielens, A. G. G. M., & Allamandola, L. J. 1993, ApJ, 415, 397

Sellgren, K. 1981, ApJ, 245, 138

—. 1983, AJ, 88, 985

—. 1984, ApJ, 277, 623

Sellgren, K., Tokunaga, A. T., & Nakada, Y. 1990, ApJ, 349, 120

Sellgren, K., Werner, M. W., & Allamandola, L. J. 1996, ApJS, 102, 369

Sellgren, K., Werner, M. W., Ingalls, J. G., Smith, J. D. T., Carleton, T. M., & Joblin, C. 2010, ApJ, 722, L54

Shannon, M. J., & Boersma, C. 2019, ApJ, 871, 124

Shannon, M. J., Stock, D. J., & Peeters, E. 2015, ApJ, 811, 153

—. 2016, ApJ, 824, 111

Shu, F. H., Adams, F. C., & Lizano, S. 1987, ARA&A, 25, 23

Skrutskie, M. F., et al. 2006, AJ, 131, 1163

Sloan, G. C., Bregman, J. D., Geballe, T. R., Allamandola, L. J., & Woodward, E. 1997, ApJ, 474, 735

Sloan, G. C., Hayward, T. L., Allamandola, L. J., Bregman, J. D., DeVito, B., & Hudgins, D. M. 1999, ApJ, 513, L65

Sloan, G. C., et al. 2007, ApJ, 664, 1144

Smith, J. D. T., et al. 2007a, PASP, 119, 1133

—. 2007b, ApJ, 656, 770

Sofia, U. J., Lauroesch, J. T., Meyer, D. M., & Cartledge, S. I. B. 2004, ApJ, 605, 272

Spoon, H. W. W., Marshall, J. A., Houck, J. R., Elitzur, M., Hao, L., Armus, L., Brandl, B. R., & Charmandaris, V. 2007, ApJ, 654, L49

Steiman-Cameron, T. Y., Haas, M. R., Tielens, A. G. G. M., & Burton, M. G. 1997, ApJ, 478, 261

Stock, D. J., Choi, W. D.-Y., Moya, L. G. V., Otaguro, J. N., Sorkhou, S., Allamandola, L. J., Tielens, A. G. G. M., & Peeters, E. 2016, ApJ, 819, 65

Stock, D. J., & Peeters, E. 2017, ApJ, 837, 129

Stock, D. J., Peeters, E., Choi, W. D.-Y., & Shannon, M. J. 2014, ApJ, 791, 99

Stock, D. J., Peeters, E., Tielens, A. G. G. M., Otaguro, J. N., & Bik, A. 2013, ApJ, 771, 72

Storey, J. W. V., Watson, D. M., & Townes, C. H. 1979, ApJ, 233, 109

Strom, S. E., Vrba, F. J., & Strom, K. M. 1976, AJ, 81, 314

Tauber, J. A., Tielens, A. G. G. M., Meixner, M., & Goldsmith, P. F. 1994, ApJ, 422, 136

Temi, P., et al. 2012, in Proc. SPIE, Vol. 8444, Ground-based and Airborne Telescopes IV, 844414

Tielens, A. 2005, The Physics and Chemistry of the ISM (Cambridge Univ Press)

Tielens, A. G. G. M. 2008, ARA&A, 46, 289

Tielens, A. G. G. M., & Hollenbach, D. 1985a, ApJ, 291, 747

—. 1985b, ApJ, 291, 722

Tielens, A. G. G. M., Hony, S., van Kerckhoven, C., & Peeters, E. 1999, in ESA Special Publication, Vol. 427, The Universe as Seen by ISO, ed. P. Cox & M. Kessler, 579

Tielens, A. G. G. M., Meixner, M. M., van der Werf, P. P., Bregman, J. D., Tauber, J. A., Stutzki, J., & Rank, D. 1993, Science, 262, 86

van der Werf, P. P., Goss, W. M., & O'Dell, C. R. 2013, ApJ, 762, 101

van Diedenhoven, B., Peeters, E., Van Kerckhoven, C., Hony, S., Hudgins, D. M., Allamandola, L. J., & Tielens, A. G. G. M. 2004, ApJ, 611, 928

Van Kerckhoven, C., et al. 2000, A&A, 357, 1013

Vermeij, R., Peeters, E., Tielens, A. G. G. M., & van der Hulst, J. M. 2002, A&A, 382, 1042

Verstraete, L. 2011, in EAS Publications Series, Vol. 46, EAS Publications Series, ed. C. Joblin & A. G. G. M. Tielens, 415–426

Verstraete, L., Puget, J. L., Falgarone, E., Drapatz, S., Wright, C. M., & Timmermann, R. 1996, A&A, 315, L337

Verstraete, L., et al. 2001, A&A, 372, 981

Walawender, J., Bally, J., Francesco, J. D., Jørgensen, J., & Getman, K. . 2008, NGC 1333: A Nearby Burst of Star Formation, ed. B. Reipurth, Vol. 4, 346

Walmsley, C. M., Natta, A., Oliva, E., & Testi, L. 2000, A&A, 364, 301

Werner, M. W., Uchida, K. I., Sellgren, K., Marengo, M., Gordon, K. D., Morris, P. W., Houck, J. R., & Stansberry, J. A. 2004a, ApJS, 154, 309

Werner, M. W., et al. 2004b, ApJS, 154, 1

Whelan, D. G., Lebouteiller, V., Galliano, F., Peeters, E., Bernard-Salas, J., Johnson, K. E., Indebetouw, R., & Brandl, B. R. 2013, ApJ, 771, 16

Wolfire, M. G., Hollenbach, D., & McKee, C. F. 2010, ApJ, 716, 1191

Wolfire, M. G., Tielens, A. G. G. M., & Hollenbach, D. 1990, ApJ, 358, 116

Wolfire, M. G., Tielens, A. G. G. M., Hollenbach, D., & Kaufman, M. J. 2008, ApJ, 680, 384

Wyrowski, F., Walmsley, C. M., Goss, W. M., & Tielens, A. G. G. M. 2000, ApJ, 543, 245

Young, E. T., et al. 2012, ApJ, 749, L17

Young Owl, R. C., Meixner, M. M., Fong, D., Haas, M. R., Rudolph, A. L., & Tielens, A. G. G. M. 2002, ApJ, 578, 885

Zhen, J., Castellanos, P., Paardekooper, D. M., Linnartz, H., & Tielens, A. G. G. M. 2014, ApJ, 797, L30

Appendix A

Additional content for Chapter 2

A.1 Relative PAH contribution to the IRAC 8.0 μm emission in a PDR

The IRAC 8.0 μm emission is often used as a tracer for PAH emission (e.g. Hogg et al., 2005; Smith et al., 2007a; Stock et al., 2014). Here, we estimate the relative contribution of the individual emission components contained within the IRAC 8.0 μm filter within the South NGC 2023 IRS SL spectral cube (e.g. Stock et al., 2016; Peeters et al., 2017; Stock & Peeters, 2017). The spectral components that dominate these spectra within the IRAC 8.0 μm filter include the 7.7 and 8.6 μm emission features, the 8 μm bump and 5–10 μm plateau, both of which are attributed to emission of PAHs and related species, the 6.9 μm H_2 line, and the underlying dust continuum (where we follow the decomposition given by Peeters et al., 2017). We multiply spectral maps of these emission components by the IRAC 8.0 μm filter response function and integrate over the relevant wavelength range of each feature. Subsequently, we determine the fractional contribution of each spectral component to the total IRAC 8.0 μm flux for a given spectrum.

Figure A.1 presents these relative contributions to the IRAC 8.0 μm bandpass along a radial cut across the S ridge PDR front in the direction to the illuminating source, HD 37903. We find that along the radial cut, extending from inside the cavity to the PDR front, the PAH related species account for $\sim$ 80% of the emission within the IRAC 8.0 μm filter. Beyond the PDR front into the molecular cloud, PAH related emission drops down to $\sim$ 73% of the total emission. Thus, we can effectively state that the IRAC 8.0 μm filter is a strong tracer of PAH emission within PDR environments but becomes a less reliable tracer in molecular cloud dominated regions.

A.2 Comparing FLITECAM 3.3 μm and IRAC 3.6 μm

We compare both of the individual Orion FLITECAM 3.3 μm images with the IRAC 3.6 μm image within each FOV at a matching spatial resolution (Figure A.2). An unweighted linear relationship was found between the IRAC 3.6 μm and FLITECAM I2 observations with a slope of 3.203 $\pm$ 0.007 and an intercept of 101.4 $\pm$ 0.7 as well as between the IRAC 3.6 μm
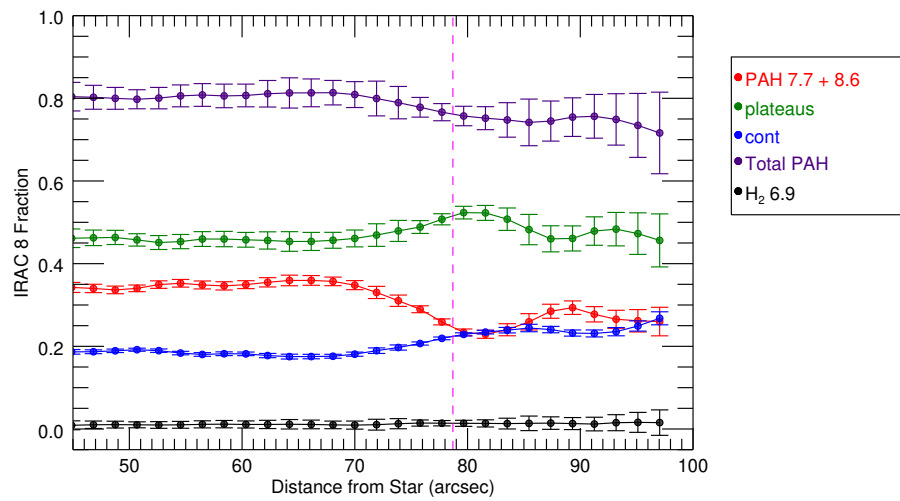
Figure A.1: A radial profile of the NGC 2023 IRS SL South data cube taking the relative contribution of the emission features within the IRAC 8.0 μm bandpass. The dashed vertical magenta line indicates the position of the PDR front as traced by H_2 emission. The position of the cross–cut is given in Peeters et al. (2017).

and FLITECAM M2 observations with a slope of 4.80 ± 0.02 and an intercept of 28.1 ± 0.3. Noise weighted linear relationships were found between the IRAC 3.6 μm and FLITECAM I2 observations with a slope of 3.876 ± 0.018 and an intercept of 55.1 ± 0.9 as well as between the IRAC 3.6 μm and FLITECAM M2 observations with a slope of 5.579 ± 0.044 and an intercept of 18.9 ± 0.5. The expected surface brightness values of both the FLITECAM I2 and IRAC 3.6 μm data within the ISO-SWS apertures across the Orion Bar are determined by multiplying each SWS spectra with the respective filter response curves. The observed surface brightness values measured at each of the SWS positions for both the FLITECAM I2 and IRAC 3.6 μm images are taken as the median value within the SWS apertures. Using linear fits with a fixed y-intercept of 0, the expected and observed data points in the IRAC 3.6 μm and FLITECAM 3.3 μm filters gives slopes of 2.765 ± 0.168 and 4.342 ± 0.997 respectively. The ratio of the observed to expected slopes is 1.57 ± 0.37, in agreement with the scale factor of 1.6 ± 0.1 derived in Section 2.4.1.
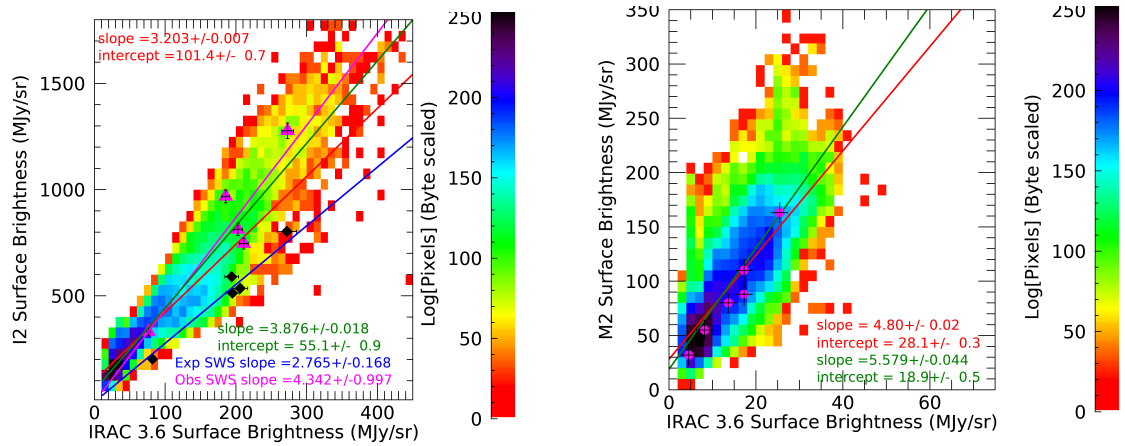

Figure A.2: The observed surface brightness in the calibrated FLITECAM data and the IRAC 3.6 μm data (after extended source correction) for all pixels contained within the I2 frame (left panel) and the M2 frame (right panel). All stellar sources present have been masked. Unweighted and weighted linear fits are given by red lines and green lines respectively. *left panel* Surface brightness values of the I2 observations within the ISO-SWS apertures are indicated by magenta triangles and expected mean surface brightness values (from multiplying the SWS spectra with each filter response curve) are shown as black diamonds. Weighted slope fits to the expected and observed mean surface brightness values from the SWS spectra are shown as a blue and magenta line respectively. *right panel* Surface brightness values of the M2 observations taken within the IRS SH apertures are shown as magenta circles.

Appendix B

Additional content for Chapter 3

B.1 Orion Bar Spitzer IRS SL Breakdown

In Table B.1, we summarize the prominent emission components found in the Orion Bar Spitzer IRS SL spectra as discussed in Chapter 3. To facilitate parsing the large amount of line profiles shown in Figures 3.4 and 3.5, we use the same nomenclature used to refer to each feature. We organize these components based on the different types of emission found and as well as where they spatially peak within each aperture relative to the Orion Bar Ionization front.

B.2 Decomposition of 7–9 μm region

We decomposed the GS subtracted spectra in the 7–9.2 μm region with 6 Gaussians. These include the 7-9 μm PAH components: G7.6, G7.8, G8.2, and G8.6 μm (Peeters et al., 2017; Stock & Peeters, 2017) and the atomic recombination lines: H I 7.45 μm and [Ar III] 8.99 μm. As in Peeters et al. (2002), we chose PAH components to fit the 7.6 and 7.8 μm peaks of the 7.7 μm complex, the 8.6 μm PAH band, and a fourth PAH component at 8.2 μm to obtain a good fit in the 7–9 μm region. We also note that the 8 μm bump found between the LS and GS spline continua is incorporated into these Gaussian components, hence the similarities between the line profiles of the 8 μm bump and the G7.8 and G8.2 μm components in particular (Figure 3.6 (d) and (h)). This fitting procedure was first run with the starting parameters of all 6 Gaussians allowed to vary in peak position in a window of 0.2 μm and in FWHM in a window of 0.1 μm. Subsequently, the average peak positions for each feature within each aperture was obtained and fixed (Table B.2). We then determine the average FWHM for each of these Gaussian fits and fix these parameters as well.

126

Table B.1: Orion Bar IRS SL Spectral Emission Components

Feature Tag[1]	Emission Description	Peak Location[2]
Atomic Lines		
[Ar ɪɪ]	[Ar ɪɪ] 6.98 μm recombination line	H ɪɪ region
H ɪ 7.46	H ɪ 7.45 μm recombination line	H ɪɪ region
[Ar ɪɪɪ]	[Ar ɪɪɪ] 8.99 μm recombination line	H ɪɪ region
[S ɪᴠ]	[S ɪᴠ] 10.5 μm recombination line	H ɪɪ region
H ɪ 12.37	H ɪ 12.37 μm recombination line	H ɪɪ region
[Ne ɪɪ]	[Ne ɪɪ] 12.8 μm recombination line	H ɪɪ region
Dust Emission		
cont. 10.2	Dust continuum emission at 10.2 μm	H ɪɪ region
cont. 13.2	Dust continuum emission at 13.2 μm	H ɪɪ region
cont.10–13	Integrated dust continuum emission from 10–13.2 μm	H ɪɪ region
PAH–Related Emission		
3.3 (FC)	PAH 3.3 μm band[3]	Orion Bar PDR
6.2	PAH 6.2 μm band	Orion Bar PDR
7.7	PAH 7.7 μm band	Orion Bar PDR
8.6	PAH 8.6 μm band	Orion Bar PDR
G7.6	PAH G7.6 μm sub–component	Orion Bar PDR
G7.8	PAH G7.8 μm sub–component	Orion Bar PDR
G8.2	PAH G8.2 μm sub–component	Orion Bar PDR
G8.6	PAH G8.2 μm sub–component	Orion Bar PDR
G11.0	PAH 11.0 μm band	Orion Bar PDR
11.2	PAH 11.2 μm band	Orion Bar PDR
12.7	PAH 12.7 μm band	Orion Bar PDR
8 bump	8 μm bump PAH plateau	Orion Bar PDR
5–10 plat	5–10 μm PAH plateau	Orion Bar PDR
10–13 plat	10–13 μm PAH plateau	Orion Bar PDR
Molecular Hydrogen Lines		
H_2 9.7	H_2 9.7 μm emission line	Orion Bar PDR

[1] Shorthand used to refer to individual features in Figures 3.4 and 3.5.; [2] Emission component peak within the Orion Bar IRS SL apertures (see Section 3.5.1).; [3] Observed with SOFIA FLITECAM photometry (see Chapter 2).

Table B.2: Orion 7 to 9 Decomposition Parameters

Feature (μm)	< Peak Position (μm) >	< FWHM (μm) >
Orion Bar Totals[1]		
Pfund α	7.481 ± 0.006	0.06 ± 0.01
GPAH 7.6	7.59 ± 0.02	0.44 ± 0.01
GPAH 7.8	7.86 ± 0.04	0.40 ± 0.03
GPAH 8.2	8.29 ± 0.02	0.263 ± 0.02
GPAH 8.6	8.61 ± 0.01	0.34 ± 0.01
Ar III 8.99	9.004 ± 0.008	0.122 ± 0.009

[1] Combined averages of fits in spectra of all three slits.

Curriculum Vitae

Collin M. Knight

Education

PhD. Astronomy, University of Western Ontario, 2020

Dissertation: "Mid-Infrared Studies of Galactic sources: Probing the Relationship Between Polycyclic Aromatic Hydrocarbons and their Physical Environment"

Advisor: Prof. Els Peeters

M.Sc. Astronomy, University of Western Ontario, 2016

M.Sc. Report: "Spatial Properties of the Polycyclic Aromatic Hydrocarbon Population in the Reflection Nebula NGC 2023"

Advisor: Prof. Els Peeters

B.Sc. Honours Physics, Memorial University of Newfoundland, 2014

Thesis: "High Pressure Morphology of Bicellar Mixtures Containing Anionic Lipids"

Advisor: Prof. Michael R. Morrow

Grants, Fellowships & Awards

2020 – Ontario Graduate Scholarship

2019 – Ontario Graduate Scholarship

2018 – Ontario Graduate Scholarship

2017 – Ontario Graduate Scholarship

2016 – Queen Elizabeth II Graduate Scholarship in Science and Technology

2016 – Ontario Graduate Scholarship

2015 – Queen Elizabeth II Graduate Scholarship in Science and Technology

2014 – UWO Entrance Scholarship

2014 – Dean's List 2013–2014

2014 – NSERC Undergraduate Student Research Award

2014 – The Harry Kiefte Scholarship

2013 – Dean's List 2012–2013

2013 – NSERC Undergraduate Student Research Award

2012 – The Marie T. Kennedy Bursary

2012 – Dean's List 2011–2012

2011 – Thomas Corbin Noel Scholarship

2007 – Millennium Scholarship

Peer-Reviewed Journal Articles

1. A. Sidhu, E. Peeters, J. Cami, **C. Knight**, 2020, *MNRAS*, 500, 177–190
   "A Principal Component Analysis of Polycyclic Aromatic Hydrocarbon Emission in NGC 2023 "

2. **C. Knight**, E. Peeters, D. J. Stock, W. D. Vacca, A.G.G.M. Tielens – Submitted
   "Tracing PAH Size in Prominent Nearby Mid-Infrared Environments"

3. **C. Knight**, A. Rahmani, and M. R. Morrow, 2016, *Langmuir*, 32, 40, 10259–10267
   "Effect of Anionic Lipid on the Barotropic Behaviour of a Ternary Bicellar Mixture"

4. A. Rahmani, **C. Knight**, M. R. Morrow, 2013, *Langmuir*, 29, 44, 13481–13490
   "Response to Hydrostatic Pressure of Bicellar Dispersions Containing an Anionic Lipid: Pressure-Induced Interdigitation"